Experimental and Computational Analysis of Interface Fracture using Extrinsic and Intrinsic Cohesive Zone Modelling

A Thesis Submitted

In Partial Fulfillment of the Requirements

for the Degree of

DOCTOR OF PHILOSOPHY

by

Pran Jyoti Saikia

(176103002)

Department of Mechanical Engineering

Indian Institute of Technology Guwahati

Guwahati-781039, India

September, 2023

Certificate

It is certified that the work contained in the Thesis titled "**Experimental and Computational Analysis of Interface Fracture using Extrinsic and Intrinsic Cohesive Zone Modelling**" submitted by **Pran Jyoti Saikia** to the Indian Institute of Technology Guwahati for the award of the degree of Doctor of Philosophy has been carried out under my supervision in the Department of Mechanical Engineering, Indian Institute of Technology Guwahati. This work has not been submitted elsewhere for the award of any other degree.

13th September, 2023

Dr. Nelson Muthu

Assistant Professor

Department of Mechanical Engineering

Indian Institute of Technology Guwahati

Guwahati — 781039

Acknowledgments

This thesis is the outcome of six years of dedicated research at IIT Guwahati. The journey was far from effortless, and I received guidance and support from many people throughout this extended duration. I extend my heartfelt gratitude to them for their invaluable assistance at various points during this period. It is now my privilege to express my profound appreciation to all of them.

To begin with, I want to convey my appreciation, particularly to my supervisor, Dr. Nelson Muthu, Department of Mechanical Engineering, IIT Guwahati. Without his sincere support, the research work would not have been possible. I also extend my deep gratitude to the members of my doctoral committee, Prof. D. Chakraborty, Dr. Sachin S. Gautam, and Dr. Amit Shelke, for their valuable contributions and insightful recommendations.

I want to express my special gratitude to the Head of the Department of Mechanical Engineering, IIT Guwahati, for providing me with a conducive environment for pursuing my research work. I am grateful to the entire technical staff of the Central Workshop, IIT Guwahati for their help in fabricating certain experimental specimens and customized fixtures. I want to thank Mr. Sanjib Sarma for his invaluable suggestions during the experiments. I would also like to provide my token of appreciation to my friends Sasanka, Atchuta, Sai, Krishnamurthy, Avneesh, Lalit, Munna, Dhiraj, Durgarao, Nilkamal, Nitish, Nilov, Biswajit, Sukanya, Kashmiri and other research scholars with whom I could discuss my research-related issues. I sincerely appreciate the Fracture Mechanics and Composite Structures laboratory at IIT Guwahati for granting me access to their composite fabrication facilities. Additionally, I would like to thank the Central Instrument Facilities, the Strength of Materials Laboratory, and the SHIMADZU UTM at IIT Guwahati for offering me the necessary facilities for my experiments.

I sincerely thank my entire family, who have been pivotal in helping me maintain a peaceful mindset consistently, with a special mention to my brothers for their encouragement and emotional support. Finally, I sincerely appreciate the Ministry of Human Resource Development, Government of India, for their financial support throughout my doctoral program.

13th September Pran Jyoti Saikia

IIT Guwahati

Contents

Abstract

In recent years, material interfaces have become part of numerous engineering and structural applications. Interface failure comprising both cohesive and adhesive failure is one of the shortcomings of bonded structures during service loading conditions. Therefore, predicting interface failures is essential for ensuring the reliability, safety, and cost-effectiveness of systems and processes across various industries. The cohesive zone model (CZM) is a widely used computational technique for analyzing the interface fracture phenomenon within computational fracture mechanics studies. The main objective of the present thesis is to expand the applicability of the CZM for a wide range of material interfaces, ranging from adhesively bonded joints to laminated composites. Additionally, the experimental crack growth studies of isotropic and orthotropic material interfaces augment the proposed numerical methodology within the finite element framework.

The CZM is classified into two types based on the shape of the traction-separation law (T-S-L): the extrinsic and the intrinsic. While there are many studies on the applications of the intrinsic CZM owing to its simplicity in implementation, the associated stress singularity characterized by the stress intensity factor (SIF) of a crack is not nullified. Until now, there has been no practical application of the extrinsic CZM, which nullifies the SIF for predicting the interface crack propagation. Therefore, one of the primary objectives of the present work is to investigate the influence of the primary parameter – characteristic length of the extrinsic cohesive zone towards nullifying the SIF and predicting load vs. displacement response due to crack propagation. The SIF at the crack tip is obtained using the interaction integral technique, including crack face traction. The computed results agree with the analytical/semi-analytical results for constant and linear T-S-L. The influence of the order of different extrinsic cohesive laws on the crack tip SIF is also analyzed and contrasted with one another. To extend the applicability of the extrinsic CZM with SIF nullification criteria, experimental interface crack growth studies on adhesively bonded joints are carried out under pure mode I and mode II loading conditions. For pure mode II loading, the intrinsic CZM is also used to predict the experimentally observed load vs. displacement response, and its performance is contrasted with the extrinsic CZM results.

Though CZMs are popular, few deterministic approaches exist to estimate the cohesive strength and fracture energy for predicting interface failure due to crack propagation. In most cases, direct and indirect approaches are used to evaluate the CZM parameters, which involve customized experimental setups and numerical procedures. The latter include regression analysis, trial and error, etc., to determine the parameters, which are computationally intensive and time-consuming. In the present thesis work, the cohesive strength is estimated using the cross-tension and short-beam shear (SBS) tests for mode I and mode II, respectively. Subsequently, the mode I and mode II cohesive energy are determined from double-cantilever beam (DCB) and end-notch flexure (ENF) tests. The experimentally determined cohesive parameters are used in the FE analyses for predicting the mechanical responses for hydroxyl functionalized multi-walled carbon nanotubes (MWCNTs) reinforced, laminated carbon fiber reinforced plastics (CFRP) under pure mode I, mode II, and mixed-mode loading. The computed mechanical responses are in good agreement with the experimental findings for different kinds of loading, demonstrating the effectiveness of the proposed approach. Finally, the fracture surfaces of composites are investigated under field emission scanning electron microscopy (FESEM) to understand the mechanics of the interface fracture.

Keywords: Interface fracture, Cohesive zone, Delamination, Composite, Adhesively bonded joint, Mixed-mode loading.

Nomenclature

$2a$	Original crack length
$2b$	Actual crack length considering the length of the cohesive zone
A_n, B_n	Coefficients of complex Eigenvalue expansion
A_N, A_S	Normal and sheared area
$\overline{c_n}, \overline{d_n}$	Coefficients used to define the near-tip stress field
E	Young's modulus
G_n^c	Critical mode I fracture energy
G_s^c	Critical mode II fracture energy
K_I, K_{II}	Pure mode I and mode II stress intensity factors, respectively
$K_{applied}, K_{cohesive}$	Stress intensity factor generated by the far-field loading and the presence of cohesive zone, respectively
k	Kolosov constant
n_x, n_y	Direction cosines of the unit normal vector along x and y-direction, respectively
N	Exponent used to define the shape of cohesive law
S_E	The brittleness number at the interface
T_x, T_y	Traction field applied at the periphery of the K-dominated region
u, v	Near tip displacement field in the cohesive zone along x and y-direction, respectively
z	Complex variable used to represent near-tip fields
δ_n	Normal separation along the cohesive zone

$\widehat{\delta_n}$	Normalized normal separation
δ_s	In-plane shear separation along the cohesive zone
$\widehat{\delta_s}$	Normalized shear separation
δ_n^c, δ_s^c	Normal and shear separation corresponding to damage initiation along the cohesive zone
δ_n^f, δ_s^f	Normal and shear final separation along the cohesive zone, respectively
$\varepsilon_{jk}^{aux}, \varepsilon_{jk}$	Auxiliary and total strain, respectively
$\eta(x)$	Arbitrary location along the crack axis
μ	Shear modulus
ν	Poisson's ratio
ρ	Cohesive zone length
σ_n	Instantaneous normal cohesive stress
σ_n^c	Normal cohesive strength
σ_s	Shear cohesive stress
σ_s^c	Shear cohesive strength
σ_{xx}	Near tip stress field in x- direction
σ_{xy}	Near tip stress field along xy-plane
σ_{yy}	Near tip stress field in y-direction
$\sigma_n^\infty, \sigma_s^\infty$	Far-field normal stress and shear stress, respectively.
$\varphi(z), \chi(z)$	Complex analytical functions used to represent the near-tip field
CNT	Carbon nanotubes
CT	Compact tension

CZM	Cohesive zone modelling
DCB	Double cantilever beam
EPFM	Elastic-plastic fracture mechanics
ENF	End notched flexure
ERR	Energy release rate
FE	Finite element
FESEM	Field emission scanning electron microscopy
LEFM	Linear elastic fracture mechanics
MMB	Mixed-mode bending
MWCNTs	Multi-walled carbon nanotubes
SBS	Short beam shear test
SERR	Strain energy release rate
SIF	Stress intensity factor
VCCT	Virtual crack closure technique

List of Figures

List of Tables

Chapter 1 Introduction

1.1 Motivation

The importance of material interfaces has grown significantly across different fields of structural and engineering applications, ranging from adhesive joining to laminated composites. However, these interfaces frequently experience debonding, which can result in the complete collapse of structures. With the increasing demand for multifunctional materials in mechanical, aerospace, and biomedical applications, it is vital to comprehend the mechanical characteristics of these interfaces to achieve optimal design outcomes. Precisely simulating the process of interfacial crack propagation is thus crucial to prevent material failure when subjected to operational loading conditions.

Therefore, it is crucial to establish dependable design techniques and effective methodologies for studying interface fracture behaviour. Several analytical, numerical, and experimental techniques have been employed to investigate the interface fracture phenomenon. The analytical approach becomes highly complex when analyzing composite adherend or adhesive materials exhibiting significant plasticity [1]. In that context, the experimental and numerical procedure is proven effective for analyzing the interface crack propagation.

1.2 Fracture mechanics: Introduction and importance

Fracture represents an unexpected failure in materials and structures. Within the fracture mechanics, failure arises from a crack, described as a fine slit with a narrow opening at its edges. As the crack gradually extends, the stiffness of the structure diminishes, resulting in fracture. Fracture mechanics is a specific branch of engineering science dedicated to investigating the behaviour of structural components when cracks are present, aiming to understand and predict their failure characteristics.

Fracture mechanics emerged as a result of significant catastrophic failures that occurred in the past. These failures were pivotal in transforming fracture mechanics from a collection of scientific concepts into a widely recognized engineering discipline. One such influential event was the failure of the liberty ships during World War II, as shown in **Fig. 1.1**, where numerous

ships experienced ruptures and structural fractures due to stress concentration from poor weld properties. Other notable disasters around the world contributed to the advancement of fracture mechanics, such as the disintegration of the pressurized cabin of the Havilland Comet jetliner in 1954 (shown in **Fig. 1.2**), the Cleveland liquid natural gas storage tank disaster in 1944, and the collapse of the King's Bridge in Melbourne, which happened only a year after its construction in 1962.

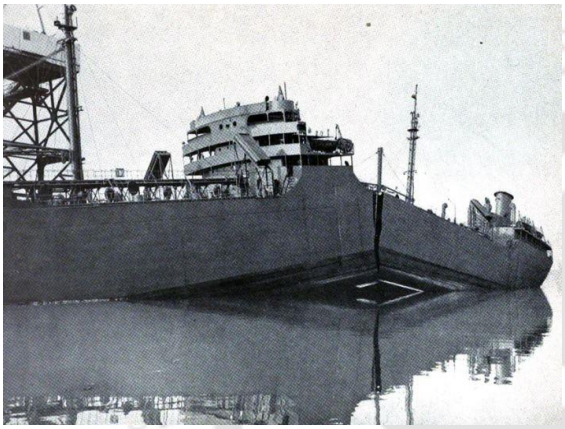

Fig. 1.1 Liberty ship failure (https://www.mathscinotes.com/2018/05/liberty-ship-production-data)

Fig. 1.2 Failure of comet jetliner (https://www.rafmuseum.org.uk/research/archive-exhibitions/comet-the-worlds-first-jet-airliner/comet-failure/)

The foundation of fracture mechanics can be traced back to the work of Inglis [2], who examined the stress distribution around an elliptical hole in an infinite plate under tensile loading. Building upon Inglis' work, Griffith [3] used an energy balance approach to analyze the fracture phenomenon in cracked bodies. This analysis, employing the continuum mechanics approach, represented the initial investigation into the relationship between crack length and the load-bearing capacity of structures. However, the development of fracture mechanics as an engineering discipline was propelled by the contributions of Irwin and his colleagues [4], who extensively studied the failure of liberty ships. Additionally, the work of Westergaard [5] and Williams [6] in the context of 2D analysis of linear elastic cracked bodies marked significant milestones in the evolution of fracture mechanics.

The study of fracture mechanics can be broadly divided into two main categories: brittle and ductile fractures. Brittle fracture, also called elastic and cleavage fracture, shows minimal plastic deformation at the crack tip. This fracture type is hazardous as it can happen well below

the component's design stress and at high speeds without any morning signs. On the contrary, ductile fracture is characterized by a gradual propagation of cracks accompanied by significant plastic deformation in the region surrounding the crack tip. This plastic deformation enables the material to withstand higher loads, providing greater resistance to failure than brittle materials.

Fracture mechanics provides a framework for predicting the strength and durability of structures and designing materials with improved resistance to fracture. It can be divided into linear elastic and elastic-plastic fracture mechanics (LEFM and EPFM). The LEFM assumes that the material response is linearly elastic with a negligible plastic zone size around the crack tip. It uses simple failure criteria (Griffith [7] and Irwin's [8] assumption) to study the crack growth. Unlike linear elastic fracture mechanics, EPFM considers plasticity and large material deformations around the crack tip. The local stress field near the crack tip and the crack propagation behaviour in LEFM is defined using the SIF. However, determining SIF is not simple for interface crack growth studies. To address these issues, critical values of fracture toughness and strain energy released rate (SERR) are used to analyze bonded joints or composite laminate [9–11].

1.3 Overview of an interface crack in an isotropic medium

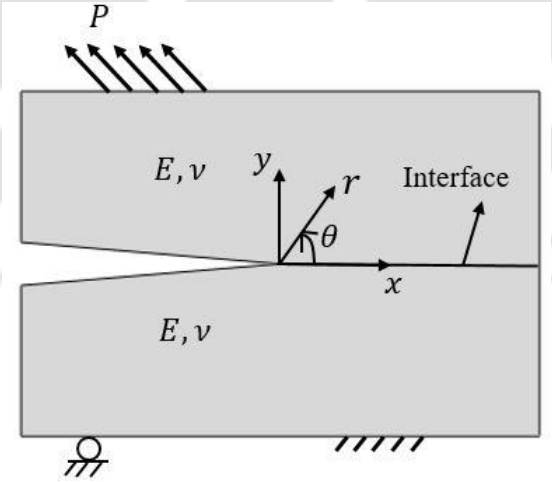

Fig. 1.3 Interface crack in an isotropic material

The interface cracks within isotropic materials display uniform crack growth patterns and deformation behaviour. This particular behaviour simplifies the process of analysis and prediction, which is particularly significant within the context of fracture mechanics to analyze

most of the engineering materials. Isotropic interface crack is prominent in many engineering materials, such as metal and polymer interfaces. A schematic of an isotropic interface crack is shown in **Fig. 1.3.**

The stress intensity factor (SIF) and the energy release rate (ERR) are the two essential parameters within the context of linear elastic fracture mechanics (LEFM) for analyzing the interface crack propagation. The SIF characterizes the stress field around the crack tip, representing a driving force for the crack propagation. The crack propagates once the SIF at the crack tip exceeds the fracture toughness of the material.

The ERR represents the energy released when the crack moves along an interface. This value signifies the potential energy released as the crack progresses. It is a crucial indicator for the crack extension. Understanding the critical ERR offers valuable information on the impetus behind crack propagation and is a significant factor for assessing the fracture behaviour of adhesively bonded joints and the laminated interface.

It is important to note that although the LEFM forms a solid basis for understanding isotropic crack propagation, it possesses a few limitations. The LEFM principles are used to analyze the linear elastic behaviour with small-scale yielding conditions. Employing more advanced fracture mechanics theories, such as elastic-plastic fracture mechanics (EPFM), is more beneficial for materials exhibiting substantial plastic deformation at the crack tip or yielding on a larger scale.

1.3.1 Experimental Methodologies for analyzing the interface crack propagation

Experimental procedures involve the physical testing of material in real-world situations. The adhesively bonded joints and composite laminate often display complex interface behaviour due to material non-linearity and time-dependent effects. Experimental methods can capture all these failure modes and intricate failure mechanisms. It provides a detailed understanding of improving the interface behaviour with optimal material selection. Though time-consuming experimental methods can be used for refining and validating the analytical results wherever applicable, this comparison can help to improve the reliability and accuracy of the analytical models.

Several commonly employed test methods to anticipate the interface fracture toughness of adhesively bonded joints and composite laminates include the double cantilever beam (DCB) test for mode I, the End-notched flexure (ENF) test for mode II, and the mixed-mode bending (MMB) test, which simulates mixed-mode (I/II) fracture behaviour. Moreover, the standard lap shear test and the short beam shear (SBS) test method are commonly utilized to evaluate shear strength in adhesively bonded joints and composite laminates. Digital image correlation (DIC) and acoustic emission (AE) monitoring techniques can also be coupled with these test methods to track crack propagation in real-time.

Standardized testing approaches ideally adhere to established guidelines and specifications, enabling direct comparison of results across different research facilities. These methods are built upon expert knowledge, with meticulous validation and refinement over time. Generally, standardized testing procedures are uncomplicated and can be executed using conventional experimental setups compared to other non-standard methodologies. Despite these benefits, non-standard testing procedures are commonly incorporated to capture specific fracture behaviour with unique design considerations. The compact mixed-mode (CMM) fracture test is a prominent non-standard technique frequently employed in recent years to estimate the failure behaviour of adhesively bonded joints.

1.3.2 Different approaches for analyzing the crack propagation within the context of finite element method (FEM)

Several approaches have accounted for crack propagation analysis within the context of FE: continuum mechanics, fracture mechanics, and damage mechanics [12]. The main principle of continuum mechanics is using an appropriate failure criterion to compare stress, strain, and energy values developed in a material with their maximum permissible values. It assumes that structures are void-free and continuous, which overlooks the influence of microstructural characteristics, such as grain boundaries, dislocations, and voids that considerably influence the crack initiation and its propagation. Moreover, the continuum approach fails to provide solutions for singular points caused by amplified stress and strain values. Therefore, researchers have adopted fracture mechanics-based approach to investigate the failure behaviour of structures with cracks.

The virtual crack closure technique (VCCT) is a popular method used within the LEFM framework. The VCCT assumes that the amount of potential energy released as the crack extends is identical to the virtual work required to close the crack back to its original state [13]. The technique estimates the energy release rate by analyzing nodal forces and displacements of every individual node under particular loading conditions. The VCCT has limitations regarding shorter cracks, as it assumes uniform nodal force values along the crack path [14]. In addition, determining SIFs using the VCCT for a bi-material interface crack is not straightforward due to coupled SIFs [15].

The extended finite element method (XFEM) is a recently developed technique adopted in the FE tools for modelling 2D crack initiation and growth. Since its inception in the 1990s [16], it has evolved to handle various complexities, including modelling cracks with multiple branching [17], modelling finite deformation with discontinuities [18], and mixed-mode fatigue crack growth studies [19]. Although the XFEM does not require re-meshing methodology, it introduces computational complexity due to the incorporation of local enrichment functions. The local enrichment functions are dependent on the type of problem considered. They are obtained from the analytical solutions which are not readily available for complex 2D and 3D scenarios [20].

The EPFM, in contrast to the LEFM, considers the non-linear behaviour of materials beyond their elastic limit. It offers a framework for predicting crack propagation in structures that undergo significant plastic deformation before its failure. Here, the energy needed for crack growth is assessed using the *J*-integral [21], encompassing both elastic and plastic deformation near the crack tip. The EPFM approach, therefore, can be applied to materials exhibiting significant plastic deformation, such as many metals and certain classes of polymers. However, all these fracture mechanics-based methods need the presence of an initial crack and involve higher computational time for accurate results [12].

Addressing the issue of interface fracture necessitates more intricate and precise predictions of failure, aiming to overcome the limitations associated with the approaches above. Interface fracture can be perceived as damage characterized by the formation of micro-cracks or voids. The damage can be quantified in terms of damage variables depending on stresses, strain, moduli, strain rates, Poisson's ratio, etc. [22]. Damage mechanics permits the progressive

accumulation of damage that results in stiffness degradation that progressively leading to the final failure of the structure [23]. This field remains at the forefront of innovation, with ongoing advancements focused on refining modelling techniques, improving robustness, and resolving convergence-related challenges [24].

The techniques used for damage modelling can be classified into two main categories: local and continuum approaches. In the local approach, damage is assumed to be confined to a zero-thickness plane or surface. This approach enables the modelling of an interface failure, such as the failure between the adhesive bond line and the adherend [25] or the interlaminar (delamination) failure in laminated composites [26]. On the other hand, the continuum approach allows for the modelling of damage within a solid finite element, which enables the simulation of bulk failure [27] or the failure along the bond line of an adhesive [28].

Although the numerical implementation of the fracture mechanics-based approach achieved greater success, simulating complex crack growth, including branching and coalescence of crack, is difficult to capture using classical fracture mechanics-based approaches. Many modern adhesives exhibit larger plastic deformation zones, so analyzing them using classical fracture criteria may lead to erroneous results. The cohesive zone model (CZM) is computationally convenient to implement using the FE tools. This flexibility enables the researchers to optimize the design and explore the failure scenarios efficiently. CZM can be implemented using local and continuum approaches to investigate the interface damage under a variety of loading conditions.

1.4 Cohesive zone model (CZM)

In recent times, the CZM has emerged as a popular computational tool to approximate the non-linear fracture behaviour in engineering materials and structures. In the CZM, a thin band with a minimal thickness, known as a "cohesive zone," is assumed to exist just ahead of the crack tip, as shown in **Fig. 1.4**. Within this zone, the cohesive interaction between the fracture surfaces is defined using a cohesive law or traction separation law (T-S-L). The T-S-L signifies the variation of cohesive traction with the separation along the length of the cohesive zone. The crack growth occurs once the cohesive separation reaches its critical separation or the cohesive traction goes down to zero.

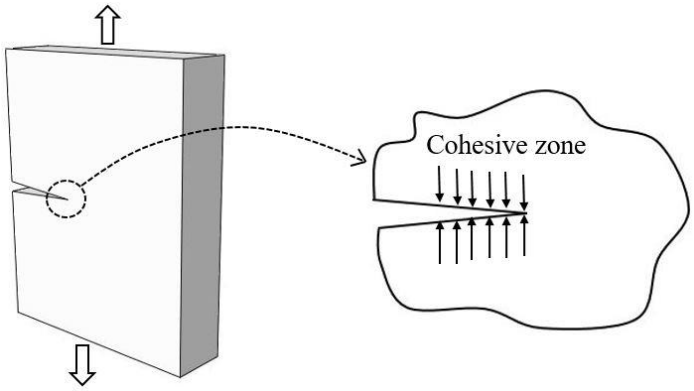

Fig. 1.4 Schematics of a cohesive zone model

1.4.1 Initial development

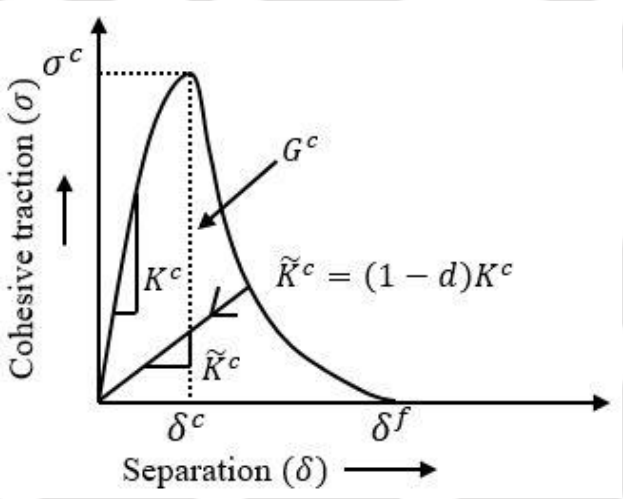

Fig. 1.5 Cohesive traction-separation law (T-S-L)

The CZM has been employed to mitigate stress singularity in the LEFM and to approximate non-linear failure phenomena. In that aspect, Elliott [29] has introduced the concept of interatomic force per unit area to investigate the non-linear failure behaviour of crystalline substances. Barenblatt [30] introduced the cohesive zone concept in the context of brittle failure behaviour. Additionally, the strip yield model developed by Dugdale [31] is viewed as analogous to the CZM, where the yield zone of a steel sheet is regarded as the cohesive zone.

The cohesive T-S-L is utilized to characterize the fundamental behaviour of the cohesive zone along an interface. Any cohesive law has three influential parameters: stiffness (K^c), damage initiation stress (σ^c) in the cohesive zone, and fracture energy (G^c), as shown in **Fig. 1.5**. The cohesive stiffness represents the slope of the traction-separation curve in the elastic region until it reaches the damage initiation stress. Once damage initiation occurs, the cohesive

stiffness deteriorates to $(1-d)K^c$, reducing the cohesive traction with an increase in the separation. The cohesive traction approaches zero value at the critical separation, indicating complete failure.

The cohesive zone parameters are determined through either iterative numerical methods or customized experimental techniques. Various cohesive laws have been proposed to simulate the failure behaviour of the material interfaces. These include the linear softening cohesive law by Camacho and Ortiz [32], the cubic polynomial and exponential cohesive law by Needleman [33] and Xu and Needleman [34], the trapezoidal cohesive law by He and Hutchinson [35], and the polynomial cohesive law by Park et al. [36].

1.4.2 Applications of CZM

The CZM has been widely used in various engineering and structural fields, covering areas such as adhesive joining, laminated composites, microelectronic device analysis, and crack propagation in rock mechanics [37]. Researchers have employed the CZM concept to gain insights into the strength and durability of bonded joints, allowing them to optimize the bonding processes.

The CZM can also simulate fatigue crack growth in engineering materials. Incorporating cohesive elements along potential failure paths, the CZM allows us to predict failure mechanisms and estimate fatigue life under cyclic loading conditions. The application of fatigue within the framework of CZM has gained significant attention and development in the past decade regarding reduced time and cost. However, determining the number of cycles required for damage initiation is challenging, as fatigue life depends on various factors such as material properties, specimen geometry, stress ratio, and testing conditions.

1.4.3 Different types of CZM

The CZM can be categorized into two types based on the relationship between cohesive traction and separation: the potential-based and the non-potential-based CZMs. The potential-based CZMs, such as those developed by Needleman [33], Xu and Needleman [34], and Park et al. [36], utilize a potential function to describe the behaviour of the fracture surface [37]. The cohesive traction values are determined by the first derivative of the potential with respect to separation, while the second derivative provides the constitutive response across the fracture surface. For a potential-based CZM, the cohesive traction must fulfill the symmetry and anti-

symmetry [36] conditions. On the other hand, the non-potential-based cohesive models are simpler to develop as the cohesive traction does not need to adhere to the symmetry and anti-symmetry requirements [38].

1.4.4 Selection of the shape of the T-S-L

In the CZM, it is desirable to customize the shape of the cohesive law to accurately represent the behaviour of the interface or adhesive being simulated. The selection of the specific shape of the T-S-L depends on user's understanding and knowledge of the interface properties. However, it is essential to note that even with slight variations in the parameters of the CZM, different cohesive laws can produce load-displacement responses that are practically indistinguishable [24].

When considering the suitability of cohesive laws, a trapezoidal law is commonly favored for simulating the failure of a ductile adhesive [39,40]. Likewise, a triangular cohesive law is beneficial when dealing with a brittle material interface that experiences minimal plasticity after yielding [41,42]. The triangular cohesive law also effectively predicts failures of composite interfaces because of their inherent brittleness. Consequently, the exponential softening cohesive law is mainly used for predicting the material interface with reasonable ductility. Although a trapezoidal cohesive law is ideal for capturing the desired behaviour, it can present challenges in terms of convergence due to abrupt changes in the cohesive stiffness during the softening process, unlike the smoother transition provided by the triangular cohesive law.

1.4.5 Advantages and limitations

Using the CZM allows researchers to incorporate damage initiation and propagation within a single model, which in turn helps improve the overall structural integrity and reliability of the components [43]. The progressive damage evolution provides a comprehensive understanding of the amount of damage an element undergoes before complete failure. Unlike other methods, the CZM does not require an initial crack for damage propagation, making it suitable for analyzing structures without cracks but with multiple potential crack paths. The ability to capture localized damage facilitates the CZM as a computationally convenient tool for engineering applications [44].

Finally, the CZM is affected by the mesh size used in simulations. To improve accuracy, it is necessary to decrease the mesh size, which increases the computational time. Using a finer

mesh makes it possible to precisely identify the damage initiation and propagation. Additionally, the behaviour of interface failure is influenced by the shape of the cohesive law employed. Different cohesive laws are suitable for specific scenarios, such as triangular cohesive law is used for predicting brittle crack propagation, while trapezoidal cohesive law is more accurate for predicting ductile failure.

1.5 Organization of the Thesis

Chapter 1 introduces the importance of interface fracture and briefly reviews various experimental and computational methods for analyzing interface crack propagation. The fundamentals of CZM are also summarized, outlining its primary benefits and limitations.

Chapter 2 comprehensively reviews the existing literature, discussing the interface crack propagation within adhesively bonded joints and laminated composites and different techniques to improve the interface properties. The chapter also includes various methodologies for determining CZM parameters when subjected to diverse loading conditions.

Chapter 3 of the thesis presents detailed theoretical formulations and numerical procedures to estimate the CZM parameters that remove the crack tip stress singularity.

Chapter 4 describes the experimental methodology of interface crack propagation in adhesively bonded joints under mode I and mode II loading conditions. The influence of multi-walled carbon nanotubes (MWCNTs) on mode II interface fracture of adhesively bonded joints is also presented at the end.

Chapter 5 provides a detailed extrinsic CZM methodology to validate the mode I and mode II crack propagation. Furthermore, the intrinsic CZM parameters are computed for adhesively bonded joints, and a comparison is drawn with the extrinsic CZM parameters under pure mode II loading conditions.

Chapter 6 outlines the experimental procedures used to determine the CZM parameters for investigating composite delamination under mode I and II loading conditions. The chapter also elaborates on the crack propagation in the composite interface under mixed-mode (I/II) loading conditions.

Chapter 7 presents the detailed numerical methodology to validate the load-displacement response of composite laminate under pure mode I, pure mode II, and mixed-mode (I/II) loading.

Chapter 8 concludes the thesis by outlining important conclusions and the scope for future work based on the present study.

Chapter 2 Literature Review

In fracture mechanics, interface fracture refers to the initiation and propagation of cracks along the boundary between two material components. The behaviour of the interface fracture primarily depends upon the presence of defects or irregularities, interface properties, and crack geometry. Research on interface fracture aims to develop strategies that can minimize the occurrence and effects of such fractures and enhance the durability of structures. The literature review initially addresses some of the essential concepts of interface fracture in the context of fracture mechanics. A detailed review of the application of the interface crack propagation, ranging from adhesively bonded joints to laminated composites, the influence of nano-reinforcement on the interface properties, and the dependency of interface parameters on global failure response, is presented in the subsequent section.

Furthermore, the literature review discusses the implementation of the CZM for simulating interface fracture, addressing essential considerations and challenges associated with this approach. Based on the exhaustive literature survey, the potential research gap and the objectives of the present thesis are laid down.

2.1 Parameters in Fracture Mechanics

In the context of fracture mechanics, the potency of an existing crack can be defined using the three mentioned parameters

- Stress intensity factor (K)
- Energy released rate (G)
- Crack opening displacement (COD)

A selection of appropriate parameters depends on the material properties and the crack tip conditions. The parameter K is used in the LEFM analysis, whereas G is useful for both LEFM and EPFM studies.

2.1.1 Stress intensity factor (SIF)

The SIF (K) is a crucial parameter in the LEFM that plays a significant role in characterizing cracks under small-scale yielding (SSY). K is influenced by the crack length and specimen

geometry. Unlike the stress concentration factor, which is the ratio between the maximum stress and the average stress, K describes stress, strain, and displacement field in the vicinity of the crack tip, known as the singularity-dominated region (SDZ).

The concept of the SIF is extensively used to explain most metal fractures within the framework of LEFM. Its practical significance has led to the compilation of the SIF values for various crack configurations in numerous handbooks. By comparing the applied SIF (K) with the critical SIF (K_C or fracture toughness), it becomes possible to predict whether a crack will propagate or remain stable.

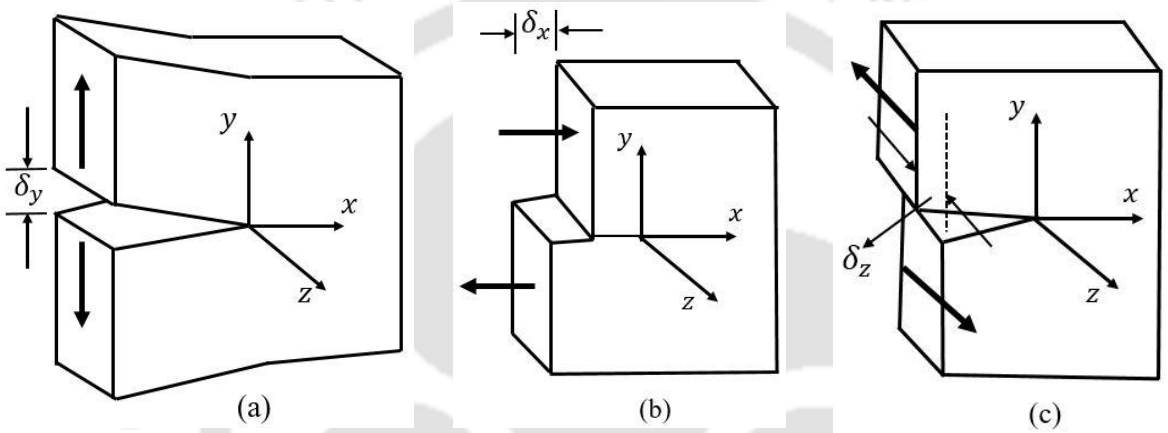

Fig. 2.1 Schematics of basic fracture modes (a) Mode I, (b) Mode II, and (c) Mode III

A crack comprises upper and lower surfaces connected at the crack front, situated at the end between these surfaces. When an external load is applied to a cracked body, the upper and lower surfaces undergo relative movements, described by differences in displacement denoted as δ_x, δ_y, and δ_z between the two surfaces. In this context, the local Cartesian coordinate system (x, y, z) is positioned at the crack front. The $x, y,$ and z axes are perpendicular to the crack front, perpendicular to the crack plane, and aligned along the crack front, respectively, as illustrated in **Fig. 2.1.**

Irwin [8] identified three distinct separations of crack surfaces corresponding to three primary fracture modes: Mode I, Mode II, and Mode III. Each fracture mode represents a specific way in which the crack surfaces can move. The fracture of a cracked body can be described independently as one of these three basic modes or a combination of them.

Mode I (Opening mode): It involves the symmetrical movement of the crack surfaces with respect to the undeformed xz plane, specifically in the y-direction, as shown in **Fig. 2.1 (a)**.

Mode II (Sliding mode): Sliding mode is characterized by the anti-symmetrical movement of the crack surfaces along the xz plane, as shown in **Fig. 2.1 (b)**.

Mode III (Tearing mode): The tearing mode represents the symmetrical movement of the crack surfaces along the z-direction, as shown in **Fig. 2.1 (c)**.

Each of the three fundamental fracture modes can be accurately characterized by the stress present at the leading edge of the crack, also known as the crack tip, within a two-dimensional system. The stresses near the crack tip can be written as $(y = 0, x \to 0^+)$

$$\begin{aligned} \sigma_{yy} &= \frac{K_I}{\sqrt{2\pi x}} + O\left(\sqrt{x}\right), \quad \sigma_{xy} = \sigma_{yz} = 0 \\ \sigma_{xy} &= \frac{K_{II}}{\sqrt{2\pi x}} + O\left(\sqrt{x}\right), \quad \sigma_{yy} = \sigma_{yz} = 0 \\ \sigma_{yz} &= \frac{K_{III}}{\sqrt{2\pi x}} + O\left(\sqrt{x}\right), \quad \sigma_{yy} = \sigma_{xy} = 0 \end{aligned} \tag{2.1}$$

The expression showed that the intensity of stress follows square root singularity with K_I, K_{II}, and K_{III} represents the SIF in opening, sliding, and tearing modes, respectively. Various SIF estimation methods, including experimental, analytical, and numerical approaches, have been developed in the past decades.

2.1.2 Strain energy release rate (SERR)

The SERR (G) quantifies the energy required to form two new surfaces, a key parameter in determining whether a crack will continue to propagate or become stable upon loading. Building upon Griffith's [7] groundbreaking work on metals, Irwin [8] introduced the SERR concept to investigate the crack propagation phenomenon.

The quantity, K_C — critical stress intensity factor (SIF) or G^C — critical strain energy release rate (SERR) at the moment of crack extension is usually defined as fracture toughness,

2.1.3 Crack opening displacement (COD)

The COD serves as an alternative parameter to the *J*-integral when significant plastic deformation occurs relative to the size of the cracked body. Wells [45] introduced the concept

of the COD, which plays a pivotal role in the EPFM. The COD increases as the crack length increases, signifying a more significant propensity for crack propagation.

2.2 Different methods for the determination of SIF of a cracked geometry

2.2.1 Analytical methods

Analytical techniques are primarily suitable for uncomplicated crack geometries and simple boundary conditions. These methods employ the LEFM equations to describe the stress and displacement patterns near the crack tip. Several commonly utilized analytical methods for estimating the SIFs include Laurent series expansion, boundary collocation, integral transform, and weighted function [46]. These analytical approaches hold significance for two main reasons. Firstly, they yield the appropriate stress singularity form and asymptotic solutions, which aid in analyzing experimental observations and enhancing the precision of the numerical outcomes. Secondly, they establish benchmark solutions for straightforward geometries assuming idealized material behaviour, facilitating the validation of numerical and experimental findings.

2.2.2 Numerical methods

Numerical approaches for SIF estimation are valuable for analyzing intricate geometries and boundary conditions commonly encountered in practical applications. These methods prove particularly useful when dealing with complex problem scenarios. The SIFs can be estimated using displacement-based or energy-based numerical techniques. Using numerical methods, specifically finite element method (FEM), boundary element method (BEM), and meshfree methods expands the scope of problems that can be addressed through computational approaches. Among the commonly employed methods for SIF estimation, the direct method and the *J*-integral stand out as widely used approaches [47]. These numerical methods enhance the capability to solve a broad range of problems, enabling the analysis of complex crack behaviour and providing reliable results.

(a) Direct method

The direct method, one of the initial techniques developed, uses the stress and displacement fields near the crack tip along the x-axis to estimate the SIF. The stress and displacement values at a specified distance x in front of the crack tip can be expressed as follows.

$$\sigma_{yy} = \frac{K_I}{\sqrt{2\pi x}}, x \to 0^+ \tag{2.2}$$

$$\delta_y = \frac{K_I(\kappa + 1)}{4\mu\pi}\sqrt{-2\pi x}, x \to 0^- \tag{2.3}$$

Thus,

$$K_I = \sigma_{yy}\sqrt{2\pi x}, x \to 0^+ \tag{2.4}$$

$$K_I = \frac{2\mu\delta_y}{\kappa + 1}\sqrt{\frac{2\pi}{-x}}, x \to 0^- \tag{2.5}$$

The x-axis, aligned with the crack direction, is used as a reference. The SIF at any arbitrary distance along x can be obtained by plotting $\sigma_{yy}\sqrt{2\pi x}(\delta_y\sqrt{\frac{2\pi}{-x}})$ versus $x(-x)$ using the data $\sigma_{yy}(u_y)$ obtained from the FE solution. Typically, the displacement solution provides a more precise estimation of the SIF. Here, μ and κ are the shear modulus and Kolosov constant, respectively.

However, these techniques require more FE meshes around the crack tip to obtain more accurate results. Using a finer mesh may yield a significant degree of freedom, thus increasing the computation time. Another alternative approach is to use the singular finite elements to surround the crack tip, which contains proper $r^{-\frac{1}{2}}$ stress singularity terms in the displacement function. Using singular elements allows one to use coarse mesh in the crack tip region.

(b) *J*-integral/Interaction integral

While dealing with elastic-plastic deformation, the principles of LEFM become inadequate due to the considerable plasticity near the crack tip. To address this, Rice [48,49] introduced the concept of *J*-integral. *J*-integral is path-independent and finds extensive use in studying elastic-plastic fracture of ductile materials. Like other parameters (G and K), the *J*-integral is essential to characterize cracks. In fact, G is a particular class of *J*-integral, i.e., G is valid for the linear elastic material. In contrast, *J*-integral is applicable to linear and non-linear elastic material and is also useful for characterizing material that exhibits elastic-plastic behaviour near the crack tip.

For a 2-D crack problem, the *J*-integral is defined as

$$J = \lim_{\Gamma \to 0} \int_{\Gamma} \left(W \delta_{1i} - \sigma_{ij} u_{j,1} \right) n_i \mathrm{d}\Gamma \tag{2.6}$$

where W and δ_{1i} represent strain energy density (SED) and Kronecker delta, respectively. $u_{j,1}$ defines the derivative of the displacement component u_j with respect to the coordinate x_1. n_i represents the outward normal to the contour Γ as shown in **Fig. 2.2**. For a problem of linear elasticity, the SED $W = \sigma_{ij}\epsilon_{ij}/2$, where σ_{ij} and ϵ_{ij} signifies the component of stress and strain tensor, respectively.

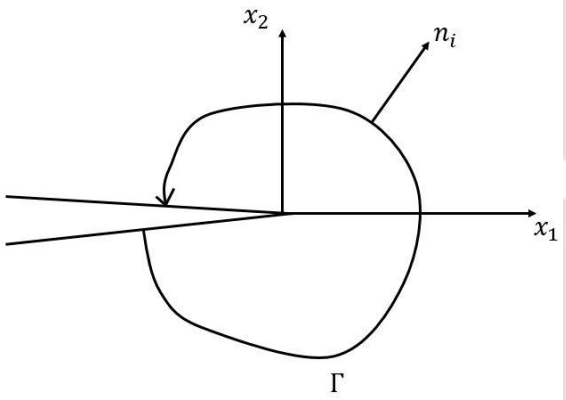

Fig. 2.2 Integral path around the crack tip

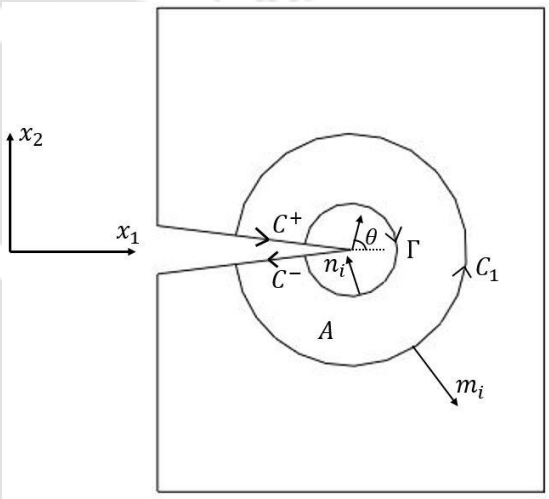

Fig. 2.3 Crack path for interaction integral with crack face traction

It is important to note that from a single value of *J*-integral, the two SIFs in mode I (K_I) and mode II (K_{II}) cannot be separated. The initial successful attempt to decouple the mixed-mode SIFs was carried out by Stern et al. [50] by establishing a two-state integral based on Betti's reciprocal theorem. The two-state integral is a contour integral with respect to the integrand $(u_i t_i^{aux} - u_i^{aux} t_i)$, where t_i^{aux} and u_i^{aux} define the auxiliary traction and displacement vector, respectively.

Superimposing the actual and auxiliary state from Eq. (2.6), we can obtain

$$\begin{aligned} J(u_i + u_i^{aux}) = \lim_{\Gamma \to 0} \int_{\Gamma} \frac{1}{2} \{ & \left(\sigma_{jk} + \sigma_{jk}^{aux} \right) \left(\epsilon_{jk} + \epsilon_{jk}^{aux} \right) \delta_{1i} \\ & - \left(\sigma_{ij} + \sigma_{ij}^{aux} \right) \left(u_{j,1} + u_{j,1}^{aux} \right) \} n_i \mathrm{d}\Gamma \end{aligned} \tag{2.7}$$

Eq. (2.7) can be rewritten as

$$J(u_i + u_i^{aux}) = J(u_i) + J(u_i^{aux}) + I \tag{2.8}$$

where $J(u_i)$ and $J(u_i^{aux})$ are the J-integral corresponding to the actual and the auxiliary field, respectively. I define the cross-term or interaction integral term. The interaction integral term is defined as

$$I = \lim_{\Gamma \to 0} \int_{\Gamma} P_{1i} n_i \mathrm{d}\Gamma \tag{2.9}$$

where P_{1i} is the mutual energy-momentum tensor expressed as

$$P_{1i} = \frac{1}{2}\left(\sigma_{jk}\epsilon_{jk}^{aux} + \sigma_{jk}^{aux}\epsilon_{jk}\right)\delta_{1,i} - \sigma_{ij}^{aux}u_{j,1} - \sigma_{ij}u_{j,1}^{aux} \tag{2.10}$$

In the presence of crack face traction, the expression for interaction integral is given as

$$I = \int_A \left[\sigma_{ij}u_{j,1}^{aux} + \sigma_{ij}^{aux}u_{j,1} - \frac{1}{2}\left(\sigma_{jk}\varepsilon_{jk}^{aux} + \sigma_{jk}^{aux}\varepsilon_{jk}\right)\delta_{1,i}\right] q_{,i}\mathrm{d}A - \int_{C^+ + C^-} (t_j u_{j,1}^{aux}) q \mathrm{dC} \tag{2.11}$$

where t_j represents the cohesive traction acting on the crack surfaces C^+ and C^-, as shown in **Fig. 2.3**. q is a smoothly increasing function with values of zero in C_1 and unity in Γ.

2.2.3 Experimental methods

Experimental techniques involve conducting physical tests on specimens that contain pre-existing cracks, subjecting them to controlled loading conditions, and thereby accurately determining the SIF. The analytical methods for SIF determination often rely on simplifying assumptions that may deviate from real-world situations. Therefore, experimental validation is necessary to ensure that such idealizations do not unduly distort the fundamental aspects of the problem. Several commonly employed experimental methods include caustics, Moire interferometry, photoelasticity, and strain gauge techniques [51]. These experimental approaches provide valuable insights into the behaviour of cracks and can be used to validate the accuracy of analytical models and assumptions.

2.3 Crack propagation in adhesively bonded joints — Experimental and Numerical studies

In recent times, adhesively bonded joints have gained significant popularity because of their reduced weight, improved resistance to fatigue, flexible design possibilities, and durability [52–54]. As a result, these joints have found widespread use in the aerospace, automotive, and infrastructure industries.

The properties of adhesively bonded joints are greatly influenced by the adhesive thickness, adhesive type, surface preparation, bonding pressure, curing conditions, and environmental factors like temperature and humidity [55]. Gleich et al. [56] conducted a study to examine the influence of the bond line thickness on the performance of the adhesively bonded joints. The experimental findings revealed that the ideal adhesive thickness for optimal joint strength is 0.1-0.2 mm. However, commonly used analytical methods for adhesive joint analysis tend to show increased joint strength with greater adhesive thickness. This discrepancy can be attributed to the through-the-thickness stress distribution within the adhesive. Han et al. [57] investigated the influence of adhesive thickness on the mode I energy release rate of the adhesively bonded joints. The mode I fracture energy initially increased and afterward diminished with increased adhesive layer thickness in the selected range of 0.2-1 mm. Increasing the bond line thickness increases the possibility of internal flaws that result in reduced joint strength.

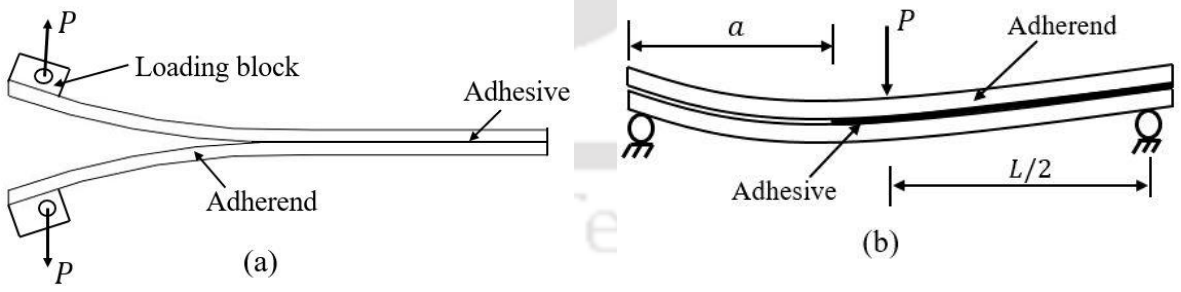

Fig. 2.4 (a) DCB and (b)ENF test configuration

Rahmani and Choupani [58] examined the performance of adhesively bonded joints at low temperatures. They observed that the ultimate tensile strength (UTS), yield strength, and elastic modulus of the joints increased as the temperature decreased. The critical SIF and the ERR

follow the same trend with decreasing temperature. However, the effect of temperature on mode I was less pronounced than on mode II.

Several test methods have been employed to investigate the fracture energy of adhesively bonded joints, namely the DCB test for mode I and the ENF test for mode II, as shown in **Fig. 2.4**. Andersson and Biel [59] conducted an experimental study to determine the effective properties of adhesive in the DCB test. They utilized a stress elongation relationship derived from the experiment, which represents the derivative of the ERR with respect to the elongation of the adhesive layer. Marzi et al. [60] investigated the influence of different adhesive thicknesses on fracture properties. They performed experiments using the DCB and tapered DCB test methods to examine the mode I fracture properties. The ENF and end-loaded shear joint (ELSJ) test methods were used to investigate fracture under the mode II loading conditions. It was observed that the fracture energy also increased as the adhesive layer thickness increased. For smaller adhesive thicknesses, the results were consistent across all test methods. However, the results showed a significant variation while dealing with larger adhesive thicknesses. Chaves et al. [61] reviewed and summarized all fracture characterization tests to investigate the mode I and mode II energy-released rates of adhesively bonded joints. The mixed-mode (I/II) tests were also carried out to examine the influence of specimen geometry for a range of mixed-mode ratios.

The testing mentioned above has limited utility due to the difficulties in obtaining a wide range of mixed-mode ratios. Moreover, different specimen geometries are required to analyze fracture toughness in each mode. Choupani [11] developed Arcan specimens with various combinations of adhesive, composite, and metallic adherends to address this issue. These specimens were subjected to loading in a specific fixture, with the loading angle ranging from 0° to 90°. By conducting experimental analysis, the fracture toughness was estimated under mixed-mode loading conditions. In another work, Choupani [62] employed the FE analysis for an identical specimen configuration and loading setup to calculate the SIF for different types of bonded joints using finite correction factor methods. The fracture toughness test results indicated that the fracture toughness in shearing mode was higher than in the opening mode. Consequently, several criteria for mixed-mode conditions were examined and compared with experimental observations. Pang and Seetoh [63] manufactured CMM specimens to evaluate

fracture toughness under pure mode I, mode II, and mixed-mode loading conditions. They also conducted a numerical investigation to explore the effects of adhesive layer thickness, crack length ratio, and the angle of fracture mode on the failure characteristics of bonded joints.

Within the context of the FE analysis, Jokinen et al. [64] investigated the applicability of the VCCT to study the crack growth analysis of adhesively bonded joints with ductile adhesive. Initially, the mode I fracture energy was evaluated for a pre-cracked DCB specimen, assuming a linear elastic behaviour of the adhesive. The ERR for a ductile adhesive is then evaluated by conducting a non-linear analysis with a plastic material model for the adhesive and comparing numerical and experimental results. Senthil et al. [65] used the VCCT to investigate damage initiation in adhesively bonded composite joints under compressive load. Mixed-mode failure criteria were also utilized to examine the influence of crack shape, size, and location on the failure behaviour of the joints.

Another alternate method to analyze the debond growth is the CZM. The CZM relies on principles of damage mechanics and employs a cohesive law to investigate the initiation and propagation of damage within the bonded joints. De Moura et al. [66] used a crack equivalent concept to estimate the fracture energy of adhesively bonded joints under pure mode I loading conditions. This novel approach was subsequently compared to a traditional data reduction method and validated using a trapezoidal CZM. The remarkable consistency observed between the numerical and experimental results is compelling evidence for the effectiveness of the proposed method. Campilho et al. [67] investigate the influence of different cohesive laws (triangular, trapezoidal, or exponential) on the strength prediction in single-lap adhesively bonded joints. The study reveals that cohesive law has a notable effect, particularly for shorter overlap lengths. Specifically, a trapezoidal cohesive law demonstrates the closest agreement with experimental data when a ductile adhesive is employed.

Conversely, the shape of the cohesive law has minimal influence on brittle adhesively bonded joints. Sadeghi et al. [68] investigated the applicability of four different FE techniques — cohesive element, surface-based cohesive behaviour, XFEM, and VCCT for analyzing the failure behaviour of single lap joints. The experiments involved two bond line thicknesses, measuring 0.2 mm and 0.9 mm. The findings indicate a clear trend where an increase in bond line thickness correlates with a decrease in the peak load. The reduction in peak load may be

due to increased secondary bending moment induced in the joints. Moreover, the plane strain elements always lead to a higher load-displacement response stiffness than the plane stress elements.

2.4 Composite material — a brief overview

"Composites" refers to a class of materials formed by combining two or more individual materials, each with unique physical and chemical properties. When these distinct components are brought together, they interact in such a way that it produces a synergistic effect, resulting in composite materials that exhibit enhanced characteristics compared to the individual components.

Composites comprise two primary elements: the matrix and the reinforcement. These components play distinct roles in the overall structure and properties of the composite material. The matrix, commonly made of polymers, metals, or ceramics, acts as a binding agent or a surrounding medium that holds the reinforcement in place. It provides a stable framework and ensures the cohesion of the composite. The reinforcement component of composites can take various forms, such as fibers, flakes, or particles. These reinforcements are incorporated into the matrix to enhance specific properties of the composite. For example, fiber reinforcements, such as carbon fibers or fiberglass, are known for their high strength and stiffness. When embedded within the matrix, they contribute to the overall mechanical strength, rigidity, and load-bearing capacity of the composite.

2.4.1 Classification of Composites

Matrix is a binding agent that plays a pivotal role in providing cohesion with the fiber. Based on the type of matrix, the composite can be classified as

- **Polymer matrix composites (PMCs):** PMCs comprise polymer matrices, including epoxy, vinyl ester, or polyester, combined with various fiber reinforcements like carbon, glass, and aramid. They exhibit low density and offer exceptional resistance against corrosion. PMCs are extensively used in the automotive and aerospace sectors.
- **Metal matrix composites (MMCs):** MMCs utilize metal matrices such as aluminum, magnesium, and titanium. These composites exhibit enhanced conductivity, strength,

and improved thermal stability. MMCs find extensive applications in the automotive, aerospace, and electronic industries.

- **Ceramic matrix composites (CMCs):** CMCs employ ceramic matrices like alumina and silicon carbide. These composites offer exceptional thermal stability and resistance to wear. CMCs find wide applications in defense applications and thermal management systems.
- **Carbon matrix composites (CMCs):** CMCs comprise carbon fibers embedded within a carbon matrix. These composites provide excellent strength, stiffness, and exceptional thermal conductivity. CMCs find extensive defense and aerospace applications due to their superior properties.

Based on the type of reinforcement, composites are classified as

- **Fiber-reinforced composites (FRCs):** This composite type utilizes fibers as reinforcement. Examples of commonly employed fiber-reinforced composites (FRCs) are carbon fiber-reinforced plastic (CFRP), glass fiber-reinforced plastic (GFRP), and aramid fiber-reinforced plastic (AFRP) composites. These composites exhibit an excellent strength-to-weight ratio and find widespread use in the automobile and aerospace industries.
- **Particulate reinforced composites (PRCs):** PRCs consist of metal, ceramic, or polymer particle matrices. These composites improve wear resistance, hardness, and dimensional stability.
- **Laminated composites:** Laminated composites are created by layering multiple lamina, primarily fiber-reinforced composites with varying orientations. These layers are bonded together to create a composite material with customized properties.
- **Hybrid composites:** Hybrid composites combine different fibers, such as carbon and glass, into a single composite structure. It can achieve a desirable balance of stiffness, strength, and cost-effectiveness by incorporating various fibers.

The different types of composites based on the reinforcement are schematically shown in **Fig. 2.5.**

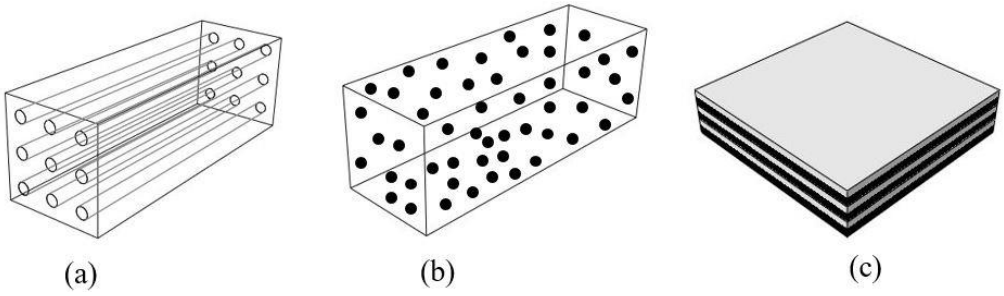

Fig. 2.5 Classification of composites (a) Fiber-reinforced, (b) Particulate reinforced, and (c) Laminated composites

2.5 Composite delamination — Experimental and Numerical studies

Fiber-reinforced composites have been extensively used in automobile, aerospace, and structural applications in recent decades due to their impressive strength-to-weight ratios and superior stiffness. Despite all these benefits, they are susceptible to delamination due to their limited interlaminar properties [69–71]. As shown in **Fig. 2.6**, delamination often arises from low-velocity impact and geometric inconsistencies that emerge during fabrication. This delamination can compromise the strength and stiffness of the composite, leading to the possibility of a catastrophic failure. It is crucial to thoroughly understand the behaviour of delamination in composite laminates to ensure fail-safe designs and maintain the component's structural integrity.

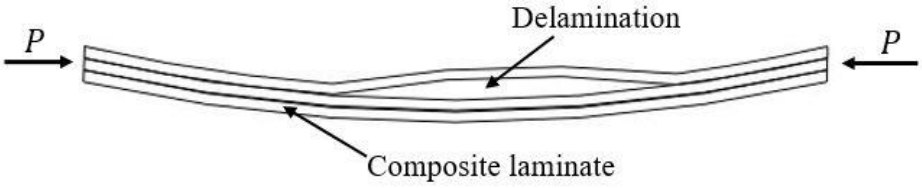

Fig. 2.6 Delamination

The delamination behaviour of the laminated composite primarily depends on the compatibility between the fiber and the matrix, fiber orientation, and environmental factors (temperature, moisture, humidity, etc.) [72,73]. Asp [74] investigated the influence of moisture and temperature on the delamination behaviour of carbon fiber-reinforced epoxy composites under pure mode I, mode II, and mixed-mode (I/II) loading conditions. The mode I strain energy release rate is unaffected, whereas the mode II and mixed-mode ERR decreased with increased moisture content. However, an increase in temperature results in marginal improvement of the mode I and mode II energy release rates.

Tan et al. [70] investigated the influence of interface properties on the interlaminar and intralaminar damage behaviour of unidirectional composite laminate. Composites with different interlaminar properties were fabricated using an autoclave under curing pressure ranging from 0 to 0.8 MPa. The interlaminar shear strength of the composite is measured by conducting a SBS test. The interface shear strength increased, whereas the void content decreased with increased curing pressure.

Lucas [75] investigated the effect of fiber orientation on the delamination fracture toughness of continuous fiber-reinforced composites. The fracture toughness was estimated for graphite/epoxy composite laminate by varying the fiber orientation from 0^0 to 90^0 with respect to the crack direction. It is observed that the fracture toughness of the composite laminate increased with an increase in the fiber orientation. It can be due to crack tip bifurcation, deflection, and twisting. Such deviant crack-tip behaviour can be attributed to the rise in mixed-mode fracture toughness.

Considerable focus has been dedicated to numerical investigations to explore the delamination mechanism. Morais et al. [76] used the VCCT to simulate the propagation of cracks using a predefined path. They conducted the DCB tests on carbon/epoxy $[0/90]_{12}$ composite samples as part of their experimental research. These tests revealed intralaminar and interlaminar delamination within the 90^0 mid-layer and along the [0/90] interface. The numerical observations indicated a noteworthy disparity between the intralaminar and interlaminar fracture toughness. Consequently, interlaminar crack propagation was impeded due to the significantly lower intralaminar fracture toughness.

Zhao et al. [77] employed four models based on the XFEM to forecast the growth of delamination in laminated composites subjected to mode I loading. They devised a novel model for crack initiation, utilizing quadratic stress criteria with the crack growth direction perpendicular to the maximum principal stress. Comparing the experimental results with all four delamination growth models, the mode I delamination along the zigzag path was investigated. The delamination growth model incorporating a mixed-mode damage evolution law and a critical fracture toughness function displayed the highest level of agreement with the experimental results.

The CZM has been recognized as a promising tool for predicting delamination in composite laminates. The primary advantages of the CZM are its straightforward and uncomplicated implementation, eliminating the need for an initial crack. Turon et al. [78] developed an accurate simulation methodology for predicting the mixed-mode delamination of laminated composites. A relationship between the interlaminar strength and the penalty stiffness was proposed to consider changes in local mode ratios during damage evolution. The proposed model was validated with the corresponding analytical solutions for different mixed-mode ratios. Lu et al. [79] systematically investigated the influence of cohesive element parameters on progressive damage and failure load. Through varying the cohesive strength in their finite element (FE) analysis, the researchers identified two types of failure behaviour: strength-sensitive and strength-insensitive, which were influenced by the geometry and ply layup of the composite material. The penalty stiffness of the cohesive element mainly affects the computational accuracy and efficiency in delamination modelling. Too low penalty stiffness delayed the damage initiation, whereas high stiffness increased the computational time. Zhao et al. [80] proposed a numerical model to accurately simulate the mode I and mixed-mode delamination of multidirectional laminate. A fracture toughness function is derived that depends on crack growth length and reflects the variations of fiber bridging tractions. The predicted delamination behaviour with interface $0^0/5^0$, $45^0/\text{-}45^0$, and $90^0/90^0$ in both the DCB and the MMB results were consistent with the experimental observations.

2.6 Influence of nano-reinforcements on improving the interface properties of adhesively bonded joints/laminated structures

Interface fracture poses a significant challenge in the design of adhesively bonded joints and laminated structures. Incorporating nano-scale fillers into the adhesive has emerged as a practical approach to enhance the mechanical properties of such joints [81–83]. Nanofillers like graphene, carbon nanotubes (CNTs), and silicon carbide have been widely utilized to join structural elements and strengthen interfaces in composite materials. The exceptional strength and stiffness of CNTs, stemming from their unique atomic structures, make them particularly well-suited for improving the interface properties of bonded joints and composite laminates.

Ejaz et al. [81] investigated the influence of multi-walled carbon nanotubes (MWCNTs) on the mechanical properties of adhesively bonded joints. They utilized Araldite 2011 adhesive

and an aluminum adherend to create two types of lap joint configurations: a single lap joint (SLJ) and a double strap lap joint (DSLJ). Including MWCNTs resulted in a significant enhancement in joint strength of the lap joint. When 1 wt.% of non-functionalized MWCNTs were added, the SLJ and the DSLJ exhibited maximum improvements of 60% and 31%, respectively.

Khoramishad et al. [84] studied the combined effect of temperature and the MWCNTs on the shear strength of adhesively bonded joints. They observed that as the testing temperature increased, the beneficial effect of the MWCNTs on the joint strength diminished. However, when the nanofiller content was further increased, it led to agglomeration, which adversely affected the interface properties of the joints. In another significant study, the same authors conducted experiments to investigate the influence of graphene oxide nano-platelets (GONPs) on the performance of bonded joints at elevated temperatures. The temperature range examined encompassed room temperature up to the glass transition temperature, using nanocomposites fabricated with GONP concentrations of 0.1 wt.% and 0.3 wt.%. It was noted that as the testing temperature exceeded a critical threshold, adding GONPs reduced joint strength. The concentration of GONPs played a substantial role in determining this critical temperature level. For specimens containing 0.1 wt.% of GONPs, the estimated critical temperature was 60°C, which decreased to 40°C when the GONP concentration was increased to 0.3 wt.% [85].

The load transfer mechanism between the carbon nanotubes (CNTs) and the polymer directly depends on the effectiveness of the chemical bonding between them. The improper bonding between the CNTs and the polymer leads to CNTs pulling out during delamination, limiting the fracture toughness of the composites [86]. Functionalization helps to produce strong covalent bonds between the CNTs and the polymer matrix, resulting in improved strength and toughness of the composite. Functionalized CNTs have better dispersion ability within the polymer matrix than non-functionalized CNTs. The electric charges of the functionalized CNTs counteract the Van der Walls force of attraction, thus increasing the effective areas of CNTs interacting with the polymer matrix.

Two methods have been employed to incorporate CNTs into fiber matrix composites. The first technique thoroughly mixes CNTs with the matrix, resulting in modifications to the matrix itself. The second method involves modifying the surfaces of the fibers by applying CNTs,

leading to modifications at the interface between the fibers and the matrix. Regarding the matrix modification techniques, Hsiao et al. [87] used two different MWCNTs content of 0.1 wt.% and 0.5 wt.% to fabricate graphite fiber-reinforced epoxy composites. Single-lap shear tests were performed to assess the impact of nanofillers on the adhesive properties, measuring the average shear strength. The results showed a significant enhancement in average shear strength, with a 45.6% increase observed when 0.5 wt.% of MWCNTs were added to the epoxy resin. Tarfaoui et al. [88] investigated the influence of MWCNTs on the mechanical behaviour of textile-based composites. Different volume percentages (pristine, 0.5%, 1%, 2%, and 4%) were used to fabricate three-phased composites composed of carbon fiber, epoxy resin, and MWCNTs. Different sets of experiments consisting of flatwise and open-hole tension tests and short beam tests were performed. The experimental observations showed that the mechanical properties of the composite increased up to 2 wt.% of MWCNTs and decayed beyond that.

Gude et al. [89] examined the strength and toughness of composite joints reinforced with carbon nanotubes (CNTs) in carbon fiber/epoxy composites. They conducted lap shear tests to evaluate the strength and DCB tests to assess toughness. The results indicated that the introduction of carbon nanofibers and nanotubes led to an increase in the fracture energy under mode I loading. At the same time, the lap shear strength remained relatively constant. This enhancement in fracture toughness can be attributed to carbon nanotubes, which facilitated toughening mechanisms.

Furthermore, including nanofillers altered the crack growth behaviour and improved the strength at the interface between the substrate and adhesives. Mujika et al. [90] investigate the influence of the MWCNTs on the interlaminar fracture properties of long carbon fiber composites. They evaluated fracture toughness using a newly proposed test method called "Beam theory including bending rotation effect" in ENF tests. This method offers the advantage of determining the critical ERR at specific points during the test, where stable crack advancement occurs. The findings demonstrated that the dispersion of the MWCNTs resulted in a 22% enhancement in initiation fracture toughness and a 14% improvement in propagation fracture toughness.

2.7 Influence of interface material properties on global load-displacement response

The fracture characteristics of any material and structure can transition from ductile to brittle (shown in **Fig. 2.7**) based on factors such as specimen geometry, material properties, loading conditions, and boundary constraints. Various authors have employed the π theorem of dimensional analysis to investigate the influence of fracture toughness, interface strength, and geometric dimensions on the failure behaviour of the specimen [91,92]. When the brittle fracture occurs, the crack propagation is rapid, followed by a sudden decrease in the load-bearing capacity of the structures. In such scenarios, the concept of LEFM can be used to explain the behaviour of catastrophic failure. Conversely, the EPFM provides a suitable framework in highly ductile cases. Snap-back instability is another rare phenomenon observed primarily in concrete specimens, where load and displacement reverse after reaching the peak load. The CZM can be employed to describe the size effects phenomenon of fracture mechanics and can predict both ductile and brittle interface fracture behaviour.

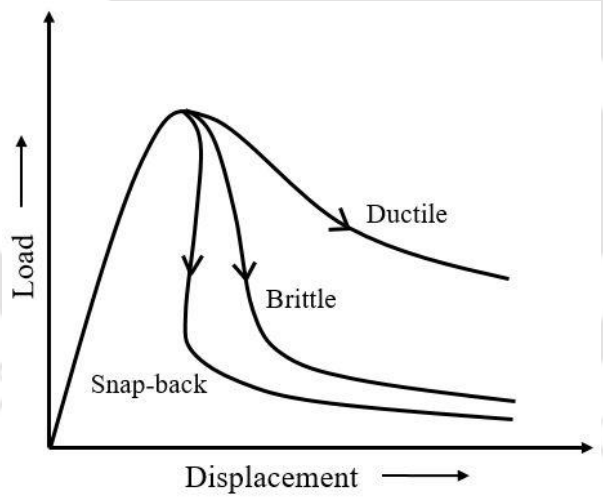

Fig. 2.7 Ductile, Brittle, and Snap-back response

Carpenteri [93] introduced a dimensionless parameter, the Brittleness number (S_E), to analyze the size effect phenomenon and investigated the brittleness of the interface. The Brittleness number for a material interface can be calculated using the following expression.

$$S_E = \frac{G_n^c}{\sigma_n^c b} \tag{2.11}$$

where G_n^c and σ_n^c are the fracture energy and cohesive strength, respectively. b represents the specimen depth. Carpenteri [93] conducted a study using the three-point bending (TPB) test configuration, obtaining a range of load-displacement responses with varying values of the Brittleness number S_E. The ratio between the interface strength (σ_n^c) and Young's modulus (E) was kept constant during the analysis. For specimens with higher brittleness numbers, indicating greater fracture energy G_n^c, and smaller structural size b, the load-displacement response exhibited a ductile behaviour. Conversely, specimens with lower fracture energy and larger structural dimensions exhibited brittle fracture behaviour. Moës and Belytschko [94] used the concepts of brittleness number and the XFEM for simulating the cohesive crack growth in concrete. A range of Brittleness numbers was considered, and the global failure responses were initially validated with the reference results of Carpenteri and Colombo [93] for TPB test configurations. Furthermore, they extended the application of their proposed methodology to analyze the mixed-mode crack growth in concrete during a four-point bending test.

Snap-back is commonly observed in reinforced concrete and a few adhesively bonded structures. Li et al. [95] examined the snap-back instability and crack-trapping effect in adhesively bonded composite joints using DCB specimens with fiber bridging. They specifically focused on the influence of the bridging phase and derived a dimensionless parameter to quantify the intensity of snap-back instability. The effect of substrate thickness and arrangement spacing of the bridging space on snap-back instability and toughening mechanism was also investigated. Lacidogna et al. [96] studied the influence of snap-back on the AE response of rock specimens under compression. The energy is dissipated in brittle crack propagation, and no energy dissipation due to snap-back phenomena is observed. They found that fracture and AE energy are independent qualities, and the AE counts result from the structural local instabilities.

2.8 Theoretical formulations of the CZM

The CZMs can be classified into two types based on their numerical implementation: intrinsic CZMs and extrinsic CZMs. Intrinsic CZMs are characterized by zero cohesive traction with no separation displacement [97,98]. Bi-linear T-S-Ls with linear and exponential softening and trapezoidal CZMs are widely used intrinsic CZMs, as shown in **Fig. 2.8**. Bilinear T-S-L with linear softening is also termed a triangular CZM, which is used in the later part of the

present work. On the other hand, the extrinsic CZMs exhibit finite and non-zero traction even at zero separation. Extrinsic CZMs employ cohesive elements that are incrementally inserted during the computational simulations [99], whereas, in intrinsic CZMs, the cohesive elements are anticipated along the failure path before the simulations. Examples of extrinsic CZMs include constant traction, linear softening, and parabolic softening, as depicted in **Fig. 2.9**.

In fracture mechanics, stress singularity pertains to exceptionally high stress levels at the tip of a crack. In the LEFM, the prevailing type of stress singularity is the inverse square-root singularity. In contrast, non-linear fracture mechanics analysis, such as the EPFM, exhibits the Hutchinson-Rice-Rosengren (HRR) stress singularity. Stress singularity plays a crucial role in evaluating the stress and deformation in the vicinity of the crack tip, which is critical for assessing the behaviour of crack initiation and propagation in materials.

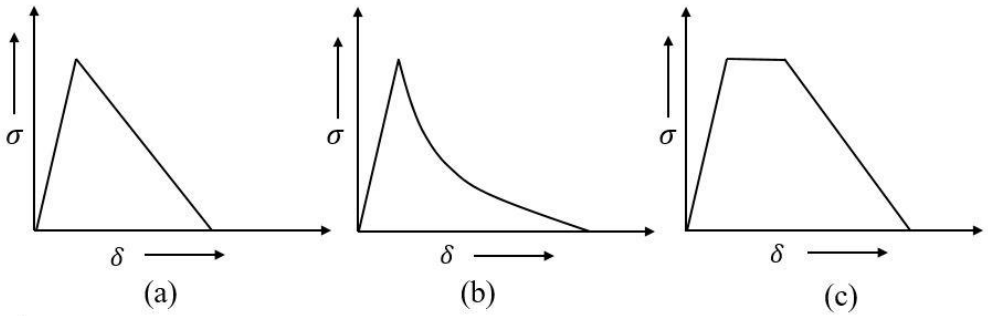

Fig. 2.8 Intrinsic CZMs: Bilinear CZM with (a) Linear, (b) Exponential softening, and (c) trapezoidal CZMs

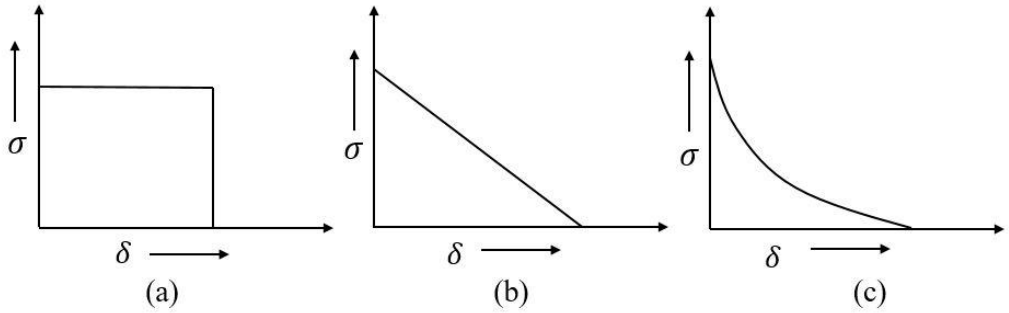

Fig. 2.9 Extrinsic CZMs: (a) Constant traction, (b) Linear, and (c) Exponential softening

Although the CZM was initially developed to eliminate the crack tip stress singularity, most researchers did not follow the stress singularity nullification criteria. Jin and Sun [60] initially used linear hardening cohesive law with a linear elastic material model to investigate some crucial aspects of the CZM. Using an integral equation approach, they observed that stress singularity can only be eliminated for a cohesive law with non-zero traction at zero separation

displacement. Moreover, they derived a CZM for necking in thin ductile cracked sheets, based on which the cohesive energy density, cohesive traction, and shape of the cohesive law were discussed. In another work [100], the same authors extended their study to investigate some conceptual issues for investigating the interface fracture in elastic bi-material. The SIF generated due to the far-field loading and cohesive zone length for semi-infinite dis-similar elastic media was initially estimated, which helps to estimate the size of the CZM for removing crack tip stress singularity. Their observations showed that a single value of cohesive zone length cannot nullify the crack tip stress singularity under combined tension and shear loading conditions. In the end, the energy dissipated at the tip of the cohesive zone was estimated using a bilinear CZM with uncoupled normal and shear traction.

Estimating the strength of stress singularity in a cohesive zone can be facilitated by analyzing the stress and displacement field. Xiao and Karihaloo [101] used the complex potential functions of Kolosov and Muskhelishvili [102] to derive an asymptotic stress and displacement field, focusing specifically on normal cohesive separation. They also explored a particular case of pure mode-I with consideration for Coulomb friction along the crack face. This solution is similar to William's [6] expression, which applies to various types of cohesive laws, such as rectangular, triangular, and exponential, expressed in polynomial forms. However, the coefficients of the solution depend on the cohesive law types and boundary conditions. The obtained asymptotic field is employed as an enrichment function at the tip of a long cohesive crack and short branches/kinks to investigate crack propagation with the help of XFEM analysis. In a separate study, the same authors expressed the asymptotic fields in a separable form, even for a polynomial cohesive law with integer powers [103].

2.9 Determination of the CZM parameters

While the CZM provides a valuable tool for predicting the behaviour of non-linear fractures, its effective use requires meticulous calibration through experimental data and subsequent validation to ensure accurate simulation of the fracture process [104]. Several data reduction techniques, such as property determination, direct, and inverse methods, are available to estimate the cohesive zone parameters — cohesive stiffness, strength, and fracture energy. These methods vary in complexity and offer different levels of accuracy in their results. Some of these approaches have been validated using established fracture characterization

experiments, such as the DCB and the ENF tests for mode I and mode II loadings and the MMB test for mixed-mode (I/II) loadings [28,105].

2.9.1 Property determination method

The approach for determining property involves estimating the cohesive law parameters through appropriate testing [106,107]. However, the CZM parameters acquired from the comprehensive tests are not entirely reliable because of the variations in properties between the bulk material and the thin adhesive bond. This discrepancy is primarily caused by the mixed-mode crack propagation within the adhesive and the strain-constraining effect of the adherends [28,105].

Campilho et al. [108] utilized a cohesive damage model to assess the tensile strength of the CFRP single strap repairs, considering variations in patch thickness and overall length. They employed a trapezoidal cohesive law within a continuum approach to simulate the ductile behaviour of Araldite 420 adhesive. They have evaluated the normal and the shear cohesive strength based on the stress-strain characteristics of the bulk adhesive. The normal cohesive strength aligned with the tensile strength measured in bulk tests, while the shear strength was derived from the normal strength using the von Mises yield criteria. In a separate study, Carlberger and Stigh [109] developed an FE model to simulate the fracture occurring in adhesively bonded joints. The mode I and mode II fracture energies of the bonded joints were estimated by conducting mode I and mode II fracture tests, respectively.

Ibrahim et al. [110] used two distinct test setups, namely the DCB and bonded-shear specimens, to assess the fracture properties in mode I and II of structural epoxy adhesives. After conducting the mode I and mode II fracture characterization tests, they derived the CZM properties for the SLJ and cross-tension (CT) FE models. The FE models for SLJ and CT accurately predicted the peak load, with an average deviation ranging from 2% to 19%. These models demonstrated the ability to anticipate the joint response across various adherend thicknesses, specimen geometries, and modes of loading.

2.9.2 Direct method

The direct approach allows for easy determination of the exact shape of the T-S-L by analyzing the variations of fracture energy with the deformation of the cohesive under fracture characterization tests. Some studies have focused on directly calculating the CZM parameters

for adhesively bonded joints and composite laminates [105,111]. Andersson and Stigh [112] employed a direct method to estimate the CZM parameters for the ductile failure behaviour of Dow Betamate XW1044-3 adhesively bonded joints. They used a series of exponential functions to minimize errors in the measured fracture energy and displacement data obtained from experiments. The resulting cohesive law was trapezoidal and comprised three sections: the initial linear elastic behaviour of the adhesive until it reaches peak stress, a region of constant limiting stress corresponding to plasticity development in the adhesive, and a parabolic softening region at the curve's end.

Högberg and Stigh [113] proposed a direct integration scheme to derive the cohesive law for adhesively bonded joints under mixed-mode loading conditions. For a mixed-mode DCB specimen, the normal and shear cohesive laws are obtained by differentiating the mode I and mode II *J*-integral values with respect to normal and shear separation, respectively. The results indicated a significant disparity between the normal and the shear cohesive laws. Furthermore, the mixed-mode constitutive behaviour of the adhesive can be accurately captured by utilizing ten evenly distributed sets of mixed-mode ratios for any load and geometry conditions. In the CZM analysis, Ji et al. [114] conducted the DCB test methods to address the influence of adhesive thickness on the cohesive strength and fracture energy of adhesive joints bonded with brittle adhesive Loctite Hysol 9460. The measurement of fracture energy by the *J*-integral approach is based on the same methodology proposed by Andersson and Stigh [112].

2.9.3 Inverse method

The inverse method involves an iterative fitting procedure that compares experimental data with numerical results, aiming to precisely describe the cohesive law and the typical behaviour of the simulated material [55]. Campilho et al. [115] employed an iterative approach to determine the CZM parameters for assessing the tensile residual strength of repaired CFRP specimens with varying geometries. The critical fracture energy values necessary for the numerical model were directly obtained from the R-curve generated during fracture characterization tests. To fully define the cohesive parameters, the strength was determined through a trial and error approach. The CZM parameters were fine-tuned with the FE analysis until accurate predictions of the experimental results were achieved.

Campilho et al. [116] conducted experimental and numerical studies to investigate the tensile behaviour of three-dimensional carbon-epoxy adhesively bonded strap repair in their work. The elastic stiffness, strength, and failure modes were evaluated experimentally for different overlap lengths and patch thicknesses. The adhesive layer is simulated in ABAQUS® with a mixed-mode trapezoidal cohesive law for the ductile failure behaviour of the adhesive. All the CZM parameters were determined by inverse methods using a fitting procedure of the experimental results with the numerical load-displacement response. Lee et al. [117] introduced a systematic approach for determining the parameters of the CZM applied to adhesive-bonded joints experiencing mixed-mode loading. They conducted tests using co-cured single-leg bending (SLB) specimens and employed linear extrapolation techniques to calculate fracture toughness in each mode of loading. The damage variables, cohesive strength, and stiffness were identified, and their specific sampling points were established. These sampling points and the defined errors were utilized as input for a kriging metamodel. Subsequently, a non-linear optimization algorithm was employed within the kriging metamodel to assess the CZM parameters when subjected to mixed-mode loading conditions.

2.10 Research gap and the objectives of the present work

The CZM is a widely utilized computational method for simulating the failure of material interfaces. Although the primary purpose of the CZM is to eliminate stress singularity at crack tips, this was not commonly observed in most published literature that employed the CZM to simulate material failure. Another significant finding from the literature is that only extrinsic CZM can remove the stress singularity at the crack tip. Therefore, the first part of the present thesis targets incorporating both intrinsic and extrinsic CZMs to investigate the failure behaviour of adhesively bonded joints under mode I and mode II loading conditions. The study aims to accomplish the following objectives.

- To investigate the influence of the CZM parameters on the crack tip stress singularity for any extrinsic generalized T-S-Ls.
- To perform interface crack growth studies under pure mode I loading conditions.
- To evaluate the extrinsic CZM parameters for predicting the experimental load-displacement response.

- To perform mode II crack growth studies of MWCNTs reinforced adhesively bonded joints. Additionally, it aims to estimate the extrinsic and the intrinsic CZM parameters while predicting the load-displacement response of MWCNTs reinforced adhesively bonded joints under mode II loading.

Although many works have been published on estimating the CZM parameters, they involve customized experimental setups or repetitive trial-and-error processes. Therefore, the thesis aims to evaluate the CZM parameters for composite laminate using straightforward fracture characterization tests. The purpose of the study is to achieve the following objectives.

- To determine the CZM parameters — cohesive strength and fracture energy for the pristine and MWCNTs reinforced CFRP under pure mode I and mode II loading conditions.
- To validate the load-displacement response numerically with the experimentally obtained CZM parameters.
- To conduct an MMB test to examine the failure behaviour of CFRP reinforced with MWCNTs under various mixed-mode ratios.
- To validate the MMB load-displacement response with the obtained mode I and mode II CZM parameters employing proper damage initiation and damage evolution criteria.

Chapter 3 Theoretical Formulation

This chapter outlines the theoretical formulations for determining the cohesive zone parameter that eliminates the crack tip stress singularity. The existing literature showed that a T-S-L with non-zero traction at the onset of the separation could only remove the stress singularity [118]; such CZMs are categorized as extrinsic CZMs, which is primarily focused in the present chapter. Initially, the stress and displacement fields are presented for pure mode I and mode II in the presence of CZM for quasi-brittle materials. These stress and displacement profiles are compared with the numerical field expression to estimate the SIF generated within the cohesive zone. Furthermore, the changes in the overall SIF are displayed in relation to the length of the cohesive zone, showcasing this behaviour for three distinct cohesive laws: constant traction, linear, and parabolic softening.

3.1 Crack tip stress and displacement field in the presence of the CZM

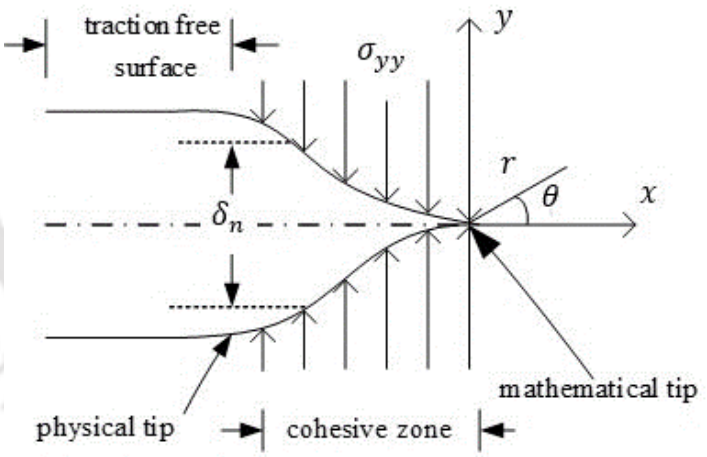

Fig. 3.1 Asymptotic near tip field in the presence of cohesive zone

The stress and displacement field in the presence of the cohesive zone can be obtained from Muskhelishvili's [102] formulation of planar elasticity. Here, the stress and displacement field can be expressed in two complex analytical functions: $\phi(z)$ and $\chi(z)$. According to Muskhelishvili [102], the convenient representation of stress and displacement in Cartesian coordinates is

$$\begin{aligned}\sigma_{xx}+\sigma_{yy}&=2[\phi'(z)+\overline{\phi'(z)}]\\ \sigma_{yy}-\sigma_{xx}+2i\sigma_{xy}&=2[\bar{z}\phi''(z)+\chi''(z)]\\ 2\mu(u+iv)&=\kappa\phi(z)-z\overline{\phi'(z)}-\overline{\chi'(z)}\end{aligned} \tag{3.1}$$

where k and μ are the Kolosov constant and the shear modulus, respectively. For elasticity problems, $k=3-4\nu$ for plane strain or $k=(3-\nu)/(1+\nu)$ for plane stress conditions. The shear modulus $\mu=E/2(1+\nu)$; E and ν are Young's modulus and Poisson's ratio, respectively. z is a complex variable in polar coordinate with $z=re^{i\theta}$, as shown in **Fig. 3.1**. The prime and overbar are used for the differentiation and the complex conjugate. Sih and Liebowitz [119] expressed the analytical functions $\varphi(z)$ and $\chi(z)$ as a series of complex Goursat functions

$$\begin{aligned}\phi(z)&=\sum_{n=0}A_{nn}z^{\lambda_n}=\sum_{n=0}A_{nn}r^{\lambda_n}e^{i\lambda_n\theta}\\ \chi(z)&=\sum_{n=0}B_{nn}z^{\lambda_n+1}=\sum_{n=0}B_{nn}r^{\lambda_n+1}e^{i(\lambda_n+1)\theta}\end{aligned} \tag{3.2}$$

where $A_{nn}=a_{1n}+ia_{2n}$ and $B_{nn}=b_{1n}+ib_{2n}$ are the coefficients of complex eigenvalue expansion. As the crack propagation occurs, the cohesive zone opens up, and the fracture process zone (FPZ) is developed ahead of the crack tip. The end coordinate of FPZ is defined mainly by a physical tip where cohesive traction approaches zero and a mathematical tip with zero crack opening and maximum traction, as shown in **Fig. 3.1**. The complete series expansion of stress and displacement near the crack tip can be obtained by substituting Eq. (3.2) into Eq. (3.1) as follows

$$\begin{aligned}2\mu u=\sum_{n=0}r^{\lambda_n}\{&k(a_{1n}\cos\lambda_n\theta-a_{2n}\sin\lambda_n\theta)\\ &+\lambda_n[-a_{1n}\cos(\lambda_n-2)\,\theta+a_{2n}\sin(\lambda_n-2)\,\theta]+(\lambda_n\\ &+1)(-b_{1n}\cos\lambda_n\theta+b_{2n}\sin\lambda_n\theta)\}\end{aligned} \tag{3.3}$$

$$\begin{aligned}2\mu v=\sum_{n=0}r^{\lambda_n}\{&k(a_{1n}\sin\lambda_n\theta+a_{2n}\cos\lambda_n\theta)\\ &+\lambda_n[a_{1n}\sin(\lambda_n-2)\,\theta+a_{2n}\cos(\lambda_n-2)\,\theta]+(\lambda_n\\ &+1)(b_{1n}\sin\lambda_n\theta+b_{2n}\cos\lambda_n\theta)\}\end{aligned} \tag{3.4}$$

$$\sigma_{xx} = \sum_{n=0} r^{\lambda_n - 1} \{2\lambda_n [a_{1n} \cos(\lambda_n - 1)\,\theta - a_{2n} \sin(\lambda_n - 1)\,\theta] - \lambda_n(\lambda_n - 1)[a_{1n} \cos(\lambda_n - 3)\,\theta] - a_{2n} \sin(\lambda_n - 3)\,\theta] - (\lambda_n + 1)\lambda_n [b_{1n} \cos(\lambda_n - 1)\,\theta - b_{2n} \sin(\lambda_n - 1)\,\theta]\} \quad (3.5)$$

$$\sigma_{yy} = \sum_{n=0} r^{\lambda_n - 1} \{2\lambda_n [a_{1n} \cos(\lambda_n - 1)\,\theta - a_{2n} \sin(\lambda_n - 1)\,\theta] + \lambda_n(\lambda_n - 1)[a_{1n} \cos(\lambda_n - 3)\,\theta] - a_{2n} \sin(\lambda_n - 3)\,\theta] + (\lambda_n + 1)\lambda_n [b_{1n} \cos(\lambda_n - 1)\,\theta - b_{2n} \sin(\lambda_n - 1)\,\theta]\} \quad (3.6)$$

$$\sigma_{xy} = \sum_{n=0} r^{\lambda_n - 1} \{\lambda_n(\lambda_n - 1)[a_{1n} \sin(\lambda_n - 3)\,\theta + a_{2n} \cos(\lambda_n - 3)\,\theta] + (\lambda_n + 1)\lambda_n [b_{1n} \sin(\lambda_n - 1)\,\theta + b_{2n} \cos(\lambda_n - 1)\,\theta]\} \quad (3.7)$$

The generalized opening displacement behind the cohesive zone tip can be given as

$$\delta_n = v|_{\theta=\pi} - v|_{\theta=-\pi} = \sum_{n=0} \frac{r^{\lambda_n}}{\mu} [(k + \lambda_n)a_{1n} + (\lambda_n + 1)b_{1n}] \sin \lambda_n \pi \quad (3.8)$$

Similarly, the sliding displacement of the crack faces

$$\delta_s = u|_{\theta=\pi} - u|_{\theta=-\pi} = \sum_{n=0} \frac{r^{\lambda_n}}{\mu} [(\lambda_n - k)a_{2n} + (\lambda_n + 1)b_{2n}] \sin \lambda_n \pi \quad (3.9)$$

The above stress and displacement solutions must satisfy the boundary conditions along the cohesive crack faces and proper symmetric conditions along the extension line of the cohesive crack.

If the cohesive crack faces are subjected to pure mode I condition, we have

$$\sigma_{yy}\big|_{\theta=\pi} = \sigma_{yy}\big|_{\theta=-\pi} \neq 0, \sigma_{xy}\big|_{\theta=\pi} = \sigma_{xy}\big|_{\theta=-\pi} = 0, \sigma_{xy}\big|_{\theta=0} = 0, v|_{\theta=0} = 0 \quad (3.10)$$

After substituting the boundary condition $\sigma_{xy}\big|_{\theta=0} = 0, v|_{\theta=0} = 0$ in the above stress and displacement field expression from Eq. (3.3)-Eq. (3.7), we can obtain

$$\begin{gathered} (\lambda_n - 1)a_{2n} + (\lambda_n + 1)b_{2n} = 0 \\ (\kappa + \lambda_n)a_{2n} + (\lambda_n + 1)b_{2n} = 0 \\ a_{2n} = b_{2n} = 0 \end{gathered} \quad (3.11)$$

Additionally, the boundary condition $\sigma_{yy}\big|_{\theta=\pi} = \sigma_{yy}\big|_{\theta=-\pi} \neq 0, \sigma_{xy}\big|_{\theta=\pi} = \sigma_{xy}\big|_{\theta=-\pi} = 0$ is satisfied only if $[(\lambda_n - 1)a_{1n} + (\lambda_n + 1)b_{1n}]\sin(\lambda_n - 1)\,\pi = 0$, which gives

$$\begin{cases} \lambda_n = n+1, n = 0,1,2,\ldots. \text{or} \\ b_{1n} = -\dfrac{\lambda_n - 1}{\lambda_n + 1} a_{1n} \end{cases} \tag{3.12}$$

The above equation provides the asymptotic solutions of a pure mode I cohesive crack. The expression for opening displacement (δ_n) in the presence of a cohesive zone can be obtained by substituting Eq. (3.12) into the displacement field Eq. (3.8), which gives

$$\begin{aligned} \delta_n &= \sum_{n=0} \frac{r^{\frac{2n+3}{2}}}{\mu} a_{1n}(\kappa+1)\sin\frac{2n+3}{2}\pi \\ \widehat{\delta_n} &= \sum_{n=0} \bar{c}_n r^{(2n+3)/2}, \bar{c}_n = \frac{(\kappa+1)}{\mu\delta_n^f} a_{1n}\sin\frac{2n+3}{2}\pi \end{aligned} \tag{3.13}$$

The above formulation is already presented in the work of Xiao and Karihaloo [120].

Assuming an ideal mode II cohesive crack conditions (frictionless crack surfaces), the boundary conditions along the cohesive crack faces can be given as

$$\begin{aligned} \sigma_{xy}\big|_{\theta=\pi} = \sigma_{xy}\big|_{\theta=-\pi} \neq 0;\ \sigma_{yy}\big|_{\theta=\pi} = \sigma_{yy}\big|_{\theta=-\pi} = 0 \\ \sigma_{yy}\big|_{\theta=\pi} = \sigma_{xx}|_{\theta=0} = 0 \ \text{ and } u|_{\theta=0} = 0 \end{aligned} \tag{3.14}$$

Following the identical solution procedure as mentioned for mode I cohesive crack, the expression for sliding displacement (δ_s) under pure mode II loading is obtained by substituting Eq. (3.14) into the stress and displacement expression mentioned in Eq. (3.3)-Eq. (3.7), which finally gives

$$\begin{aligned} \delta_s &= \sum_{n=0} \frac{r^{\frac{2n+3}{2}}}{\mu} b_{2n}(\kappa+1)\sin\frac{2n+3}{2}\pi \\ \widehat{\delta_s} &= \sum_{n=0} \bar{d}_n r^{(2n+3)/2}, \bar{d}_n = \frac{(\kappa+1)}{\mu\delta_s^f} b_{2n}\sin\frac{2n+3}{2}\pi \end{aligned} \tag{3.15}$$

3.2 Crack tip stress singularity and the cohesive zone

Assume a plate containing a central crack with a length of $2a$, at the interface of an elastic medium depicted in **Fig. 3.2**. The plate experiences far-field loading, characterized by tensile stress σ_n^{∞} and shear stress σ_s^{∞}. Due to this external loading, a cohesive zone is developed ahead of the crack tip, spanning a distance of $\rho = b - a$. Assuming ρ is much smaller than a, we can write $a = a + \rho$. The SIF generated under the application of applied load can be expressed as

$$K_{applied} = (\sigma_n^{\infty} + i\sigma_s^{\infty})\sqrt{\pi a} \tag{3.16}$$

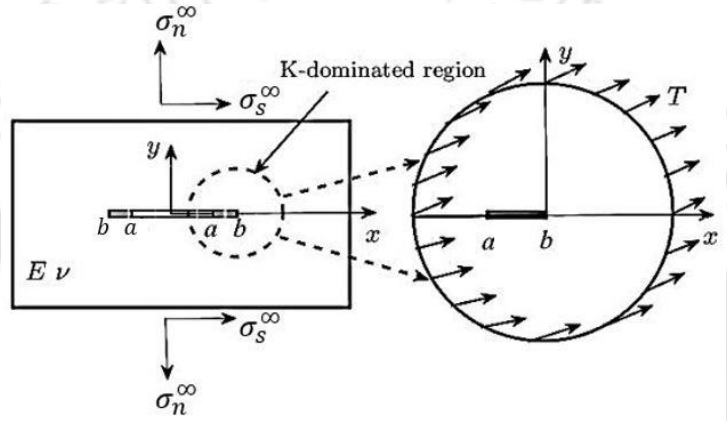

Fig. 3.2 Infinite central crack plate with the K-dominated region used for the analysis

Using the Green's function approach, the SIF generated at the tip of the cohesive zone due to the cohesive traction can be given as [121]

$$K_{cohesive} = -\sqrt{\frac{2}{\pi}}\int_0^{\rho}[\sigma_n(\eta) + i\sigma_s(\eta)]\eta^{-\frac{1}{2}}\mathrm{d}\eta \tag{3.17}$$

where $\sigma_n(\eta)$ and $\sigma_s(\eta)$ are the normal and shear cohesive traction at any arbitrary location η along the crack axis.

For the removal of stress singularity, we can use

$$K_{applied} + K_{cohesive} = 0 \tag{3.18}$$

which gives,

$$(\sigma_n^{\infty} + i\sigma_s^{\infty})\sqrt{\pi a} = \sqrt{\frac{2}{\pi}}\int_0^{\rho}[\sigma_n(\eta) + i\sigma_s(\eta)]\eta^{-\frac{1}{2}}\mathrm{d}\eta \tag{3.19}$$

For a cohesive zone with constant normal and shear traction $\sigma_n(\eta) = \sigma_n^c$ and $\sigma_s(\eta) = \sigma_s^c$, Eq. (3.19) leads to

$$(\sigma_n^\infty + i\sigma_s^\infty)\sqrt{\pi a} = \sqrt{\frac{2}{\pi}}(\sigma_n^c + i\sigma_s^c)\int_0^\rho \eta^{-\frac{1}{2}}d\eta$$
$$(\sigma_n^\infty + i\sigma_s^\infty)\sqrt{\pi a} = \sqrt{\frac{2}{\pi}}(\sigma_n^c + i\sigma_s^c)2\sqrt{\rho} \quad (3.20)$$

Assuming a pure mode I or mode II case, separating the real and imaginary parts of Eq. (3.20), we get

$$\sigma_n^\infty\sqrt{\pi a} = \sqrt{\frac{2}{\pi}}\sigma_n^c 2\sqrt{\rho}$$
$$\sigma_s^\infty\sqrt{\pi a} = \sqrt{\frac{2}{\pi}}\sigma_s^c 2\sqrt{\rho} \quad (3.21)$$

Therefore, for a given constant normal cohesive traction σ_n^c and shear cohesive traction σ_s^c with prescribed loading σ_n^∞ and σ_s^∞, the cohesive zone length ρ can be evaluated from Eq. (3.21).

However, for any generalized T-S-Ls, the cohesive stress distribution $\sigma_n(\eta)$ or $\sigma_s(\eta)$ mentioned in Eq. (3.19) along the cohesive zone is not readily available to determine the cohesive zone parameters for the removal of stress singularity. A combined semi-analytical method, incorporating FE analysis alongside theoretical formulations, is employed to compute the SIF. Subsequently, a domain-independent interaction integral approach is used to numerically evaluate the SIF in the presence of a cohesive zone. The change in SIF is presented for eight distinct cohesive zone lengths. This dataset enables the determination of the value of ρ at which the SIF approaches zero.

3.2.1 Interface cohesive law

It is already mentioned that in order to mitigate the crack tip stress singularity, a cohesive zone needs to exhibit non-zero traction when at zero separation displacement. To fulfill these criteria, a generalized extrinsic CZM is employed to describe the behaviour of the interface. The constitutive behaviour of the cohesive model can be given as

$$\sigma_i(\delta_i) = \begin{cases} \sigma_i^c \left(1 - \dfrac{\delta_i}{\delta_i^f}\right)^N, & \delta_i < \delta_i^f \\ 0, & \delta_i \geq \delta_i^f \end{cases} \tag{3.22}$$

where σ_i^c is the peak cohesive traction with $i = n$ or s under mode I and mode II loading, respectively. For the proposed extrinsic CZM, the cohesive tractions are initially σ_n^c (or σ_s^c); the cohesive traction decreases gradually and approaches zero value once the instantaneous cohesive separation δ_n (or δ_s) approaches the critical cohesive separation δ_n^f (or δ_s^f) under their respective modes of loadings. The exponent N is used to define the shape of the cohesive law.

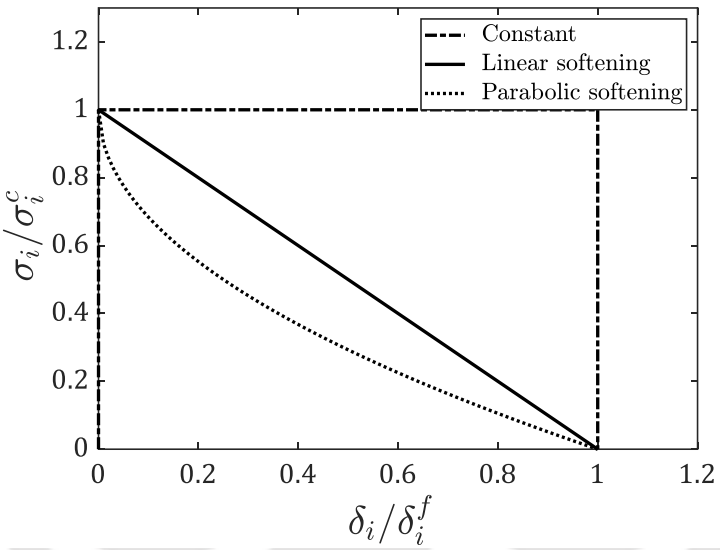

Fig. 3.3 A generalized extrinsic CZM

Three distinct values of N =0, 0.5, and 1 are considered, corresponding to constant traction, parabolic, and linear softening law, respectively. The variation of the T-S-Ls for different values of *N* are shown in **Fig. 3.3**.

3.3 Numerical methodology

This section outlines the numerical procedures for determining the characteristic cohesive zone length ρ within the singularity-dominated region (SDZ), as illustrated in **Fig. 3.2**, nullifying the crack tip stress singularity. The results are then compared with analytical and semi-analytical results for constant traction and linear softening laws. This approach can readily be expanded to encompass higher-order laws, as detailed in Eq. (3.22).

3.3.1 Model geometry and the boundary conditions

As the region adjacent to the crack is primarily K-dominated, a finite circular area centered at the mathematical crack tips, as depicted in **Fig. 3.2**, is selected for the numerical analysis. The traction field developed at the outer edge of the K-dominant region can be given as

$$\begin{bmatrix} T_x \\ T_y \end{bmatrix} = \begin{bmatrix} \sigma_{xx} & \sigma_{xy} \\ \sigma_{xy} & \sigma_{yy} \end{bmatrix} \begin{bmatrix} n_x \\ n_y \end{bmatrix} \tag{3.23}$$

where n_x and n_y are the direction cosines of the unit normal vector to the boundary with $n_x = \cos\theta$ and $n_y = \sin\theta$, respectively. σ_{xx}, σ_{yy}, and σ_{xy} are the near-tip stress field, where

$$\begin{aligned} \sigma_{xx} &= \frac{K_I}{\sqrt{2\pi r}} \cos\left(\frac{\theta}{2}\right)\left[1 - \sin\left(\frac{\theta}{2}\right)\sin\left(\frac{3\theta}{2}\right)\right] \\ \sigma_{yy} &= \frac{K_I}{\sqrt{2\pi r}} \cos\left(\frac{\theta}{2}\right)\left[1 + \sin\left(\frac{\theta}{2}\right)\sin\left(\frac{3\theta}{2}\right)\right] \\ \sigma_{xy} &= \frac{K_I}{\sqrt{2\pi r}}\left[\sin\left(\frac{\theta}{2}\right)\cos\left(\frac{\theta}{2}\right)\cos\left(\frac{3\theta}{2}\right)\right] \end{aligned} \tag{3.24}$$

for pure mode I and

$$\begin{aligned} \sigma_{xx} &= -\frac{K_{II}}{\sqrt{2\pi r}} \sin\left(\frac{\theta}{2}\right)\left[2 + \cos\left(\frac{\theta}{2}\right)\cos\left(\frac{3\theta}{2}\right)\right] \\ \sigma_{yy} &= \frac{K_{II}}{\sqrt{2\pi r}}\left[\sin\left(\frac{\theta}{2}\right)\cos\left(\frac{\theta}{2}\right)\cos\left(\frac{3\theta}{2}\right)\right] \\ \sigma_{xy} &= \frac{K_{II}}{\sqrt{2\pi r}} \cos\left(\frac{\theta}{2}\right)\left[1 - \sin\left(\frac{\theta}{2}\right)\sin\left(\frac{3\theta}{2}\right)\right] \end{aligned} \tag{3.25}$$

for pure mode II, respectively.

The singularity-dominated region, as represented in **Fig. 3.2**, is modelled in the FE software ABAQUS® 2017. The behaviour of the cohesive material and the failure criteria are defined using the user subroutine UMAT. The global coordinate system is positioned at the center of the geometry, specifically at the mathematical tip. A magnified view of the finite element mesh near the tip of the cohesive zone is presented in **Fig. 3.4**. The meshed geometry on the parent material is discretized using four-noded quadrilateral elements with two-dimensional cohesive elements (COH2D) along the interface. Two distinct mesh configurations are considered: a square domain encompassing the cohesive zone tip and a circular domain surrounding it. The circular domain has a radius of r =100 mm, with an initial crack length of $a = r - \rho$. The base

material is aluminum with the following properties: Young's modulus (E) = 70 GPa, and Poisson's ratio (ν) = 0.33. The far-field loading is characterized by SIF $K = K_I = K_{II} = 100$ MPa$\sqrt{\text{mm}}$, where K_I and K_{II} are the mode I and mode II SIF, respectively. The thickness of the cohesive layer is maintained at $t = 0.1$ mm. The total number of elements is considered based on the mess convergence analysis.

The assumed material properties for the cohesive are:

$$\sigma_n^c = \sigma_s^c = 50 \text{ MPa}; \; G_n^c = G_s^c = \frac{K^2}{E} = 0.1428 \text{ KJ/m}^2. \tag{3.26}$$

Here, G_n^c and G_s^c are the critical fracture energy in mode I and mode II loading, respectively.

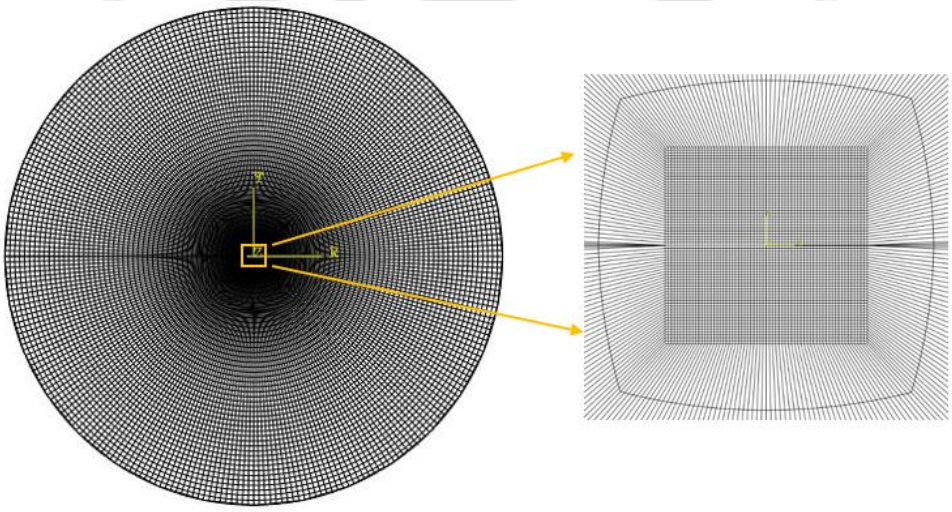

Fig. 3.4 FE mesh geometry of the singularity-dominated region

The in-built contour integral in ABAQUS® lacks crack face traction term; therefore, the SIF obtained depends on the contour. Including crack face traction would have solved the issue, but mode separation would still be an issue for contour integral. Therefore, the domain-dependent interaction integral is used for the present analysis. This formulation assumes a linear elastic response with no body forces, implemented on a square path (composed of 8 elements in the first contour; out of which four 2-D quadrilateral parent elements and another four 2-D cohesive elements) encircling the tip of the cohesive zone, as shown in **Fig. 3.5 (a).** The SIFs obtained by the interaction integral and contour integral for a particular cohesive zone length ρ =1.75 mm and σ_n^c = 50 MPa for a linear softening cohesive law are shown in **Fig. 3.5 (b)**. From **Fig. 3.5 (b),** it is evident that the interaction integral formulation is domain-independent, and it can be extended to any square domain covering the mathematical tip of the cohesive zone.

The detailed interaction integral formulation is already described in the section 2.2.2 of the literature review section.

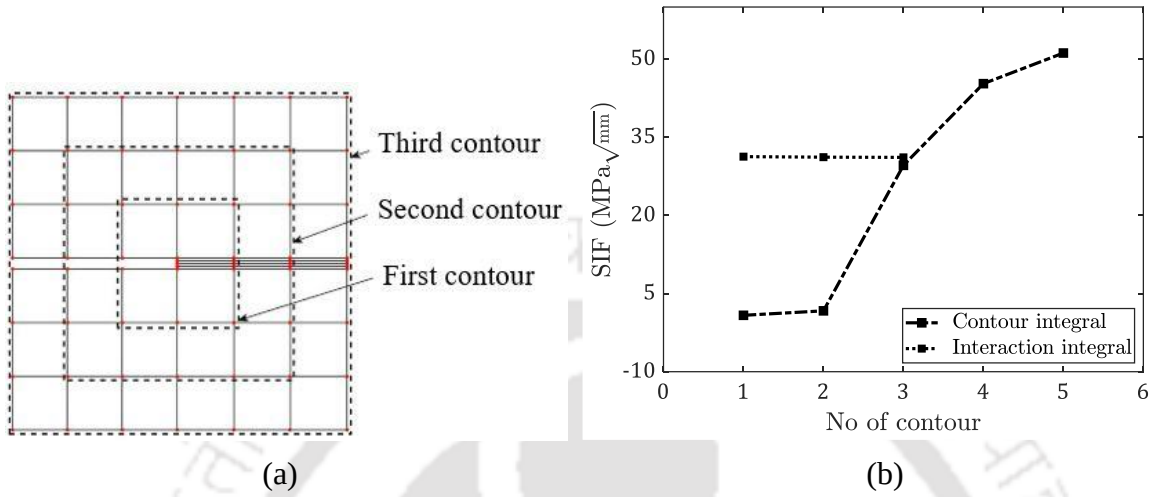

Fig. 3.5 (a) Domain for the interaction integral, (b) Comparison of SIF between contour and interaction integral

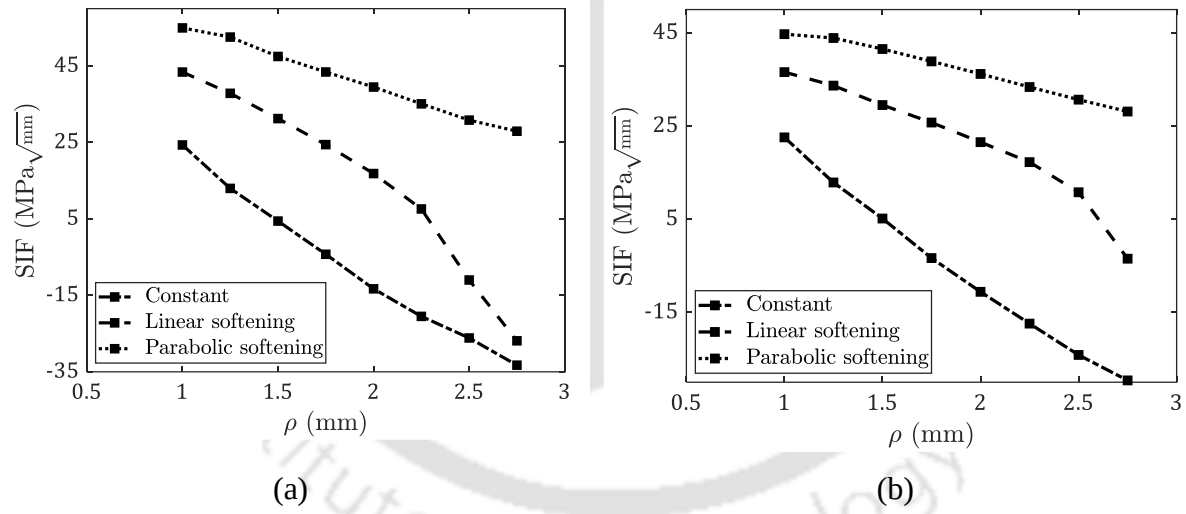

Fig. 3.6 Variation in the SIF with changes in cohesive zone length (a) Mode I, (b) Mode II

The length of the cohesive zone, denoted as ρ, is varied within a range of 1 mm to 2.75 mm, incrementing by 0.25 mm. The cohesive energy and strength remain unchanged, as mentioned in Eq. (3.26) of section 3.3.1 during the entire simulation. The SIF is computed at the tip of the cohesive zone using the interaction integral procedure under pure mode I and mode II loading for all three cohesive laws: constant traction, linear softening, and parabolic softening. **Fig. 3.6 (a)** and **Fig. 3.6 (b)** show that the reduction in SIF is more rapid in constant traction cohesive law compared to linear and parabolic softening. In the case of constant traction cohesive law,

the magnitude of the $K_{cohesive}$ increases rapidly, as evident from Eq. (3.21), resulting in a rapid reduction in the net SIF. So, not only the magnitude but also the variation of cohesive stress along the length of the CZM is the deciding factor that affects the net SIF. Additionally, it is noticed that for linear softening cohesive law, the reduction in SIF is rapid under mode I loading compared to mode II loading conditions. This discrepancy primarily arises from the variations in the deformation behaviour along the length of the cohesive crack. Specifically, the cohesive crack subjected to mode I loading experiences smaller deformation than the mode II loading. This limited deformation results in comparatively higher cohesive stress, consequently leading to an increase in the $K_{cohesive}$ values for larger cohesive zone lengths. These increased $K_{cohesive}$ values subsequently contribute to a rapid reduction in the overall SIF.

3.3.2 Comparison between FEA results with the semi-analytical studies

For a constant cohesive law, the SIF developed from the cohesive zone at the crack tip can be easily evaluated through analytical expression, as outlined in Eq. (3.21), as discussed earlier in Section 3.2. The comparison between the SIF determined via the analytical expression and the interaction integral is shown in **Fig. 3.7**. The numerical results agree well with the analytical results, and the errors are within reasonable limits.

However, for any other generalized T-S-Ls, straightforward analytical expressions for evaluating the SIF are unavailable due to the complexity of the cohesive profile. Hence, a semi-analytical procedure is adopted to approximate the SIF around the tip of the cohesive zone. In this regard, a linear-softening cohesive model is employed.

For other generalized T-S-Ls, the pure mode I and II asymptotic displacement fields mentioned in Eq. (3.13) and Eq. (3.15) approximate the stress field ahead of the cohesive tip. After obtaining the displacement field numerically around the cohesive tip for a specified cohesive law, unknown coefficients are determined by comparing the numerically obtained field with the analytical field mentioned in Eq. (3.13) and Eq. (3.15). Coefficient up to their fifth order is considered to get the desired computational accuracy, as shown in **Fig. 3.8.**

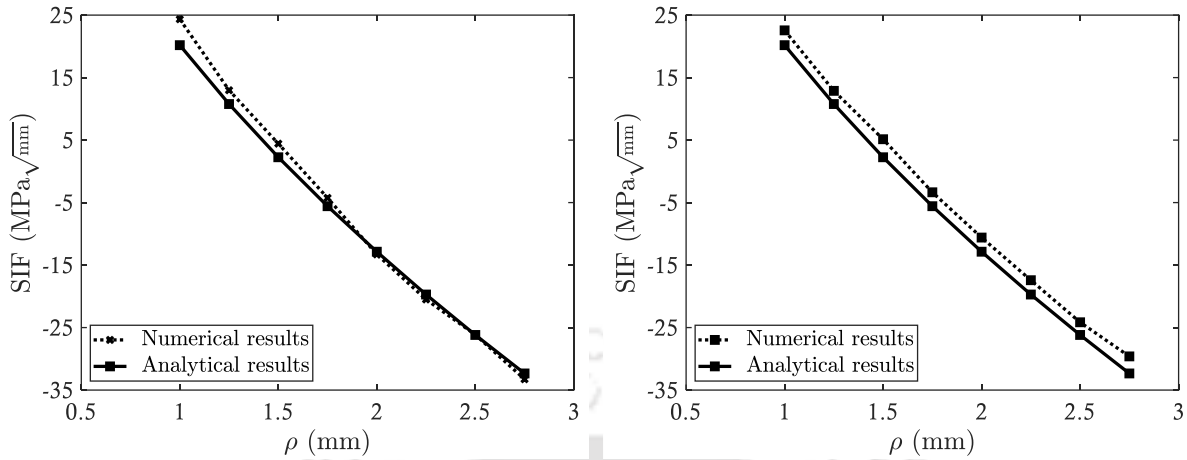

Fig. 3.7 Comparison of SIFs for a constant T-S-L under (a) Mode I, and (b) Mode II loading

Table 3.1 Variation of the coefficients with the cohesive zone length (pure mode I with linear softening T-S-L)

ρ (in mm)	$\bar{c_1}$	$\bar{c_2}$	$\bar{c_3}$	$\bar{c_4}$	$\bar{c_5}$
1	6.042	−26.347	53.080	−48.847	16.785
1.25	4.090	−13.963	22.515	−16.604	4.572
1.5	2.822	−7.760	10.380	−6.360	1.455
1.75	2.097	−4.821	5.571	−2.949	0.581
2	1.514	−2.866	2.865	−1.314	0.225
2.25	1.092	−1.710	1.519	−0.620	0.094
2.5	0.568	−.9475	0.621	−0.295	.0412
2.75	−0.193	0.447	−0.295	0.091	−0.011

For a linear softening cohesive law, the obtained value of the coefficients and their variations, along with the cohesive zone length, is mentioned in **Table 3.1** and **Table 3.2** for pure mode I and mode II, respectively. All the coefficients are monotonically increased or decreased with the change in cohesive zone length ρ. After obtaining the displacement field, the stress field in the cohesive crack for a particular cohesive law can be easily evaluated from Eq. (3.22). **Fig. 3.9** and **Fig. 3.10** compared the pure mode I and mode II displacement and stress behaviour for a linear softening T-S-L, respectively, for a specific value of ρ =1.75 mm. **Fig. 3.11 (a)** and **Fig. 3.11 (b)** represents the SIF obtained for semi-analytical and interaction

integral with the changes in cohesive zone length for a linear-softening cohesive law. The numerical results agree well with the semi-analytical formulation.

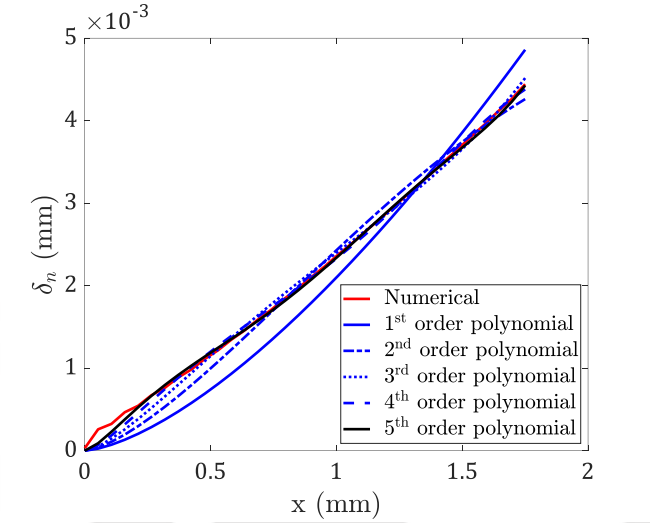

Fig. 3.8 Polynomial order considered to estimate the displacement field (for pure mode I, $\rho = 1.75$ mm)

Table 3.2 Variation of the coefficients with the cohesive zone length (pure mode II with linear softening T-S-L)

ρ (in mm)	$\overline{d_1}$	$\overline{d_2}$	$\overline{d_3}$	$\overline{d_4}$	$\overline{d_5}$
1	5.143	−21.661	43.067	−39.286	13.417
1.25	3.437	−11.277	17.925	−13.081	3.573
1.5	2.342	−6.176	8.177	−4.973	1.131
1.75	1.573	−3.370	3.837	−2.007	0.392
2	0.964	−1.622	1.629	−0.752	0.129
2.25	0.416	−0.382	0.364	−0.156	0.025
2.5	−0.094	0.185	−0.216	0.075	−0.009
2.75	−0.478	0.873	−0.609	0.199	−0.024

3.4 Closure

This chapter proposes a numerical solution procedure with analytical/semi-analytical methodology to determine the size of the cohesive zone (ρ) that nullifies the crack tip stress singularity. The variations in the SIF with the CZM length are presented for three extrinsic CZMs: constant traction, linear, and parabolic softening. It is observed that the variation in the

SIF with the cohesive zone length is highest for constant T-S-L, followed by linear and parabolic softening.

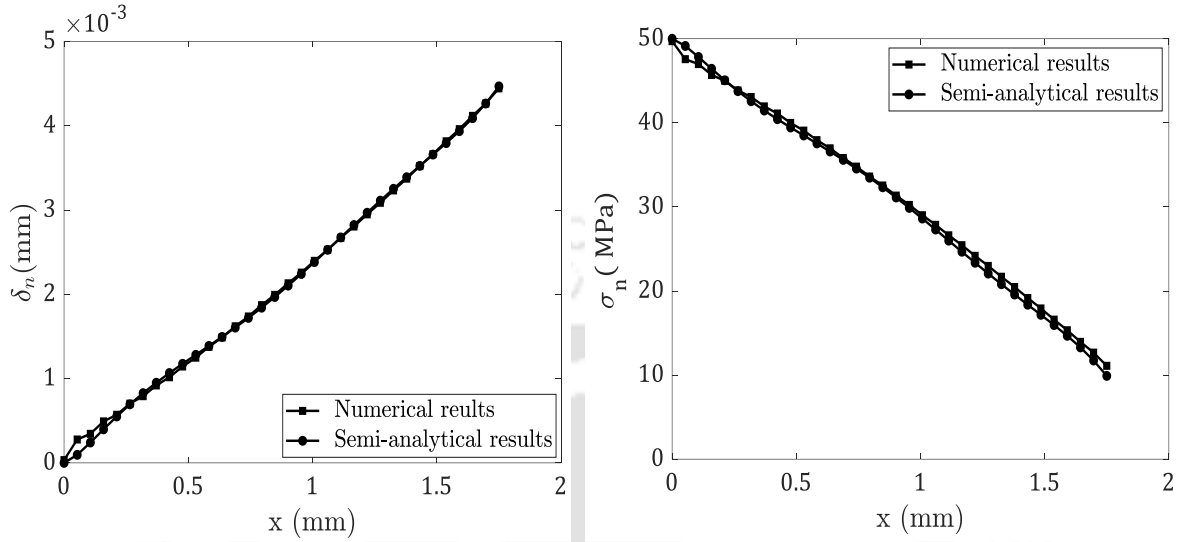

Fig. 3.9 (a) Mode-I displacement, and (b) Stress profile for ρ= 1.75 mm.

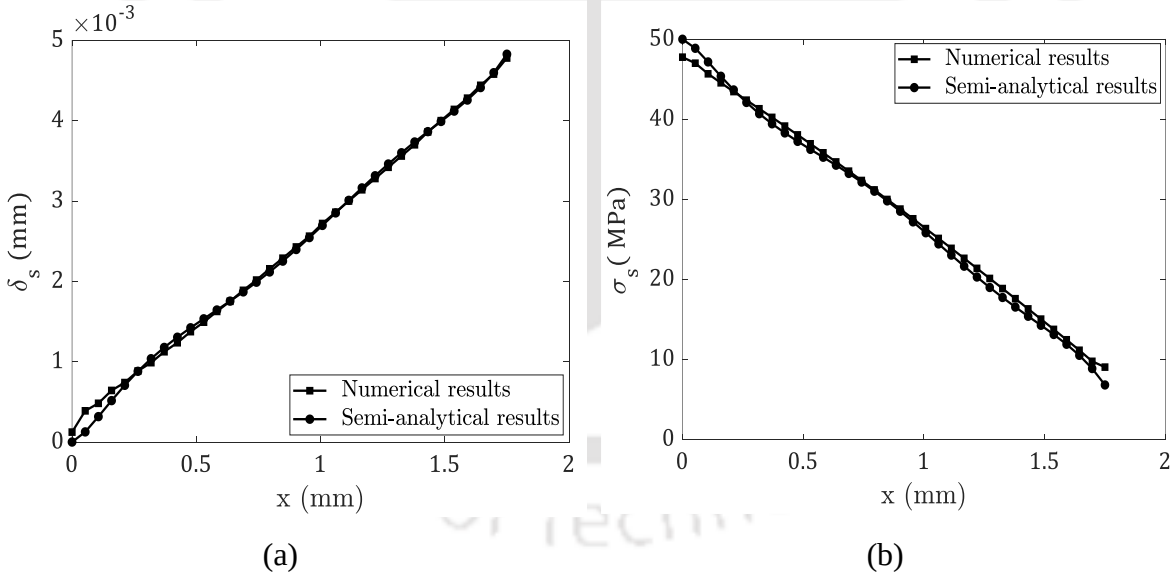

Fig. 3.10 (a) Mode-II displacement, and (b) Stress profile for ρ= 1.75 mm.

One can easily calculate the SIF in the presence of a cohesive zone for constant T-S-L. However, no straightforward procedures are available when dealing with other generalized T-S-Ls. In such cases, a semi-analytical approach is employed to determine the SIF in the presence of the CZM. The numerical results of the interaction integral method align well with those

obtained using the semi-analytical and analytical approaches for linear softening and constant traction. This proposed semi-analytical procedure can be extended to evaluate the strength of stress singularity for other higher-order CZMs.

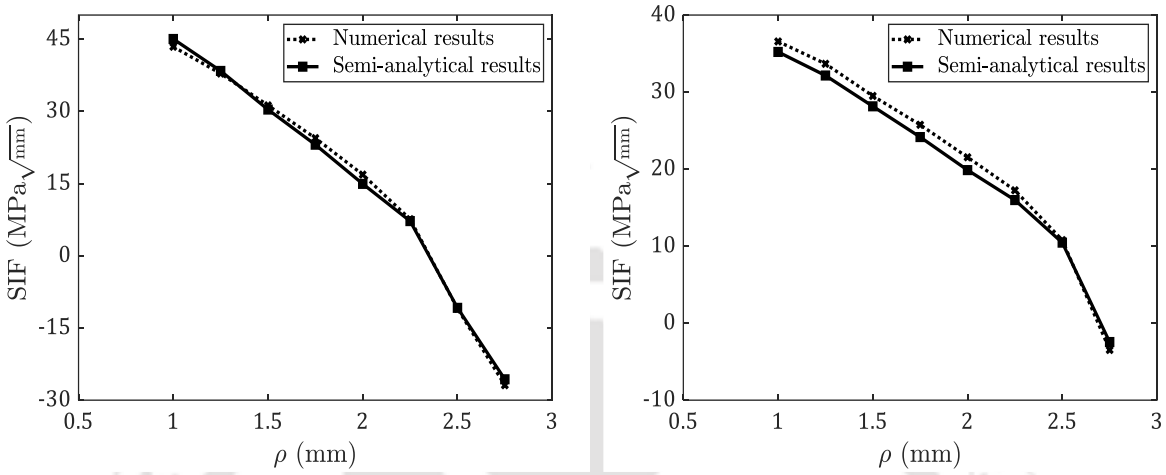

Fig. 3.11 Comparison of SIFs for a linear softening T-S-L under (a) Mode I, and (b) Mode II loading

Chapter 4 Interface Fracture – Experimental methodology

This chapter briefly overviews the adhesively bonded joints, emphasizing their potential advantages and limitations. The initial part of the study explores the fracture behaviour of Polymethyl methacrylate (PMMA) adhesively bonded specimens subjected to pure mode I loading conditions. At the same time, the latter portion investigates the influence of multi-walled carbon nanotubes (MWCNTs) on the mode II interface fracture behaviour in adhesively bonded aluminum joints. Some essential inferences from the experimental study are presented at the end.

4.1 Adhesive joining — a brief insight

Adhesive bonding is a versatile technique used to join similar or dissimilar materials using adhesive materials. The process entails the application of adhesive onto the surface of the substrate, which subsequently cures and establishes a resilient bond. Various types of adhesives, such as epoxies, polyurethane, acrylic resin, and cyanoacrylate, have been utilized in adhesive joining. The choice of adhesive depends on factors like the compatibility between the adhesive and the substrate, the desired bond strength, and the conditions under which the joints will operate [122,123]. As advanced joining technologies continue to evolve, the utilization of adhesive bonding continues to expand.

4.1.1 Different types of joints

Adhesively bonded joints come in various types, each possessing unique characteristics and suitable applications. The joint selection relies on factors such as the specific application, the materials involved, the desired strength, and the load-bearing capacity. Additionally, the thickness of the adhesive is a crucial parameter that influences the joint performance. Experimental studies have indicated that the adhesive thickness should ideally range between 0.1-0.2 mm for optimal joint strength [56].

Lap joints are the simplest adhesive bond configuration commonly used, where overlapping surfaces are joined together using an appropriate adhesive. These are particularly well-suited

for connecting flat surfaces and offer excellent shear strength. Single-lap joints are easy to fabricate and analyze; however, the double-lap joint provides better resistance to peel stress. T-shape joints are widely used in manufacturing aircraft tails, where one component is bonded at a right angle to another, forming a T-shaped configuration. This type of joint provides enhanced resistance against bending and twisting forces.

When joining larger surface areas like panels or sheets, a common choice is the butt joint, which is applied to the ends of the two substrates and bonded together. The scarf joint is widely used in boatbuilding and furniture construction, joining two tapered edges. This type of joint offers increased bonding areas, resulting in stronger bond connections and higher load-bearing capacity [124]. However, it's important to note that a mismatch in stiffness between the adherend and the adhesive can lead to increased stress concentration at the end of the joint. A fillet joint is often used for that purpose, which helps minimize stress singularity and promotes a more even distribution of the load. An overview of some popularly used joints is shown in **Fig. 4.1**.

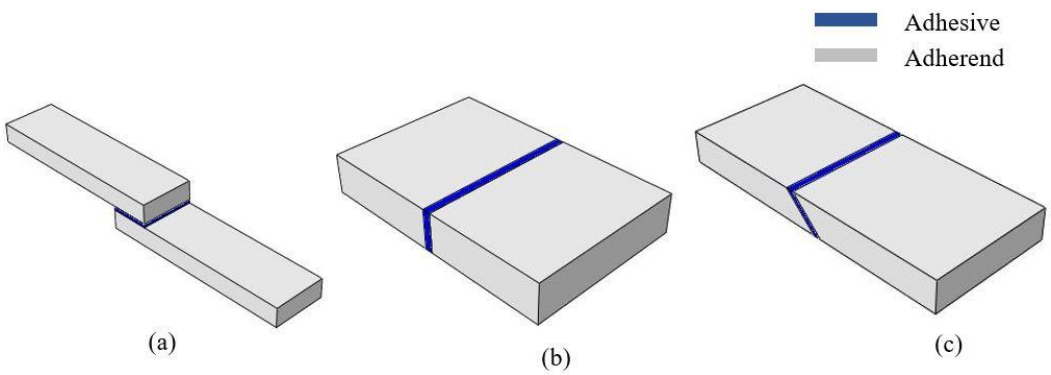

Fig. 4.1 Types of Adhesively bonded joints (a) Lap joint, (b) Butt joint, and (c) Scarf joint

4.1.2 Failure modes within the bonded joints

Failure modes in bonded joints can be classified into cohesive, adhesive, and adherend failure. When the failure occurs within the adhesive itself rather than at the interface between the adherend and adhesive, it is known as cohesive failure. This type of failure happens when the adhesive lacks sufficient strength to withstand the applied force, resulting in internal failure within the adhesive material. Excessive stress concentration within the adhesive, caused by flaws or incorrect bonding techniques, can also contribute to cohesive failure. Selecting

appropriate adhesives and employing proper bonding techniques is crucial to mitigate the risk of cohesive failure.

An adhesive failure occurs when the adhesive and the adherend are separated at their interface. This failure is typically caused by inadequate surface preparation and a lack of compatibility between the adhesive and the substrate. If both cohesive and adhesive failures are present, and the fracture is near the adhesive surface, it can also be classified as an adhesive failure. It is essential to follow proper surface preparation methods, choose an appropriate adhesive for the specific application, and maintain suitable environmental conditions to avoid this type of failure.

Adherend failure, which is less commonly observed, predominantly occurs in bonded joints where the adherend material is composed of composites. The primary reason behind adherend failure can be attributed to inadequate curing of the lamina or flawed ply matrices. Different failure modes of the bonded joint are illustrated in **Fig. 4.2**.

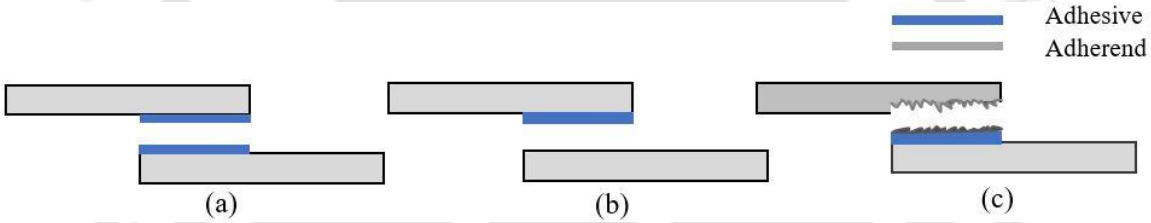

Fig. 4.2 Failure modes in bonded joints (a) Cohesive failure, (b) Adhesive failure, and (c) Adherend failure

4.1.3 Advantages and limitations

Adhesively bonded joints exhibit superior strength and load-bearing capacity, ensuring even stress distribution and reducing stress concentration for enhanced overall joint strength. Compared to conventional mechanical fastening techniques like bolts or rivets, adhesively bonded joints can significantly reduce weight. This advantage is precious in industries such as automotive and aerospace, where lightweight structures are crucial for improving fuel efficiency and optimizing engine performance. Furthermore, adhesively bonded joints offer superior resistance to fatigue, impact, and vibration compared to traditional joining methods. Some adhesives also possess excellent damping properties, contributing to the longevity and durability of the joints. By eliminating the need for drilling holes and mechanical fasteners, adhesively bonded joints eliminate potential entry points for corrosive agents. Moreover, the

design flexibility of bonded joints allows for joining similar and dissimilar materials, expanding the range of available adhesives and enabling innovative designs.

Adhesively bonded joints require specific procedures for surface preparation, which involves roughening and cleaning the substrate. Inadequate surface preparation results in decreased adhesion between the adhesive and the adherend, leading to a decline in joint strength. Moreover, adhesives are susceptible to environmental conditions such as temperature and humidity. Extreme temperature changes and exposure to certain chemicals can degrade the adhesive properties and overall durability, thereby impacting the strength of the joint.

In contrast to bolted and riveted joints that can be effortlessly taken apart, disassembling adhesively bonded joints necessitates specialized tools and techniques, resulting in a time-consuming and expensive process. Adhesive bonding techniques rely on the compatibility of materials, ensuring that they adhere effectively to one another. The proper adhesive selection is essential, considering the material to be joined for the requisite bond strength.

4.2 Crack propagation study in Adhesively bonded Interface

The study investigates the interface fracture behaviour of adhesively bonded joints under mode I and mode II loading conditions. The selection of adhesives and the substrate system are chosen based on their anticipated use in automobile, aerospace, and structural applications. Two different substrates, PMMA and aluminum, are bonded with commercially available epoxy resin for mode I and mode II crack propagation studies, respectively. Furthermore, the study also investigates the influence of MWCNTs on the interface fracture properties of adhesively bonded aluminum joints under mode II loading.

4.3 Experimental procedure: Mode I interface crack propagation

4.3.1 Material

The material chosen for the experimental study is a transparent and non-crystalline thermoplastic polymer known as PMMA, commonly called acrylic or Plexiglas. PMMA is a suitable structural polymer and can be effectively bonded with various commercial adhesives for interface studies. An acrylic sheet with a thickness of 10 mm, available under the brand name BIGMALL (India), is selected for experimental investigations.

4.3.2 Strength and Toughness Measurement

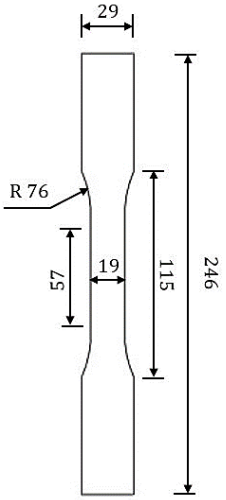

All dimensions are in mm

Fig. 4.3 Tensile test specimen

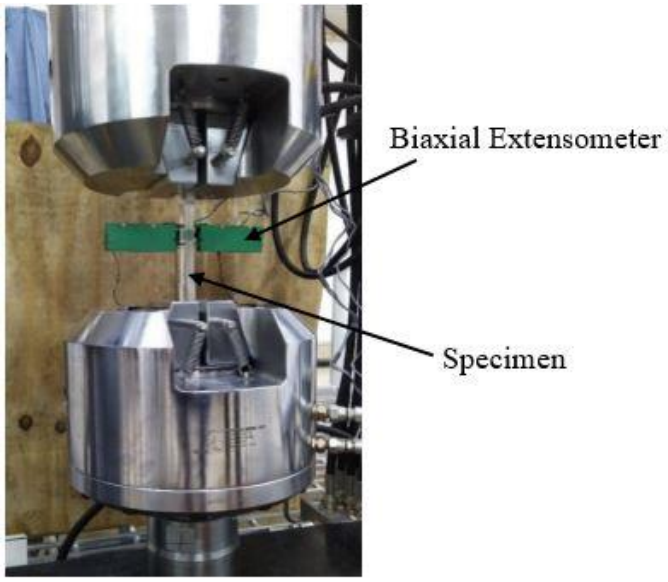

Fig. 4.4 Experimental setup for the tensile test

As there is no standard method for evaluating the interfacial fracture toughness, a procedure identical to Alam et al. [125] for measuring the deflection-penetration behaviour of the PMMA interface is adopted. Before proceeding, accurate material properties (Young's modulus and Poisson's ratio) are essential to perform interface crack propagation simulation. Five specimens are tested according to the ASTM D638-14 [126] test method to evaluate the requisite elastic properties. A schematic diagram of a dog-bone-shaped tensile specimen is shown in **Fig. 4.3**. All the specimens are machined in a CNC (computer numeric control) laser cutting machine to confirm good dimensional accuracy. The tests are conducted in a 250 kN BISS servo-hydraulic Universal Testing Machine with a 1mm/min strain rate, as shown in **Fig. 4.4**. The obtained elastic properties after the experimentation are listed in **Table 4.1**.

Table 4.1 Obtained mechanical properties of the PMMA

Property	value
Young's modulus (GPa)	2.88
Poisson's ratio	0.38

A non-standard fracture test is carried out to evaluate the fracture toughness at the interface. The schematic of a disc-shaped CT specimen with a thickness denoted as t = 10 mm, employed for the experimental process, as shown in **Fig. 4.5**. The adhesive joining involves a low-strength, brittle Araldite resin (Epofine 1564) mixed adequately with hardener (FINEHARD-

3486-2) in the weight ratio of 10:3 to connect the native PMMA with minimal thickness, ensuring the discontinuity in local properties. Thorough cleaning of all interfaces is achieved using fine-grade sandpaper and subsequent acetone treatment to eliminate debris and impurities.

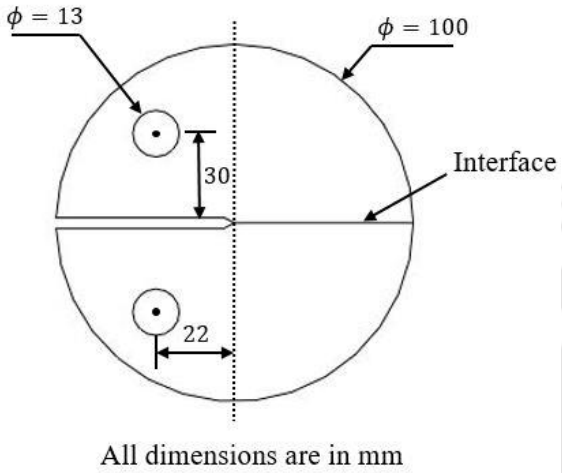

Fig. 4.5 Non-standard disc-shaped CT specimen for fracture test

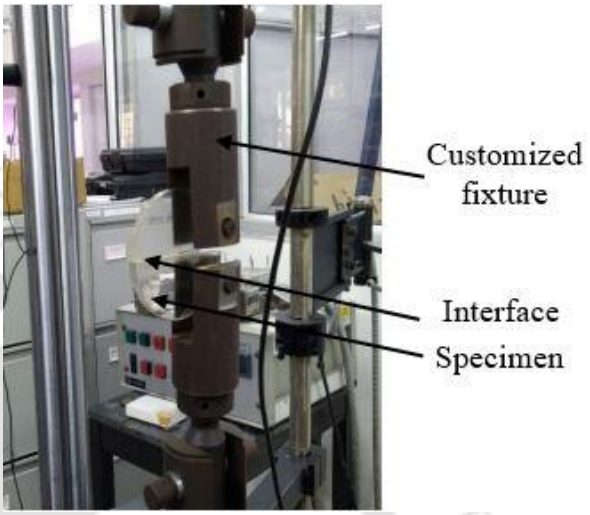

Fig. 4.6 Experimental setup for fracture test

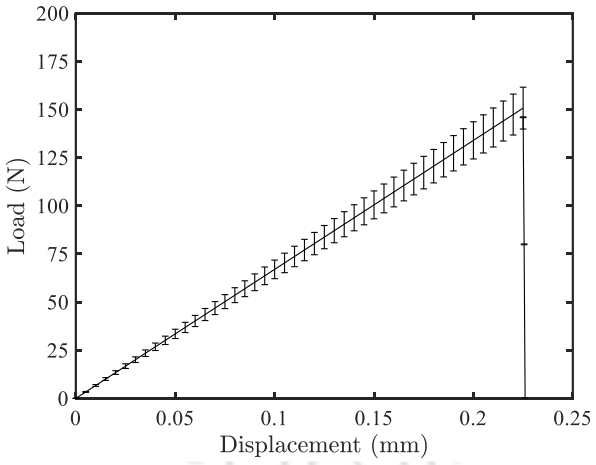

Fig. 4.7 Load displacement behaviour at the interface

Two semicircular PMMA specimens are affixed with the mentioned adhesive, positioned ahead of the notch tip from the center of the midplane. Additionally, two circular openings with a diameter of 13 mm are precision-machined on each specimen to facilitate secure clamping in appropriate fixtures. Employing a 25 kN INSTRON 8801 dynamic testing machine, shown in **Fig. 4.6**, the fracture toughness of the interface is assessed for five identical samples. A quasi-

static test is performed at a displacement rate of 0.1 mm/min to determine the overall load-deflection behaviour of the interface accurately.

The load resistance by the specimen increases linearly with the separation until crack propagation is initiated, and it drastically drops. This sudden drop in the load-displacement response mimics the inherently brittle fracture of the material interface. **Fig. 4.7** illustrates the average load-displacement behaviour of all test specimens, accompanied by their standard deviation.

4.4 Experimental procedure: Mode II interface crack propagation

4.4.1 Material

Aluminum specimens are bonded using adhesives mixed with different proportions of hydroxyl functionalized MWCNTs. Modified compact tension (CT) samples are fabricated, incorporating pristine, 0.1 wt.%, 0.2 wt.%, and 0.3 wt.% of MWCNTs. All the specimens are subjected to an Instron 8801 100 kN dynamic testing system under quasi-static loading conditions. The subsequent sections illustrate the experimental methodology in detail.

The half CT-shaped Aluminium-6061 substrates are joined by the same epoxy adhesives used for pure mode I crack propagation. The aluminum substrate is purchased from Maharashtra Metal, India. The specimens are cut out from an aluminum alloy plate of dimension 500×500×10 mm^3 using a wire-cut electrical discharge machine (EDM). The Young's modulus and the Poisson's ratio of the epoxy-based adhesive are approximately 3.1 GPa and 0.29, respectively, as provided by the manufacturer. The MWCNTs have a diameter of 30 nm, length of 10 μm, and elastic modulus of 400 GPa (approx.) supplied by Adnano Technologies, India. The fixture is made of steel. The material properties of the substrate and the fixture are provided in **Table 4.2**.

Table 4.2 Material properties of specimen and fixture

Material	Young's modulus (E) in GPa	Poisson's ratio (ν)
Aluminum	70	0.33
Steel	210	0.30

4.4.2 Techniques used for the dispersion of MWCNTs within the Epoxy resin

Applying CNTs-reinforced adhesively bonded joint poses significant challenges due to the improper dispersion of nanofillers into the polymer matrix and the chemical affinity between the CNTs and the polymers. The CNTs tend to agglomerate and hold together in bundles owing to the strong van der Walls force of attraction between the individual tubes. Beyond a particular proportion, they aggregate easily, a source of stress concentration that weakens the joint strength. Therefore, it is essential to maintain a stable dispersion of CNTs within the polymer matrix to fabricate good-quality bonded joints.

Numerous dispersion techniques, including mechanical stirring, centrifugal mixing, and magnetic stirring, have been used to efficiently mix CNTs within the epoxy resins [7]. One widely utilized technique is ultra-sonication, which employs pulsed sound waves to disperse CNTs and prevent them from clumping within the epoxy resin. Ultra-sonication is most effective for dispersing small quantities of CNTs because the vibrational energy decreases significantly as the distance from the sonication tip increases. Additionally, the localized energy input during sonication can cause the CNTs near the tip to break, reducing their effective length. Maintaining the high aspect ratios of CNTs is crucial for enhancing the mechanical properties of the polymer. The calendaring process, or three-roll milling, efficiently disperses large volumes of CNTs without reducing their effective length.

4.4.3 Specimen Fabrication and Test Procedure

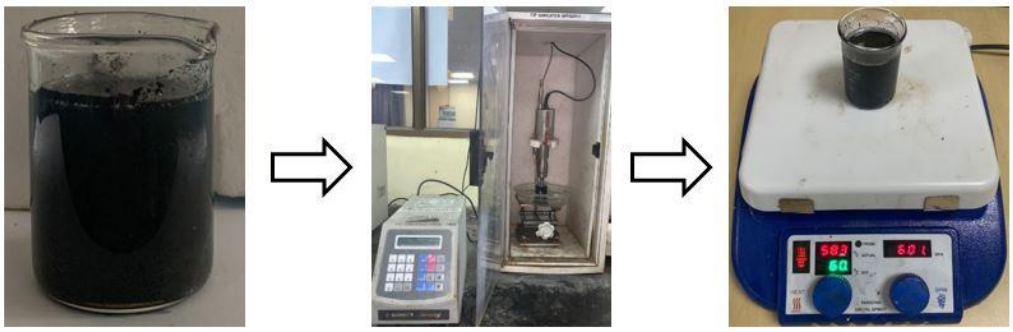

Fig. 4.8 Dispersion of MWCNTs in Resin (a) Manual mixing, (b) Ultra-sonication, and (c) Magnetic stirring

In order to achieve a bonded joint with superior interface properties, the nanofillers must be effectively dispersed in the epoxy resin. The MWCNTs of different weight proportions are dispersed in the epoxy resin using the ultra-sonication process used by most researchers [127,128]. The detailed dispersion procedures of MWCNTs in the epoxy resin are described and schematically shown in **Fig. 4.8**.

(a) The MWCNTs are first manually mixed with the resin and stirred for 5 minutes. The amount of MWCNTs used is determined by their weight relative to the combined weight of resin and hardener for each proportion of MWCNTs.

(b) The resin mixer is sonicated in a tip sonicator SONICS of 20 kHz frequency range and 500-watt power capacity. The amplitude of the sonicator is kept at 40% and 20% for the sonication time of 5 min and 1hr 55 min, respectively, with 5 min on and 2 min off cycle. The solution container is kept in an ice bath to reduce the temperature of the solution generated during the sonication process.

(c) The solution is finally mechanically stirred for another 2 hours at 60^0 C and 600 rpm, and the hardener is added afterward with a weight ratio of 3:10 to that of the resin.

Fig. 4.9 Fabricated specimens for fracture tests (a) Pristine (b) 0.1%, (c) 0.2% and 0.3% of MWCNTs

The machined surface of the aluminum substrate is initially wiped with a cloth wetted with acetone solution. The bonded surfaces of the substrates are then etched and anodized with H_2SO_4 solution as per the standard ASTM D2651 [129]. The adhesives are then applied to the surfaces of the substrate and bonded by placing it properly in a suitable fixture. All the specimens are cured for a day in the furnace at a temperature of 80^0 C, and the excess materials from the specimen are removed using abrasive paper. The prepared specimen for all wt.%

variation of MWCNTs is shown in **Fig. 4.9**. The thickness of the adhesive layer is approximately 0.1 mm, measured using a Vernier caliper. Five specimens are prepared for each nanofiller variation to confirm the repeatability of the results.

To ensure pure mode II loading, the specimens are connected to the cross-head of the universal testing machine (UTM) through Richard's [130] fixture. The fixture is made of steel with a thickness of 4 mm. All other geometric dimensions of the fixture and the specimen are shown in **Fig. 4.10 (a)** and **Fig. 4.10 (b)**, respectively. The specimens are connected to the fixture with a 13 mm diameter mild steel pin. The material properties of the fixture are already mentioned in **Table 4.2**.

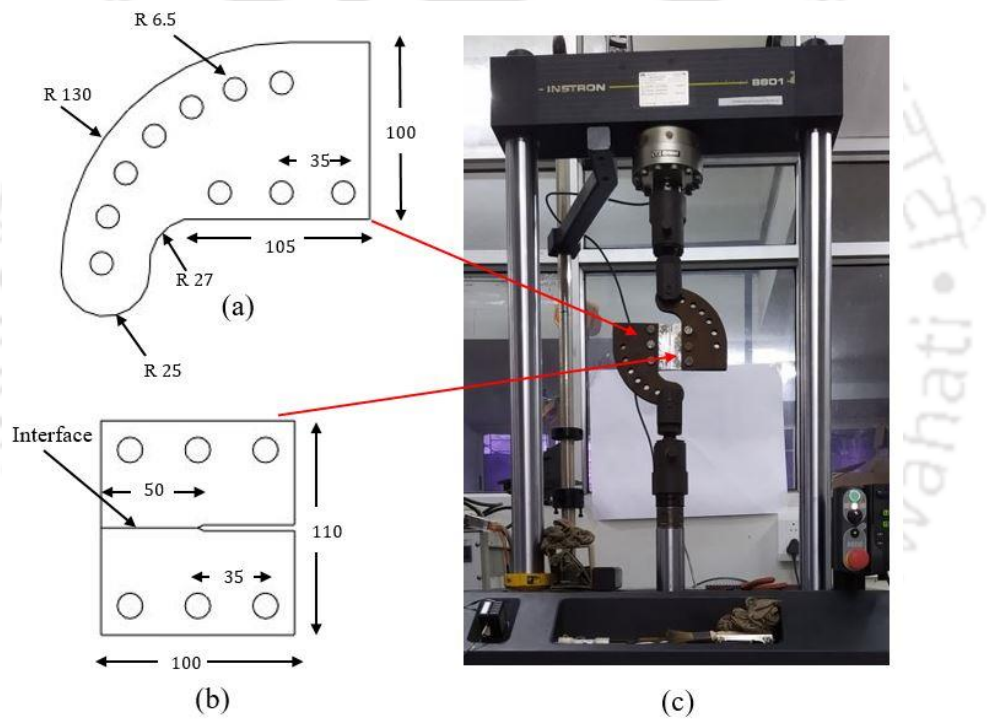

Fig. 4.10 Schematic dimensions of the (a) Fixture, (b) Specimen, and (c) Experimental setup

The strength of the bonded joints is found to vary with the changes in strain rate. Machado et al. [131] investigated the fracture toughness of CFRP and found that a higher strain decreases the mode II fracture toughness considerably. Therefore, the cross-head speed is kept constant to maintain a strain rate of 1mm/min. The Richard's fixture is connected to the upper and lower part of the cross-head of the UTM, as shown in **Fig. 4.10 (c)**. The cross-head applied the tensile force to the bonded surface through the fixture. The displacement data are simultaneously recorded till the fracture happens along the interface.

4.4.4 Experimental results

The average experimental load-displacement responses for all the variations of MWCNTs are shown in **Fig. 4.11**. Initially, the load data is recorded for each common displacement value for every category of specimens (five specimens each for pristine and all other variations of MWCNTs). The average load is obtained by summing the respective load of the specimens and dividing by the no of samples tested for every wt.% of MWCNTs.

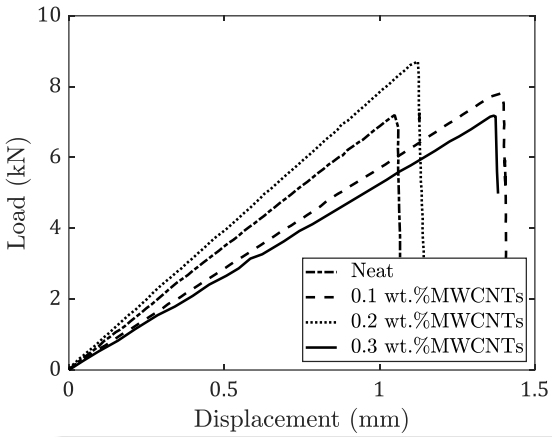

Fig. 4.11 Load displacement response of Pristine and all weight proportions of MWCNTs

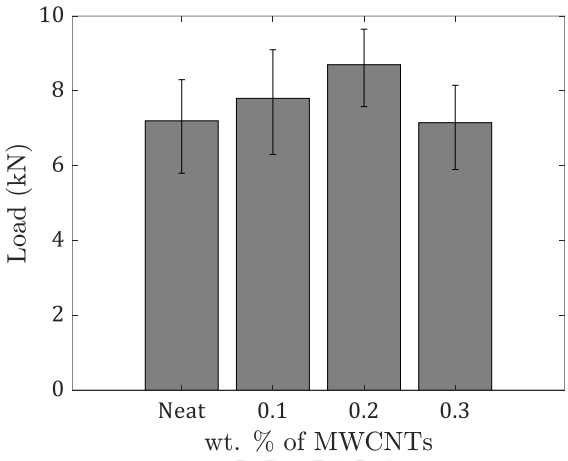

Fig. 4.12 Peak load with their standard deviations for Pristine and all wt.% of MWCNTs

The failure response is brittle for all the specimens; the load linearly increased with the displacement, followed by a drastic drop in the load-bearing capacity due to the unstable crack propagation. From the observations, as shown in **Fig. 4.12**, it is found that the maximum failure load is obtained for 0.2 wt.% of MWCNTs. The load-bearing capacity for 0.1 wt.% and 0.2 wt.% MWCNTs are 8.1% and 21.2% higher, respectively, compared to pristine bonded joints.

The failure load for 0.3 wt.% of MWCNTs is less than 0.1 wt.% and 0.2 wt.% of MWCNTs variation (approximately 1.5% less than the pristine samples). The decrease in failure load is possibly due to the agglomeration of MWCNTs, as it reduces the bonding ability of the adhesives with the aluminum substrate [132,133]. The fracture surfaces of the tested specimens are shown in **Fig. 4.13**. Visual observation revealed that the fracture occurred between the aluminum substrate and the adhesive, and the failure mode is primarily interfacial.

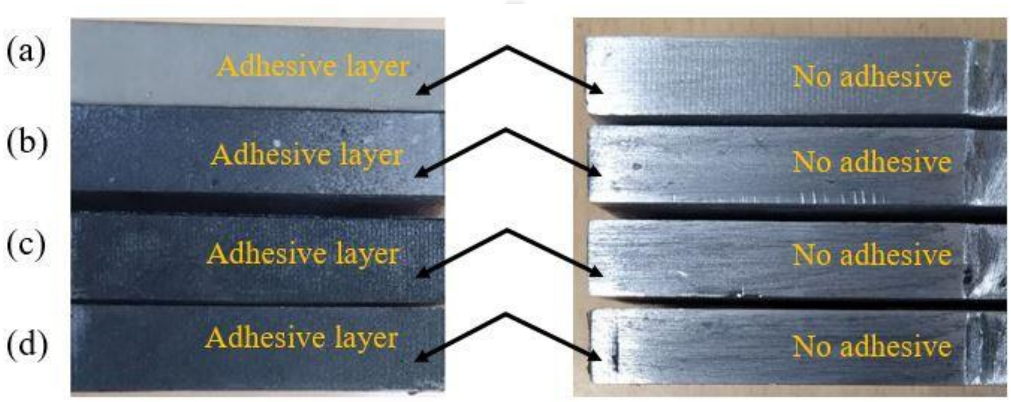

Fig. 4.13 Fracture surfaces illustrating the interface fracture of (a) Pristine, (b) 0.1 wt.%, (c) 0.2 wt.%, (d) 0.3 wt.% of MWCNTs reinforced adhesively bonded joints.

4.5 Closure

This chapter briefly reviews adhesively bonded joints, along with their potential advantages and limitations. The mode I failure behaviour of non-standard adhesively bonded PMMA specimens is studied using the routine experimental setup (Universal testing machine). The interface exhibits brittle failure behaviour, as observed from the load-displacement response.

Secondly, the mode II failure behaviour of adhesively bonded aluminum joints is performed utilizing a specially designed Richard's fixture. Three different categories of specimens are fabricated by reinforcing 0.1 wt.%, 0.2 wt.%, 0.3 wt.% of MWCNTs into the epoxy resin. These MWCNTs are evenly distributed within the epoxy resin using a standard ultra-sonication procedure, which is used by most of the researchers. The load-bearing capacity increases from pristine to 0.2 wt.% of MWCNTs reinforced adhesively bonded joints. All the specimens subjected to fracture tests possess brittle interface behaviour.

The load-carrying capacity experiences a significant decline in the case of specimens reinforced with 0.3 wt.% of MWCNTs. This decrease could result from the MWCNTs

clustering or aggregating within the epoxy resin. Agglomeration results in ineffective stress transfer between MWCNTs and epoxies. Consequently, it is strongly recommended to limit the reinforcement of hydroxyl functionalized MWCNTs up to 0.2 wt.% only when using the specific epoxy resin combination (Epofine 1564 + FINEHARD-3486-2) for fabricating adhesive-bonded aluminum joints.

Chapter 5 Numerical validation: Adhesively bonded joints

This chapter provides a fundamental overview of intrinsic and extrinsic CZMs, discusses their possible benefits and drawbacks, and the implementation methodologies in interface crack propagation. The extrinsic CZM parameters are evaluated to predict the growth of mode I interface cracks in adhesively bonded joints, as discussed in the preceding chapter. Subsequently, intrinsic and extrinsic CZM parameters are estimated to replicate the load-displacement behaviour of adhesively bonded joints reinforced with MWCNTs under mode II loading, as detailed in the earlier chapter. Finally, a correlation between intrinsic and extrinsic parameters is established and presented in the concluding section.

5.1 Intrinsic and extrinsic CZMs: Brief insight

CZM, a phenomenological model, finds application in analyzing the fracture of various materials and structures. Near the crack tip, the material softens due to void growth and micro-crack formation, as shown in **Fig. 5.1**. This softening initiates at point A, eventually resulting in a complete loss of load-bearing capacity at point B within the cohesive zone. A traction-separation relationship is employed to study the fracture behaviour within this zone.

In the case of intrinsic CZM, the traction value initially rises, approaching its maximum at the critical separation displacement. Afterward, it gradually decreases, reaching zero at the final separation displacement of the cohesive. In contrast, the extrinsic CZM exhibits non-zero traction even at zero separation displacement. The intrinsic and extrinsic CZM under mode I loading is shown in **Fig. 5.1**.

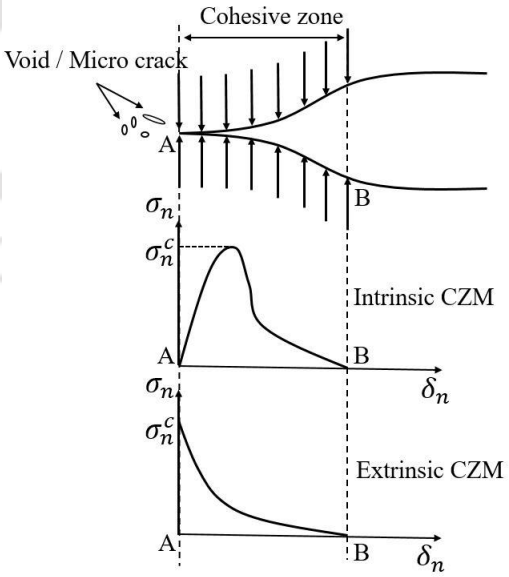

Fig. 5.1 Schematic diagram of intrinsic and extrinsic CZM

It is essential to mention that although the intrinsic CZM is relatively more straightforward for computational implementation, it cannot remove the crack tip stress singularity. Additionally, the initial stiffness of the intrinsic CZM will introduce an artificial reduction of the stiffness of the total structure [134,135]. On the other hand, the extrinsic CZM can mitigate the stress singularity at the crack tip. Still, the computational application of extrinsic CZM is challenging due to the stepwise incorporation of cohesive elements along the potential path of failure. The intrinsic CZM is more susceptible to mesh size variations than the extrinsic CZM.

5.2 Extrinsic CZMs: Numerical Implementation

5.2.1 Validation of the extrinsic CZM

The three-point bending test, shown in **Fig. 5.2**, is mainly used for simulating crack propagation under the pure mode I condition. The crack propagation methodology is identical to Moës and Belytschko's [94] analysis with a linear softening law defining cohesive behaviour. However, to the author's knowledge, no mode II work has been published within the context of removing the crack tip stress singularity using extrinsic CZM procedures. The stated problem can be considered a benchmark for predicting the interface crack propagation under mode I and II loading conditions.

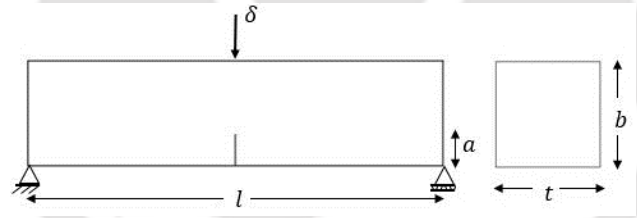

Fig. 5.2 Schematics of three-point bending (TPB) test

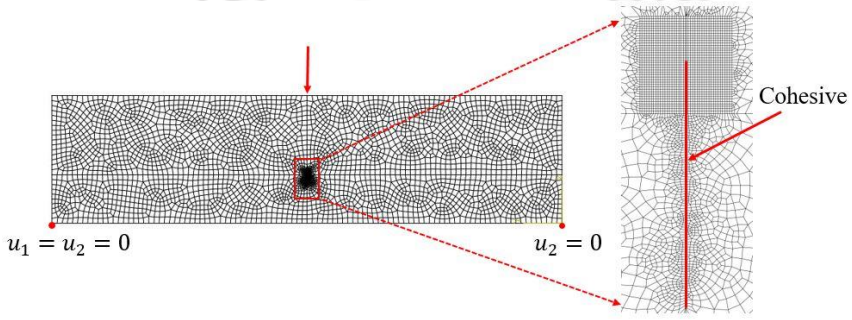

Fig. 5.3 Mesh geometry of TPB specimen with a magnified view around the crack tip

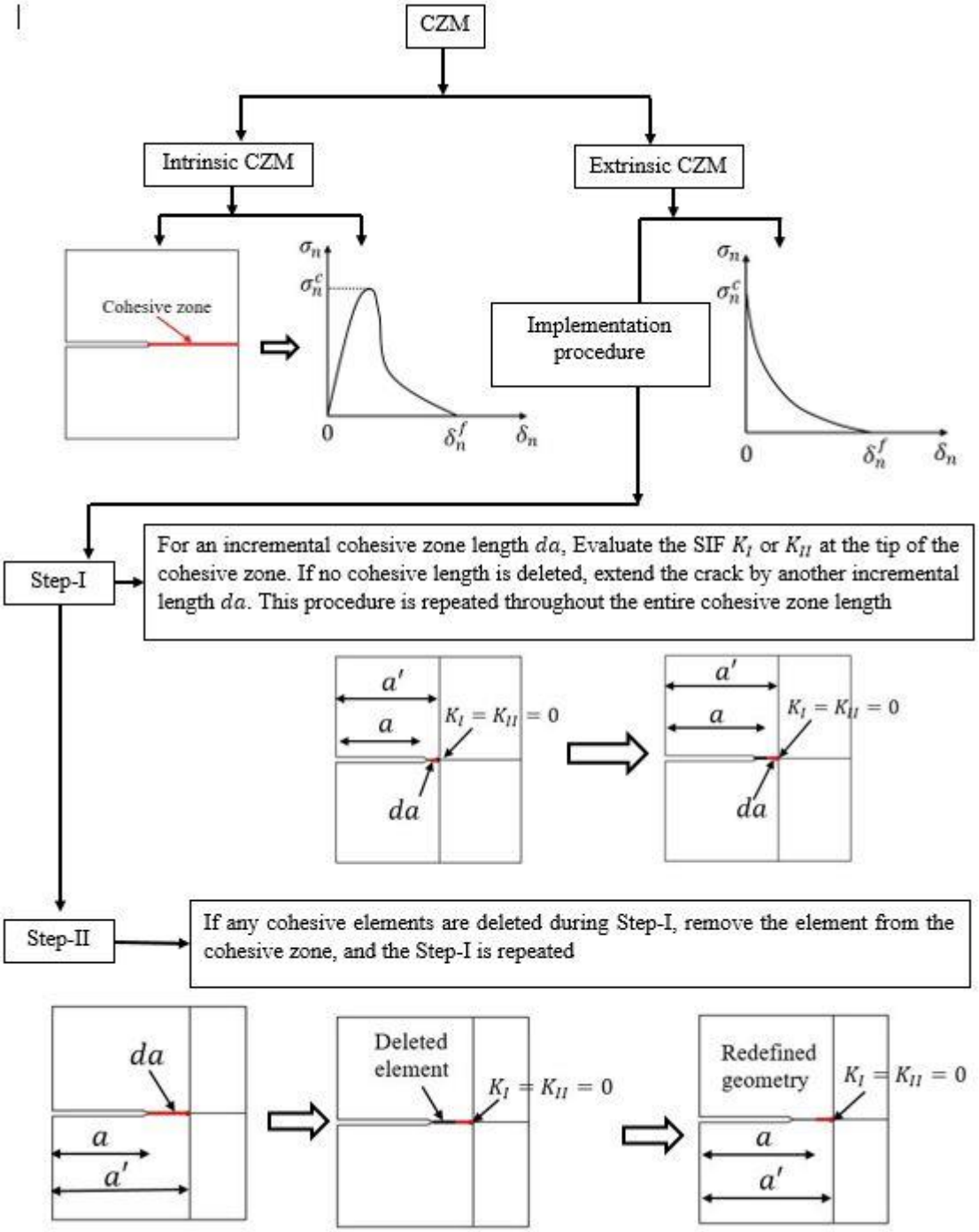

Fig. 5.4 Implementation procedures for intrinsic and extrinsic CZM

The length of the beam is l = 600 mm. The cross-section of the beam is square with $b = t = 150$ mm; an initial crack length of $a = 45$ mm, shown in **Fig. 5.2**, is considered for the analysis. t and b represented the width and depth of the beam, respectively. The load is applied on the mid-length of the beam on the top surface ahead of the crack plane. The finite element mesh consists of quadrilateral elements with a mesh size of 6 mm × 6 mm and two-dimensional interface cohesive elements with a mesh size of 0.15 mm×0.1 mm, as shown in **Fig. 5.3** inserted ahead of the initial crack length a. The plane stress condition is considered with an incremental cohesive zone length $da = 15$ mm. The properties of the bulk material are $E = 36500$ MPa, $\nu = 0.1$ with the material properties at the cohesive interface σ_n^c = 3.19 MPa. E, ν, and σ_n^c are Young's modulus, Poisson's ratio, and mode I cohesive strength, respectively. The detailed crack propagation methodology is represented in **Fig. 5.4** by a flowchart, as shown.

In most engineering structures, crack growth is usually steady and progresses slowly. In some other cases, the crack formation and its propagation are catastrophic, resulting in the abrupt loss of load-bearing capacity. The failure behaviour of the structure might range from ductile to brittle depending on its material properties, structural geometry, and loading condition. To investigate the effect of geometric dimensions (size effect) on the global load-displacement behaviour and to compare the interface brittleness, a dimensionless number (popularly known as brittleness number) was introduced by Carpinteri and Colombo [93]. The brittleness number can be defined as

$$S_E = \frac{G_n^c}{\sigma_n^c b} \tag{5.1}$$

where, G_n^c represents mode I fracture energy.

The load-deflection path presumed a positive slope for particularly brittle failure (specimen with high tensile strength and low toughness) at the interfaces. This can only be possible with simultaneous degradation of load and displacement to achieve stable and controlled crack propagation. On the other hand, a higher value of S_E, which is due to a higher value of G_n^c or a lower value of σ_n^c, resulting in a more ductile specimen. A ductile failure always proceeds with normal softening, resulting in a negative slope in the load-displacement behaviour. Two different values of brittleness number (S_E) are considered to capture the ductile to brittle failure

transition behaviour at the interface, as shown in **Fig. 5.5-Fig. 5.6.** The crack propagation procedure agreed well with the reference results of Carpinteri and Colombo [93] for both cases.

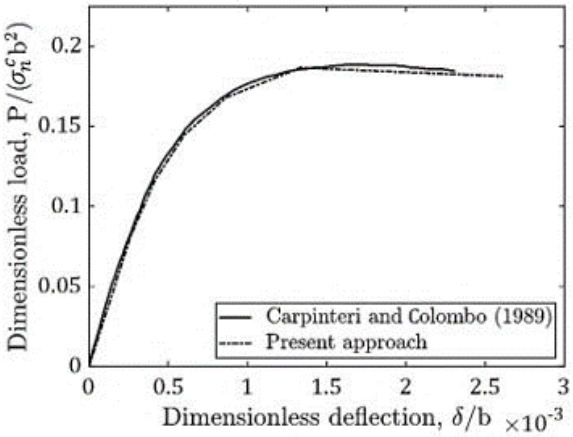

Fig. 5.5 Dimensionless load-displacement behaviour for S_E =0.00208

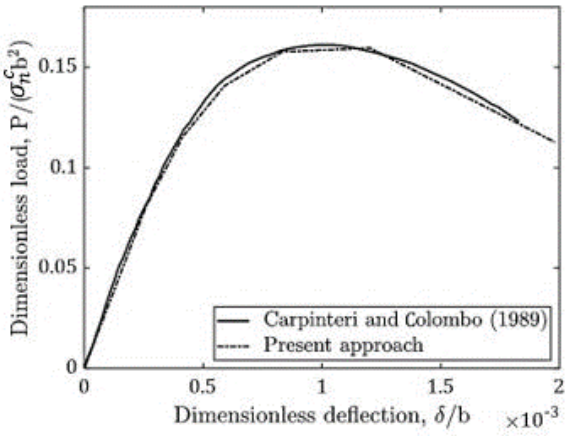

Fig. 5.6 Dimensionless load-displacement behaviour for S_E =0.000627

5.2.2 Parametric studies for the extrinsic cohesive laws

In this section, the failure response of a structure is evaluated for three different extrinsic cohesive laws, as mentioned in Eq. (3.22) of the theoretical formulation part in Chapter 3. The dimensions and material properties of the specimens are the same as those mentioned in the experimental methodology section, mentioned in Chapter 4, under the mode I and mode II loading conditions. The extrinsic crack propagation methodology is already mentioned. The depth term (b) is considered as the width of the specimen in the direction of applied load for mode II loading. However, for non-dimensional mode I fracture test, it is considered as the out of plane thickness. The plane stress condition is assumed throughout the analysis.

The specimen geometry and the FE model of the specimen under pure mode I loading condition, as mentioned in Section 4.3.2, is shown in **Fig. 5.7 (a) and Fig. 5.7 (b)**. An initial crack of length $a = r$ along the mid-plane is considered up to the center point ($x = 0, y = 0$) of the specimen. The center of the circular hole is considered a reference point for applying the boundary conditions and evaluating the interface fracture toughness. The incremental cohesive zone length da is assumed as 5 mm throughout the analysis.

The top reference point (RP-1) is constrained to move along the x-direction, while the bottom (RP-2) is constrained in both x and y directions. The displacement control boundary condition is prescribed along y-direction at the top reference point to induce crack propagation.

The substrate is modelled with 4-noded bilinear plane stress quadrilateral element (CPS4) with the 4-nodded 2D cohesive element (COH2D4) along the interface. The global size of the continuum and cohesive elements are 2 mm and 0.1 mm, respectively, based on the mesh-sensitivity analysis.

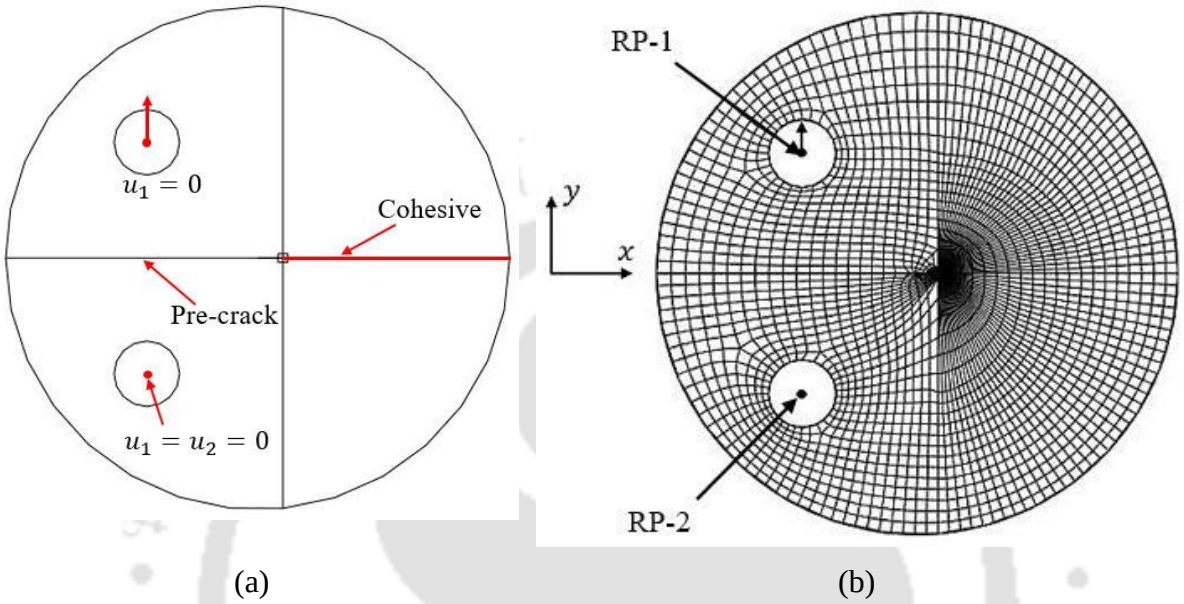

Fig. 5.7 (a) The CT geometry (b) FE mesh

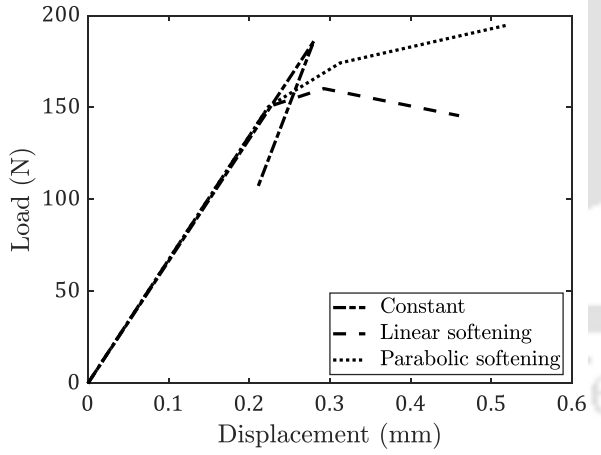

Fig. 5.8 Load-displacement response for constant, linear, and parabolic softening law (Mode I)

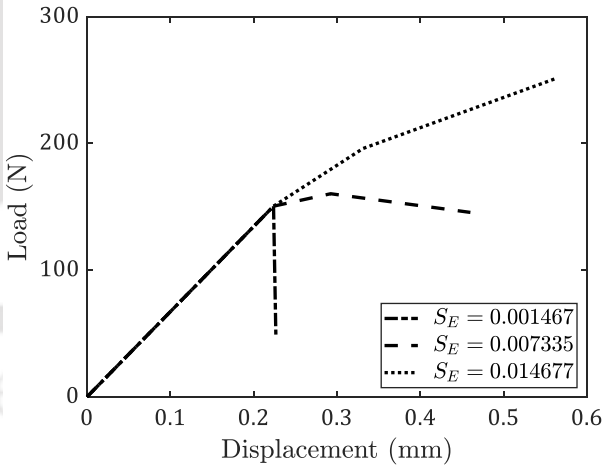

Fig. 5.9 Load-displacement response for linear-softening cohesive law to examine the size effect

Initially, a brittleness number of S_E =0.007335 is considered, corresponding to fracture energy G_n^c = 0.352 N/mm and σ_n^c =16 MPa from **Eq. (5.1)**. The load-displacement response for all three cohesive laws (constant, linear, and parabolic) is shown in **Fig. 5.8**. It is noticed

that depending upon the shape of the cohesive laws, the peak load changes and the failure behaviour of material changes from ductile to brittle. Also, the failure response with parabolic softening cohesive law is more ductile with reasonable strain hardening. For linear softening cohesive behaviour, a softening load-displacement response is observed once it reaches the peak load. However, the failure response with the constant traction cohesive law is unstable.

It is evident that for the same values for fracture energy and maximum cohesive stress, the parabolic softening cohesive law will have the highest values of critical separation δ_n^f compared to the other two cohesive laws. It prolonged the crack propagation, leading to ductile failure behaviour. So, a parabolic softening extrinsic T-S-L will result in ductile types of fracture compared to constant and linear softening T-S-Ls for the same cohesive strength and fracture energy.

The size effect of the specimen is further investigated for three different values of brittleness number shown in **Fig. 5.9**. The failure response changes from ductile to brittle with the reduction in brittleness number from 0.001467 to 0.01467 with linear softening behaviour for the cohesive interfaces.

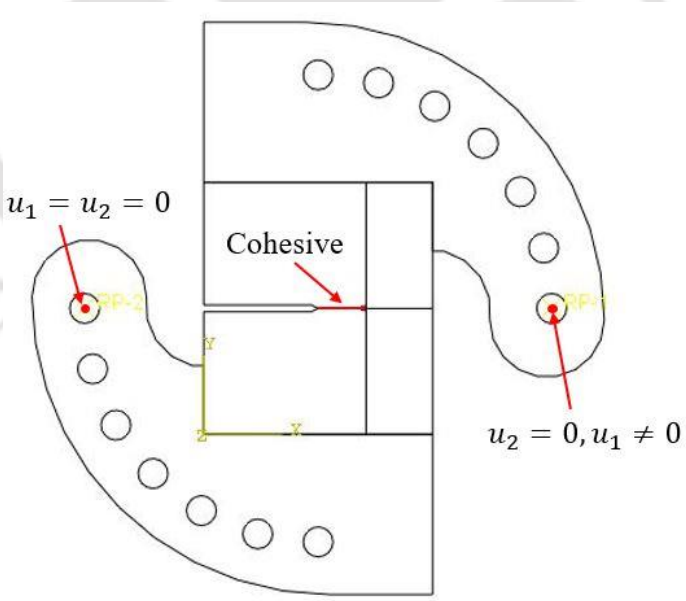

Fig. 5.10 Model geometry with the boundary conditions

The schematic drawing of the specimen with loading and the boundary conditions are shown in **Fig. 5.10**. The FE model of the specimen geometry under pure mode II loading condition, as mentioned in Section 4.4.3, is shown in **Fig. 5.11**. Two reference points (RP-1 and

RP-2) are provided in the fixture to apply the displacement-based boundary conditions. To eliminate the rigid body motion, RP-2 is allowed to move only in the x-direction. The displacement of the other reference point RP-1 is constrained in both x and y directions. The thickness of the cohesive is set at 0.1 mm with cohesive strength as σ_s^c = 200 MPa.

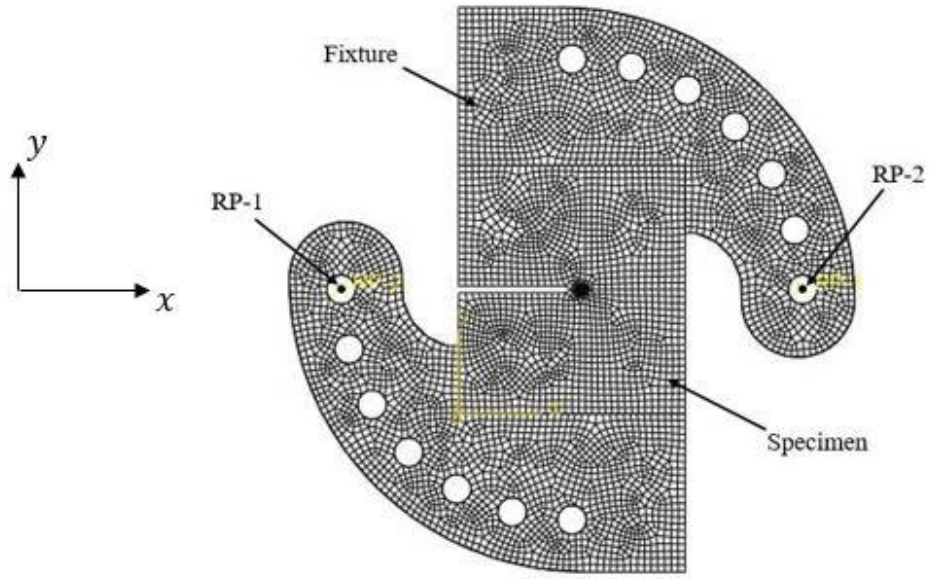

Fig. 5.11 FE mesh of the specimen and fixture

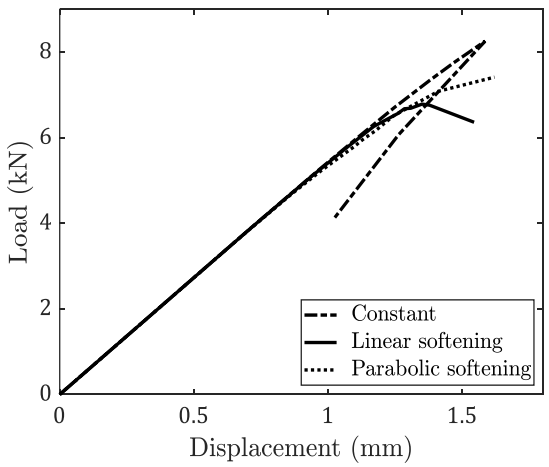

Fig. 5.12 Load-displacement response for constant, linear, and parabolic softening law (Mode II)

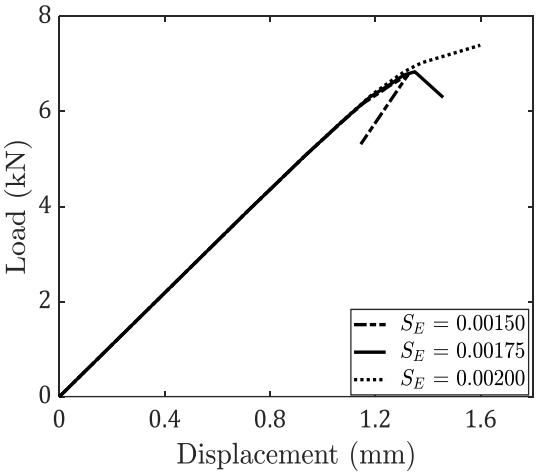

Fig. 5.13 Load-displacement response for linear-softening cohesive law to examine the size effect

One square region is considered in the specimen geometry for evaluating the SIF at the tip of the cohesive zone. The specimen and fixtures are modelled with 4-noded bilinear

quadrilateral elements with 3640 and 1723 elements in the specimen and fixture, respectively. da is set at 5 mm throughout the analysis. The size of the continuum and cohesive elements is considered 2 mm and 0.05 mm, respectively, based on sensitivity analysis.

A specific value of the brittleness number S_E =0.00175 (corresponding to fracture energy G_s^c =35 N/mm and σ_s^c =200 MPa) is assumed, and its influence on the global load-displacement response is investigated for the same three extrinsic cohesive laws used for pure mode I analysis. **Fig. 5.12** shows that the failure response is identical to mode I analysis for all three cohesive laws; however, for different values of the brittleness number.

Finally, the size effect of the specimen is studied for three different values of brittleness number shown in **Fig. 5.13**. The failure response changes from ductile to brittle with the reduction in brittleness number from 0.00150 to 0.00200 with linear softening cohesive law. A perfect brittle specimen with a sudden drop in the load after the peak value can be modelled using the information of the brittleness number. In this case, it lies between 0.00150 and 0.00175 for a linear softening T-S-L.

5.3 Numerical validation (Extrinsic CZM)

The crack propagation methodology for extrinsic CZM is already described in

Fig. 5.4. The governing parameters for the extrinsic CZM are only the cohesive strength and fracture energy. A linear softening cohesive law is considered throughout the analysis. The cohesive strength (σ_n^c) is assumed in such a way that it correlates well with the elastic response of the interface obtained from the experiment. The removal of SIF at the tip of the cohesive zone is also sequentially carried out.

The assumed cohesive strength value is 16 MPa to accurately predict the elastic response of adhesively bonded joints under mode I loading. Moreover, It is observed from **Fig. 5.14** that for a brittleness number S_E = 0.001467, the numerical results obtained from the present procedure are very close to those obtained from the experiments. So, the current procedure can be efficiently used to capture the ductile to brittle fracture transition behaviour of the interface fracture mechanics. The out-of-plane thickness of the specimen is considered as 3 mm to accurately predict the peak load of the specimen observed under the fracture toughness test.

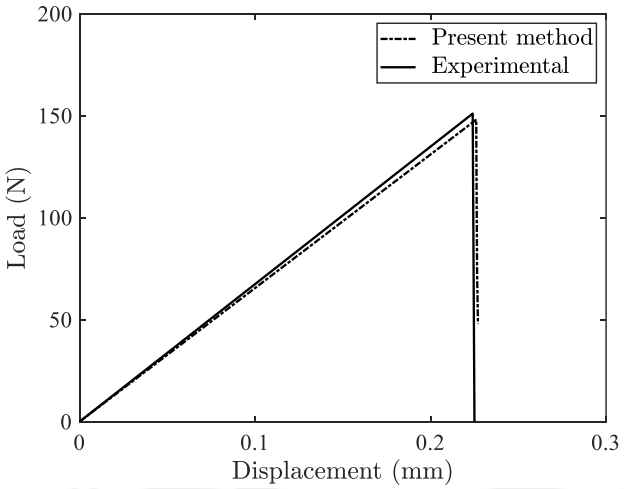

Fig. 5.14 Comparison of results obtained from the experiment and the present method

Four different cohesive strengths (σ_s^c) values are obtained for pristine and three different variations of MWCNTs (0.1 wt.%, 0.2 wt.%, and 0.3 wt.%) reinforced adhesively bonded joints under the mode II loading condition. It is observed that for higher values of brittleness number under mode II loading, the global failure behaviour of the specimen is mainly influenced by the continuum element placed ahead of the cohesive zone. The cohesive zone length incrementally varied from da = 5 mm to 45 mm, and their load-displacement responses were recorded. The estimated CZM parameters are provided in **Table 5.1**.

5.4 Numerical validation (Intrinsic CZM)

This section evaluates the intrinsic CZM parameters for MWCNTs reinforced aluminum specimens subjected under mode II loading conditions. The obtained parameters are then compared with their extrinsic counterpart, based on which some specific conclusions are made. It must be noted that, due to the unique deformation behaviour of cohesive elements along the cohesive zone, an intrinsic CZM cannot be used to capture the brittle load-displacement response of the interface under mode I loading conditions.

One of the most popular ways to estimate the intrinsic CZM parameters (cohesive strength, stiffness, and fracture energy) is to compare the results obtained from the experiment with the numerical simulation. Cohesive strength (σ_s^c) and fracture energy (G_s^c) are directly obtained from the peak load (P_{max}), and failure displacement is obtained for each MWCNT variation under load-displacement response. It is found that any increase in the cohesive stiffness increases the load vs. displacement response slope in the linear elastic regime. Accordingly,

based on iterations, the K_s is chosen in such a way that the elastic responses obtained from the numerical study correlated well with the experimental observations.

For a specimen subjected to pure shear loading, as shown in the experimental methodology part of the adhesively bonded joint under mode II loading in the previous chapter, it results in uniform and maximum shear stress distribution across the interface. The interface shear stress obtained from the experiment can be considered as cohesive strength σ_s^c in the numerical simulation. For a 50 mm interface length with 10 mm thickness, as shown in **Fig. 4.10 (b),** the cross-section of the adhesive bond across the interface is 500 mm^2. The maximum load obtained for each proportion of MWCNTs divided by the interface bond area will give the values of the cohesive strength σ_s^c. Numerically, the cohesive strength:

$$\sigma_s^c = \frac{P_{max}}{A_s} \tag{5.2}$$

where A_s is the sheared area, and P_{max} is the maximum load under load-displacement behaviour obtained from the experiment, as shown in Fig. 4.11 in the previous chapter.

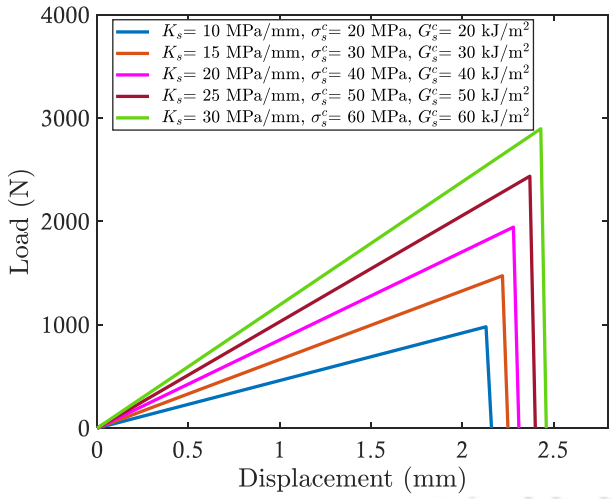

Fig. 5.15 Load-displacement responses with different damage initiation/failure combinations ($\delta_s^c = \delta_s^f$)

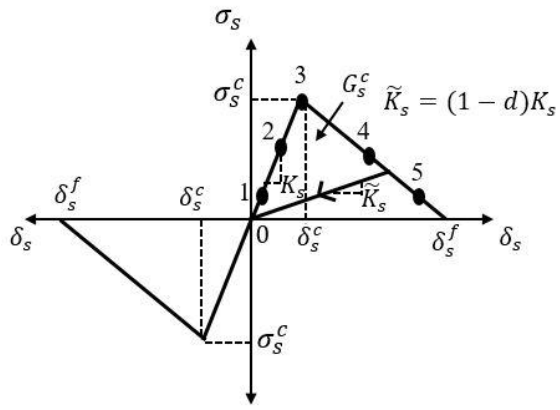

Fig. 5.16 Mode II triangular CZM

To investigate the influence of cohesive stiffness, the CT specimen is modelled under pure mode II with a triangular T-S-L. The cohesive stiffness varies from 10 to 30 MPa/mm, and the global load-displacement behaviour is shown in **Fig. 5.15**. As the failure response of the adhesive is perfectly brittle, it can be considered that the adhesive undergoes rapid damage evolution. Therefore, the critical separation corresponding to the damage initiation δ_s^c is equal

to the displacement at the failure δ_s^f of the cohesive, as shown in **Fig. 5.16**. In that scenario, the mode II fracture energy is estimated as:

$$G_s^c = \frac{1}{2}\sigma_s^c \delta_s^f \tag{5.3}$$

The intrinsic cohesive zone parameters for all proportions of MWCNTs are provided in **Table 5.1.**

Intrinsic CZMs are straightforward to implement. Additionally, depending upon the fracture energy values, one can obtain a wide variety of load-displacement behaviour for pure mode II loading, ranging from ductile to brittle. The problems of removing the crack tip stress singularity still need to be addressed, even though implementing intrinsic CZM is computationally more convenient than the extrinsic CZM. The extrinsic CZM parameters – cohesive strength and fracture energy reported in **Table 5.1**, differ considerably from the intrinsic parameters.

Table 5.1 Estimated CZM parameters for MWCNTs reinforced bonded joints

wt. % of MWCNTs	Intrinsic CZM parameters			Extrinsic CZM parameters		
	K_s (MPa/mm)	σ_s^s (MPa)	G_s^c (kJ/m^2)	σ_s^s (MPa)	$\sigma_s^s . t$ (N/mm)	G_s^c (kJ/m^2)
Pristine	15.2	14.40	6.82	158	214.88	26.70
0.1% MWCNTs	12.2	15.62	10	215	232.20	37
0.2% MWCNTs	18	17.41	8.41	170	241.40	28.80
0.3% MWCNTs	11.5	14.31	8.90	206	212.18	34.80

Ideally, the presented extrinsic crack propagation methodology is initially developed for continuous specimens with no bonded interface. As the interfaces are significantly weaker in adhesively bonded joints, the out-of-plane thickness (t) is set to correlate well with the stiffness of the experimental load vs. displacement response. Accordingly, the t for the pristine, 0.1%, 0.2%, and 0.3wt.% of MWCNTs are set at 1.36 mm, 1.08 mm, 1.42 mm, and 1.03 mm, respectively. Any other combination will not give the expected response. The experimental and

numerical results (both intrinsic and extrinsic CZM) are shown in **Fig. 5.17 (a)-Fig. 5.17 (d)**. The numerical results agreed well with the experimental observation. On the other hand, for the intrinsic CZM, the out-of-plane thickness t =10 mm, which is the same as that of the specimen thickness used in the experimental section.

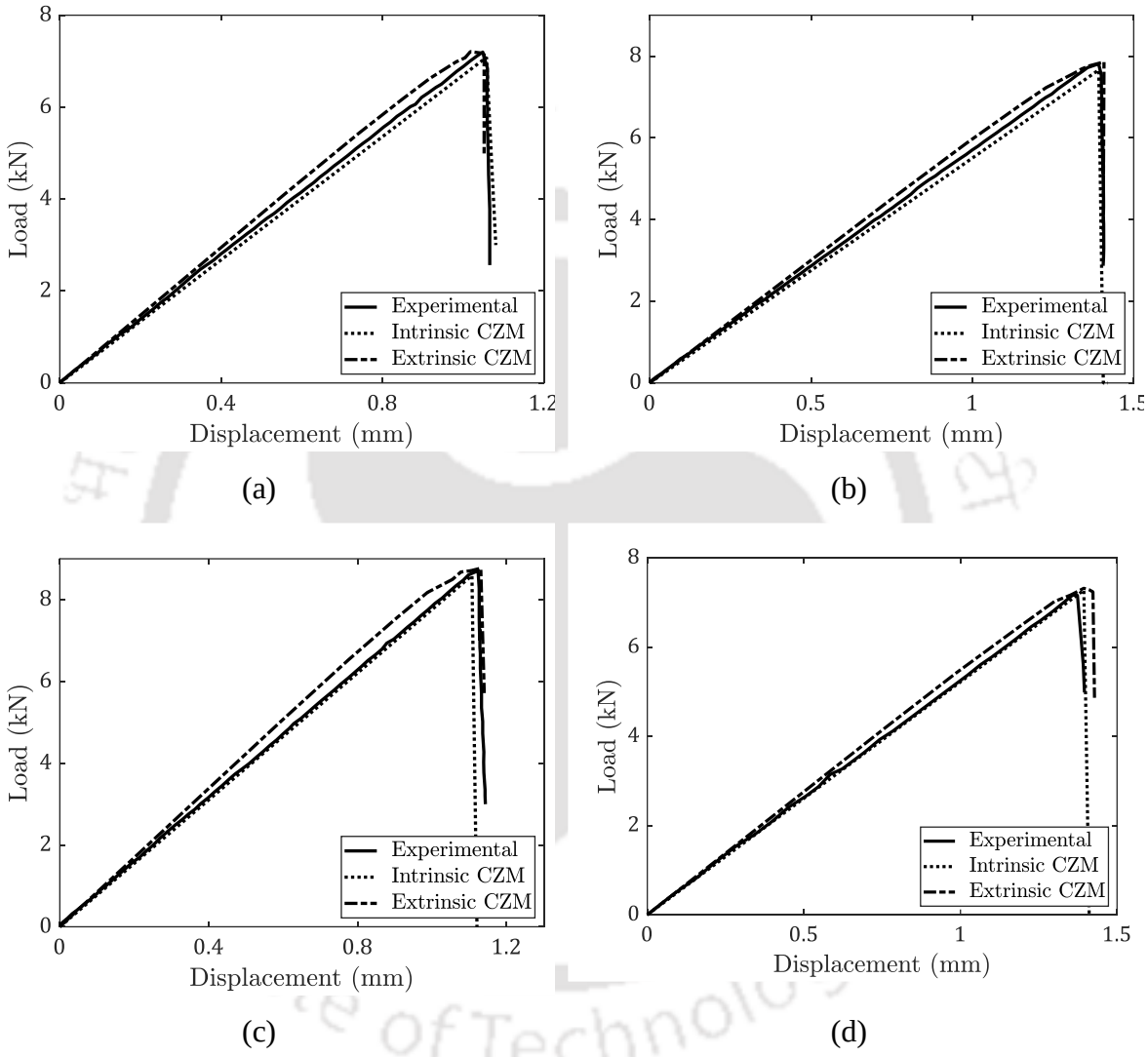

Fig. 5.17 Numerical validation of load-displacement response for (a) Pristine, (b) 0.1 wt.%, (c) 0.2 wt.%, and (c) 0.3 wt.% of MWCNTs

The intrinsic CZM parameters, i.e., cohesive strength and fracture energy, are precisely calculated using Eq. (5.2) and Eq. (5.3). As the cohesive strength depends entirely on the peak load of the load-displacement response, the cohesive strength for 0.2 wt. % of MWCNTs is the highest. However, as seen in Eq. (5.3), the fracture energy (G_s^c) of the intrinsic CZM depends

on the displacement at failure in addition to the cohesive strength (σ_s^c). Therefore, among all the MWCNTs variations, 0.1 wt.% MWCNTs sustain maximum failure separation and, therefore, exhibit maximum fracture energy (G_s^c). On the other hand, the load vs. displacement response of the extrinsic CZMs depends upon the ratio of fracture energy to the product of the width of the specimen and the cohesive strength for any specific cohesive law. The ratio is almost constant at approximately 0.0017 for pristine and all other variations of MWCNTs with the assumed linear-softening extrinsic cohesive law. This supports the conclusions made at the end of Section 5.2.2. It implies that for a set of bulk material properties, geometric dimensions, and the type of test, the brittleness number remains constant for simulating a particular manner of load vs. displacement response, e.g., a perfectly brittle response. The cohesive fracture energy and strength can change with the type of adhesives, but they get tuned to a specific brittleness number to obtain a particular load vs. displacement response.

It is observed that there is a good correlation between the cohesive strength (σ_s^c) of the intrinsic CZM with the $\sigma_s^c . t$ (cohesive strength times the thickness) of the extrinsic CZM. A higher displacement at failure observed during the experiment requires an increase in extrinsic cohesive strength (σ_s^c) to nullify the SIF. Consequently, the displacement at failure in the experiments shown in **Fig. 5.17** and the extrinsic cohesive strength (shown in **Table 5.1**) follow a similar trend. In summary, the intrinsic CZM strength solely depends on the experimental peak load. However, the extrinsic cohesive strength relies upon the displacement at the failure of the load-displacement response.

5.5 Closure

This chapter outlines an extrinsic CZM procedure to investigate the mode I and mode II interface fracture behaviour of adhesively bonded joints. The extrinsic CZM procedure is initially validated with the TPB test reference results. A parametric study is also carried out to investigate the influence of the shape of the cohesive law and the brittleness number S_E on the interface load vs. displacement response.

Moreover, the extrinsic CZM parameters are evaluated while validating the load-displacement response of adhesively bonded joints under mode I and mode II loading. The

intrinsic CZM parameters are also estimated for MWCNTs reinforced adhesively bonded joints, and a comparison is made with their extrinsic counterpart.

Chapter 6 Experimental procedure: Composite delamination

This chapter uses an experimental approach to assess the interface characteristics of CFRP reinforced with MWCNTs subjected to mode I and mode II loading conditions. The interface normal and shear strength are initially evaluated using cross-tension and short beam shear (SBS) tests, respectively. Moreover, the mode I and mode II fracture energy is estimated using standard test procedures, such as the DCB and ENF tests.

The mixed-mode (I/II) fracture toughness of the composites is also estimated for three different mixed-mode ratios. Finally, the mode I, mode II, and mixed-mode (I/II) fracture surfaces of the specimen are investigated to understand the interface fracture mechanism.

6.1 Experimental methodology

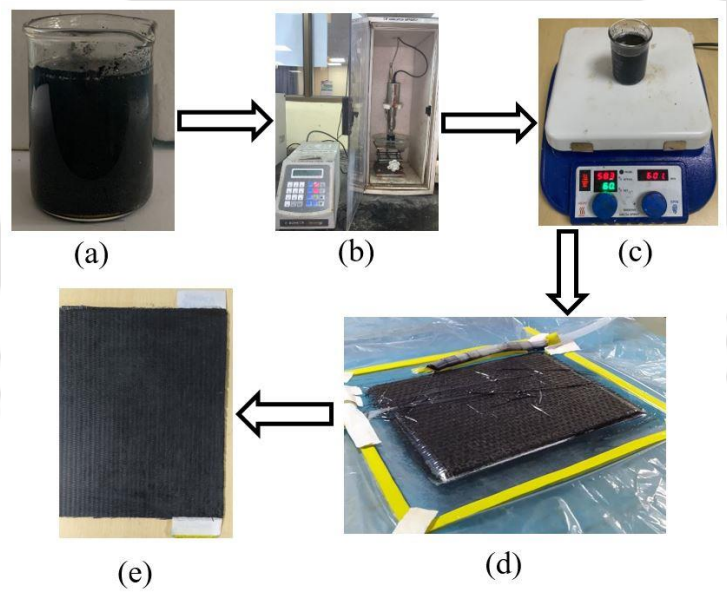

Fig. 6.1 Composite fabrication process (a) Manual mixing of MWCNTs with the resin, (b) Ultra-sonication, (c) Magnetic stirring, (d) Composite fabrication process, and (e) Fabricated composite plate

The unidirectional carbon fiber (grade 200 GSM) is supplied by FIBER REGION, INDIA. The fiber diameter is 10-20 μm with approximated elastic modulus and tensile strength equal to 230 GPa and 2750 MPa, respectively. The material properties and geometric dimensions of the MWCNTs and epoxy resin are the same as those used to fabricate adhesively bonded joints,

as mentioned in Chapter 4. Three different MWCNTs wt.% of 0.1%, 0.2%, and 0.3% are used in the present study. The ultra-sonication process effectively disperses the MWCNTs into the epoxy resin. The experimental methodology section in Chapter 4 has already presented the step-wise dispersion of MWCNTs in the epoxy resin.

6.1.1 Fabrication of carbon fiber-reinforced epoxy nanocomposites

Due to the higher aspect ratios, the MWCNTs are segregated while passing through each layer of fibers. Therefore, traditional hand lay-up techniques with vacuum bagging are used to fabricate the composite instead of the resin transfer molding (RTM) process. This entire procedure involves pouring a mixture of resin and hardener onto a single layer of unidirectional carbon fiber, maintaining a fiber-matrix volume fraction $V_f = 50\%$. A paintbrush and a hand roller are used to distribute the resin-hardener mixture across the fiber layer uniformly. This process is repeated for each subsequent layer of carbon fiber. A Teflon sheet with a thickness of 0.1 mm is inserted in the middle of the composite laminate to create an initial crack. The entire fabrication process is shown in **Fig. 6.1**. After fabrication, the test coupons are cut from the laminated composite plate using a shearing cutter. Specific geometric dimensions and the number of fiber layers used for each test category are detailed in **Table 6.1**.

6.2 Test procedures

The CZM parameters of laminated composite can be evaluated with direct and indirect test procedures, which involve customized experimental setup and tiresome trial and error processes. To overcome these limitations, specific fracture characterization tests are conducted. The key advantage of all these test procedures is their sensitivity to individual cohesive parameters (cohesive strength and fracture energy) in their respective loading modes. Here, the cross-tension test determines the mode I cohesive strength, while the SBS test estimates the mode II cohesive strength of the composites.

Moreover, the fracture energy in mode I and mode II loading are evaluated using the standard DCB and ENF test procedures. It is essential to mention that the shape of the cohesive law plays a significant role in influencing the failure response of the structure. Therefore, in the present study, a triangular T-S-L is employed — a choice made by numerous researchers for accurately predicting composite delamination [136].

Table 6.1 Specimen geometry and standards for conducting specific fracture characterization test

Tests	Standard procedure	No of lamina	Dimensions $(l \times b \times h)$ in mm^3	Crack length (a) in mm
Cross-tension test	Non-standard	16	$50 \times 50 \times 3.2$	—
SBS test	ASTM D2344 [137]	30	$36 \times 12 \times 6$	—
DCB tests	ASTM D5528 [138]	16	$160 \times 21 \times 3.2$	65
ENF tests	ASTM D7905 [139]	16	$140 \times 21 \times 3.2$	50
MMB test	ASTM D6671 [140]	16	$150 \times 21 \times 3.2$	50

6.2.1 Estimation of mode I interface strength

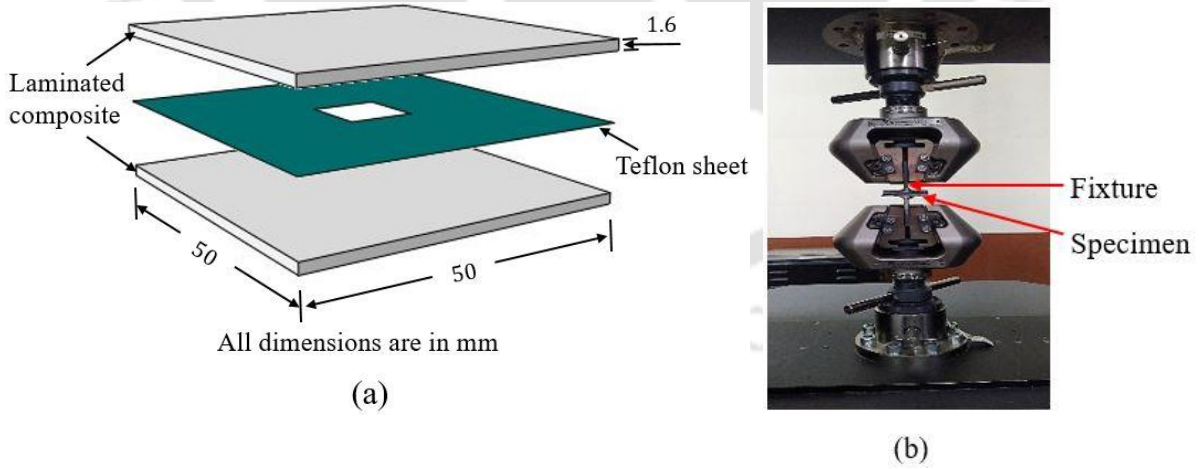

Fig. 6.2 (a) Schematic of cross-tension specimen geometry, and (b) Experimental setup

To perform the cross-tension test, a Teflon sheet is inserted into the central portion of the composite laminate, as shown in **Fig. 6.2 (a)**. The Teflon sheet covers all laminate edges except for a square region measuring 10 mm × 10 mm at the center. The backing plates are made by

welding two mild steel square plates in a 'T' shaped configuration. An uneven texture is made on the bonded surface of the backing plate using a rough file to improve adhesion between the specimen and the backing plate. The surface of the backing plate is then cleaned with acetone, glued with the composite specimen using Araldite klear adhesive, and fixed in a bench vice under even clamping force. The specimen-fixture assembly is cured for 24 hrs. in the furnace at 80^0 C. After curing, the side surfaces of the specimens are polished with sandpaper to remove any excessive adhesives.

The cross-tension test is performed with a 0.5 mm/min displacement rate in a SHIMADZU 100 kN Universal Testing Machine (UTM), as shown in **Fig. 6.2 (b)**. The cohesive strength σ_n^c is calculated using the formula

$$\sigma_n^c = \frac{P_{max}}{A_N} \tag{6.1}$$

where P_{max} and A_N are the maximum load and the cohesive area under the cross-tension test, respectively.

6.2.2 Evaluation of interlaminar shear strength

The SBS test is commonly employed to investigate interlaminar shear strength due to its relatively more straightforward specimen fabrication and simplified test procedures [141–143]. The SBS rectangular specimen geometry is schematically shown in **Fig. 6.3 (a).** When the transverse shear load exceeds the interlaminar shear strength, delamination occurs between the layers of reinforcing fibers.

To conduct the SBS tests, all specimens are subjected to a TPB test in a SHIMADZU 100 kN UTM with a crosshead speed of 1 mm/min, as shown in **Fig. 6.3 (b)**. The specimen is considered to have failed due to interlaminar shear if its load drops by 30% after reaching the peak load. The interlaminar shear strength (ILSS) for a beam with a rectangular cross-section can be calculated using the following formula.

$$\sigma_s^c = 0.75\frac{P_{max}}{b.t} \tag{6.2}$$

where b and t denote the width and thickness of the specimen, respectively. P_{max} corresponds to the maximum load observed in the load-displacement response. The distance between the supports is four times the thickness of the specimen.

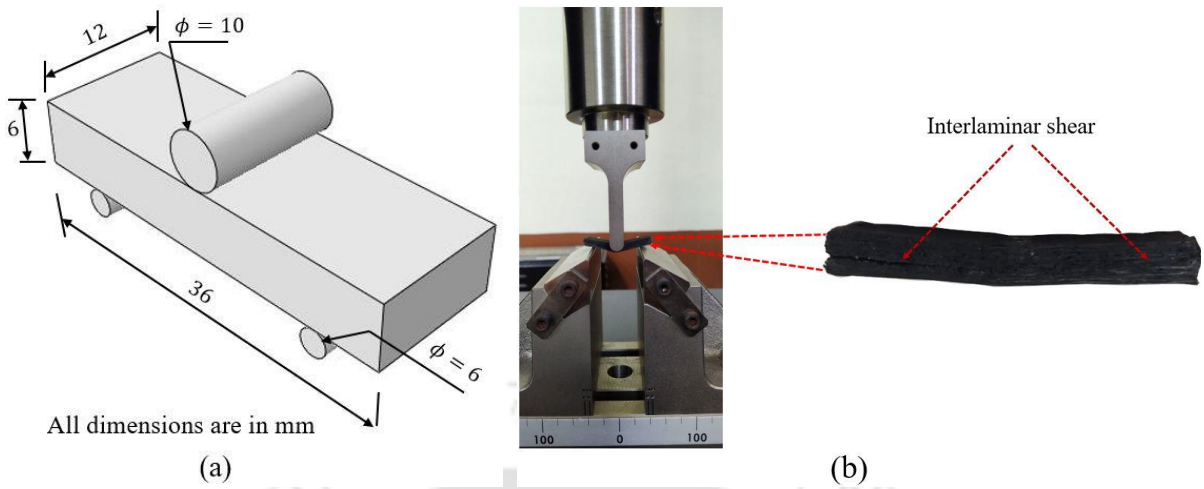

Fig. 6.3 (a) Schematic of SBS specimen geometry, and (b) Experimental setup

6.2.3 Evaluation of mode I interlaminar fracture toughness

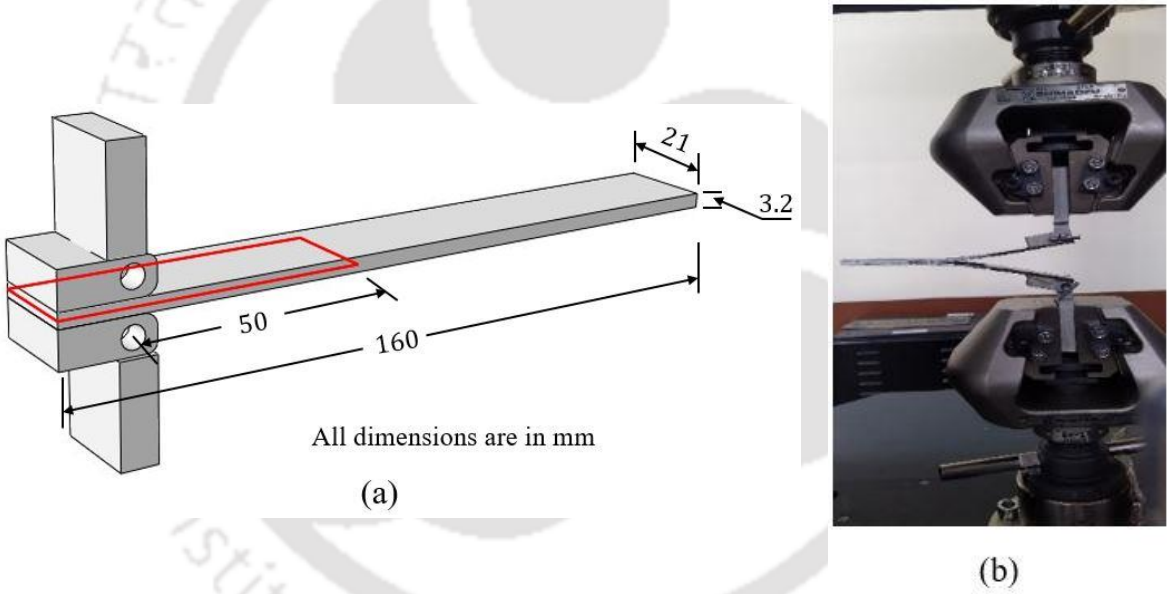

Fig. 6.4 (a) Schematic of DCB specimen geometry, and (b) Experimental setup

DCB test is most frequently used for evaluating the mode I fracture toughness of the composite laminate. Here, all specimens have an initial crack length of approximately 65 mm, comprising a 50 mm initial delamination length and an additional 15 mm length for bonding the loading block with the upper and lower parts of the composite laminate, as shown in **Fig. 6.4 (a)**. The tests are conducted using a SHIMADZU 100 kN UTM with a 5 mm/min crosshead speed, as illustrated in **Fig. 6.4 (b)**.

A modified beam theory is employed to estimate the strain energy released rate (SERR) for the DCB test specimen. For the DCB specimen, the SERR can be evaluated as

$$G_n^c = \frac{3P\delta}{2ba} \tag{6.3}$$

where P and δ represent the instantaneous load and load point displacement. b and a define the specimen width and instantaneous delamination length, respectively.

Nevertheless, the procedure above tends to overestimate the SERR values because of the rotation of the delamination front. To address this issue, a correction factor Δ is introduced to adjust the delamination length. This correction factor is obtained by creating a least square fit of the cube root of compliance $C^{1/3}$ with δ [138]. As a result, the modified SERR can be calculated as

$$G_n^{corrected} = \frac{3P\delta}{2b(a+\Delta)} \tag{6.4}$$

6.2.4 Evaluation of mode II interlaminar fracture toughness

The mode II fracture toughness of unidirectional fiber-reinforced polymer composites is estimated using the ENF test method under pure mode II loading conditions. **Fig. 6.5** (a) shows the schematic dimensions of an ENF test specimen. The tests are conducted on a three-point bend fixture with a 0.5 mm/min crosshead speed, as shown in **Fig. 6.5 (b)**. The Compliance calibration (CC) procedure determines the mode II fracture toughness of the composite laminate, which is already provided in the ASTM standard [139]. The mode II fracture toughness can be estimated as

$$G_s^c = \frac{3mP_{max}a_0^2}{2b} \tag{6.5}$$

The compliance calibration coefficient, denoted as m, is derived by plotting compliance against the cube of the crack length, a. The width of the specimen is represented by b, and P_{max} corresponds to the peak load observed during the fracture test. Additionally, the initial crack length a_0, employed in the fracture test, is set at 30 mm.

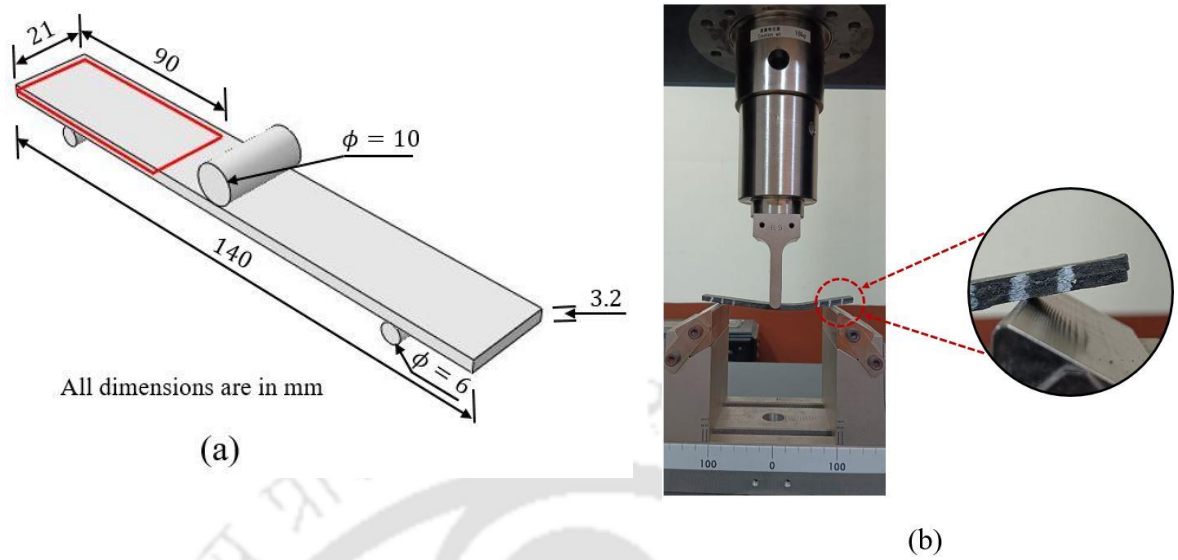

Fig. 6.5 (a) Schematic of ENF specimen geometry, and (b) Experimental setup

6.2.5 Evaluation of mixed-mode (mode I /mode II) interlaminar fracture toughness

The mixed-mode interlaminar fracture toughness is evaluated using the MMB test. To control the mixed-mode ratio, the lever length 'c' of the customized fixture, as shown in **Fig. 6.6 (a),** can be adjusted. Three specific lever lengths of 104 mm, 68 mm, and 52 mm are considered, corresponding to mixed-mode ratios G_S/G equal to 0.2, 0.3, and 0.4, respectively. All tests are performed in displacement mode with a 1 mm/min crosshead speed, as shown in **Fig. 6.6 (b)**. The lever length can be determined using the following formula

$$c = \frac{12\beta^2 + 3\alpha + 8\beta\sqrt{3\alpha}}{36\,\beta^2 - 3\alpha} L \tag{6.6}$$

In the given context, $'L'$ refers to the half-span length of the MMB apparatus. The parameters α and β in the equation are related to the mixed-mode transformation parameter and the non-dimensional crack length correction used for determining the lever length. These values are obtained from the following expression.

$$\alpha = \frac{G}{G_S} - 1$$
$$\beta = \frac{a + \chi h}{a + 0.42\chi h} \tag{6.7}$$

where a represents the delamination length, and χ denotes the crack length correction parameter given as

$$\chi = \sqrt{\frac{E_{11}}{11\,G_{13}}\left\{3 - 2\left(\frac{\Gamma}{1+\Gamma}\right)^2\right\}} \tag{6.8}$$

where E_{11} and E_{22} are the longitudinal and transverse modulus of elasticity, respectively. G_{13} corresponds to the shear modulus in the out-of-plane direction. The parameter Γ represents the transverse modulus correction parameter and is defined as follows

$$\Gamma = 1.18\frac{\sqrt{E_{11}E_{22}}}{G_{13}} \tag{6.9}$$

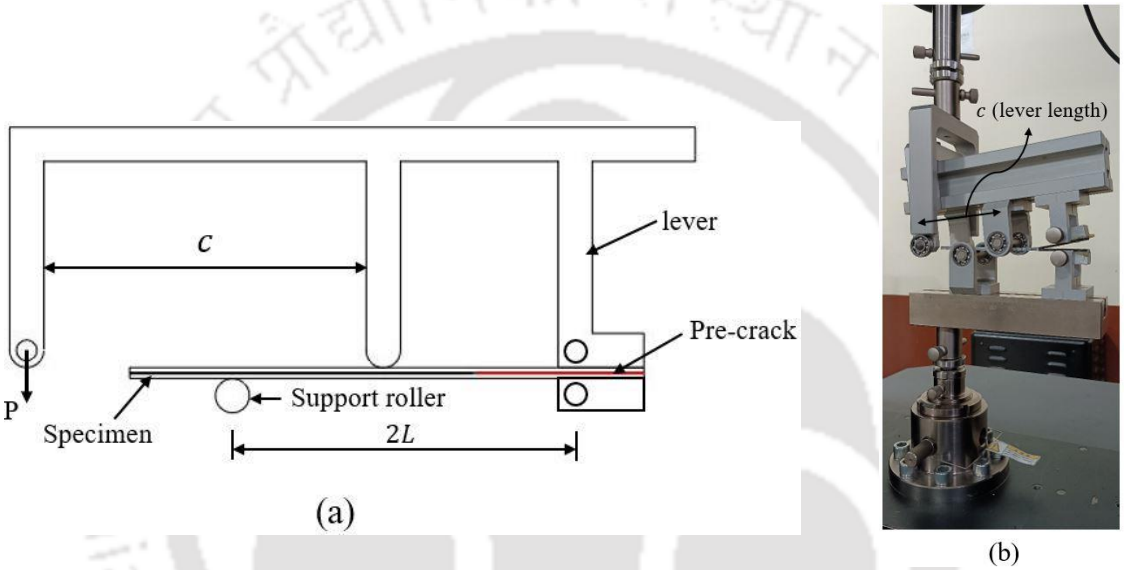

Fig. 6.6 (a) Schematics of MMB specimen geometry with fixture, and (b) Experimental setup

6.3 Results and discussions

The load-displacement responses of pristine and MWCNTs-reinforced specimens are obtained following the experimental procedures. The strength and toughness of the composite specimen are evaluated for mode I and mode II loading scenarios, employing the methodologies detailed in the earlier section.

6.3.1 Evaluation of mode I interface strength

All the specimens subjected to cross-tension test exhibit interface failure, as shown in **Fig. 6.7 (a)**. The load-displacement response of all the specimens is brittle; the load increases linearly with the displacement until a drastic drop follows the maximum load. The mode I cohesive strength of 0.2 wt.% MWCNTs reinforced composite specimen is the highest compared to pristine and other reinforced test specimens. The average mode I interface strength

for 0.2 wt.% MWCNTs reinforced test coupons are approximately 20 MPa, approximately 25% higher than the pristine composite specimen. Consequently, the average mode I cohesive strength for 0.1 and 0.3 wt.% of MWCNTs reinforced composite specimens is about 13.1% and 9.37% higher than the pristine composite, as shown in **Fig. 6.7 (b)**.

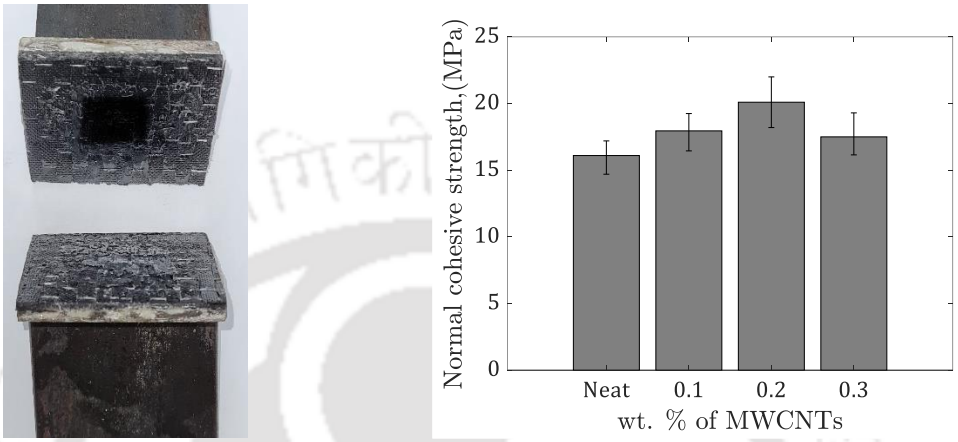

(a) (b)

Fig. 6.7 (a) Interface failure of CT specimen, and (b) Mode I interface strength for different MWCNTs variation

6.3.2 Evaluation of mode I fracture toughness

The representative load-displacement behaviour of pristine and MWCNTs reinforced composite specimens are shown in **Fig. 6.8 (a)**. Although all the specimens exhibit identical stiffness, the load-bearing capacity of 0.2 wt.% of MWCNTs reinforced composite specimen is maximum. The peak load of all the specimens gradually increased from pristine to 0.2 wt.% of MWCNTs, and beyond that, it decayed.

The resistance curve (R-curve) represents the variations of mode I fracture toughness (or SERR) as a function of the delamination length, as shown in **Fig. 6.8 (b)**. The R-curve shows that the inclusion of MWCNTs enhanced the mode I interlaminar fracture toughness (IFT). The CFRP test coupons reinforced with 0.2 wt.% of MWCNTs exhibit the highest IFT compared to pristine and other MWCNTs-reinforced specimens. The maximum IFT (G_n^c) for 0.2 wt.% of MWCNTs reinforced specimens is around 1.30 kJ/m^2, approximately 47% higher than the pristine composites. The IFT values for 0.1 and 0.3 wt.% of MWCNTs reinforced specimens are 0.95 kJ/m^2 and 0.92 kJ/m^2, approximately 7.9% and 4.3% higher compared to pristine composite specimens.

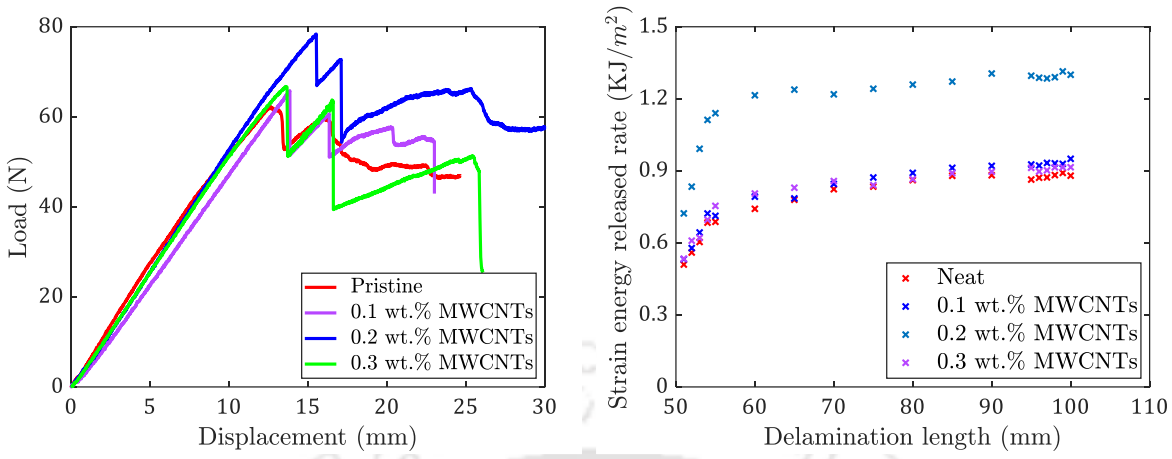

(a) (b)

Fig. 6.8 (a) Load-displacement response of CFRP under DCB test, and (b) Variation of SERR along the crack length

It is confirmed that for pristine CFRP laminate, the delamination occurs due to the tensile cracking of the matrix associated with the bridging of the carbon fiber. When the MWCNTs are added, a similar mechanism remains; however, an additional energy consumption mechanism is developed where the MWCNTs also bridge the interface of the crack tip and provide resistance to crack propagation. The experimentally obtained strength and energy parameters under mode I and mode II loading are listed in **Table 6.2**.

Table 6.2 Estimated CZM parameters from the experiments

MWCNTs Variations	Cohesive strength (MPa)		Fracture toughness (kJ/m^2)	
	Mode I	Mode II	Mode I	Mode II
Pristine	16.12	28.50	0.88	2.08
0.1 wt.% MWCNTs	18.23	31.62	0.95	2.34
0.2 wt.% MWCNTs	20.08	32.50	1.30	2.45
0.3 wt.% MWCNTs	17.63	31.08	0.92	2.15

6.3.3 Interlaminar shear stress (ILSS) studies

The representative load-displacement behaviour of the specimens subjected to the SBS test is shown in **Fig. 6.9 (a)**. A gradual increase in load with the displacement up to the peak load followed by a sudden drop represents an interlaminar shear failure of the specimens. The ILSS

of pristine and nanofiller-modified specimens are shown in **Fig. 6.9 (b)**. The average ILSS value of the pristine laminate is approximately 28.5 MPa, which increases up to 32.5 MPa for 0.2 wt. % of MWCNTs modified CFRP. The increase in the MWCNTs content results in improved fiber/matrix adhesion and effective stress transfer between epoxy and MWCNTs. However, it is noticed that an increase in MWCNT content proportionally increases the viscosity of the matrix, which results in poor wettability and poor fiber-matrix adhesion. Accordingly, a decrease in interlaminar shear stress is observed for CFRP reinforced with 0.3 wt.% of MWCNTs.

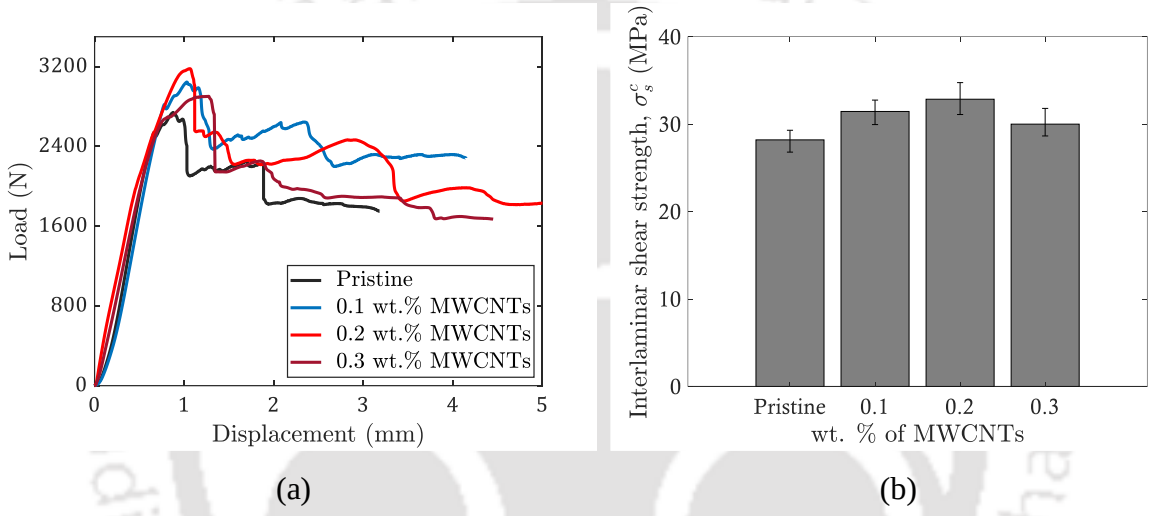

(a) (b)

Fig. 6.9 (a) Load-displacement response obtained from the SBS test, and (b) Variation of interlaminar shear stress for different MWCNTs variation

6.3.4 Mode II interlaminar fracture studies

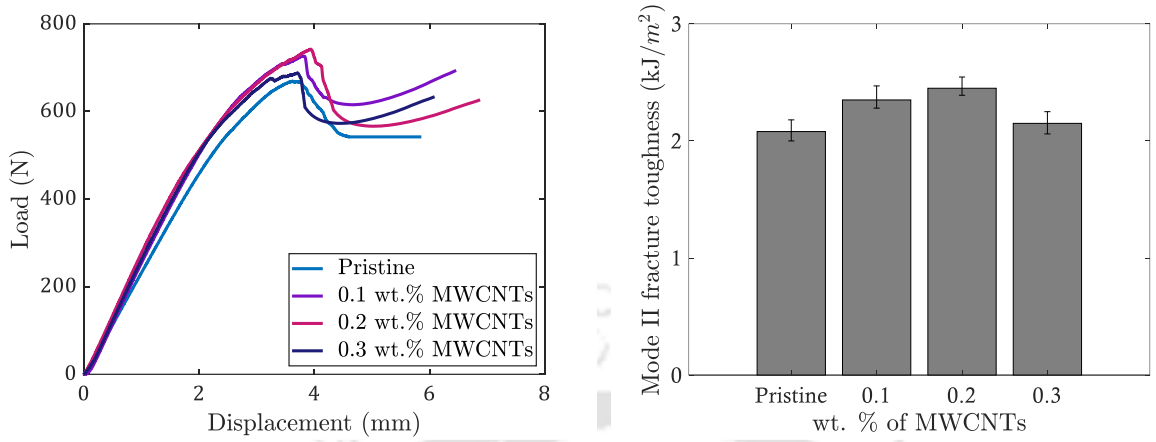

(a) (b)

Fig. 6.10 (a) Load-displacement response obtained from the ENF test, and (b) Mode II fracture toughness for different MWCNTs variation

The representative load-displacement response of pristine and MWCNTs reinforced specimens is shown in **Fig. 6.10 (a)**. The responses are initially linear and become non-linear before approaching their peak load. The average mode II fracture toughness value is 2.08, 2.34, 2.45, and 2.15 kJ/m^2 for pristine, 0.1, 0.2, and 0.3 wt.% of MWCNTs reinforced composites, respectively. The mode II fracture toughness of 0.2 wt.% of MWCNTs reinforced composite specimen is the highest, approximately 17.78% higher than pristine composites, as shown in **Fig. 6.10 (b)**. The fracture toughness of 0.3 wt.% of MWCNTs reinforced composite specimen is decreased compared to 0.2 wt.% of MWCNTs, possibly due to the agglomeration of MWCNTs into the epoxy resin [144].

6.3.5 Mixed-mode (I/II) interlaminar fracture studies

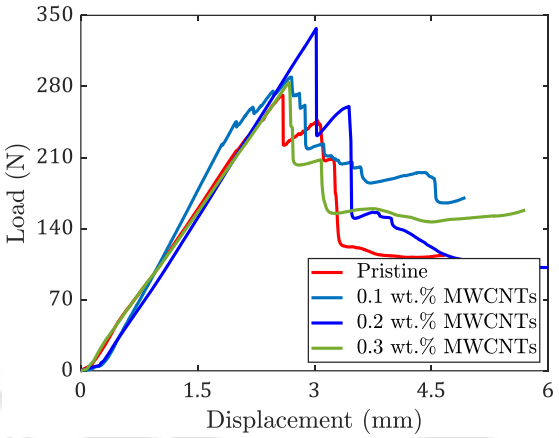

Fig. 6.11 Mixed-mode load-displacement response for lever length *c* =52 mm

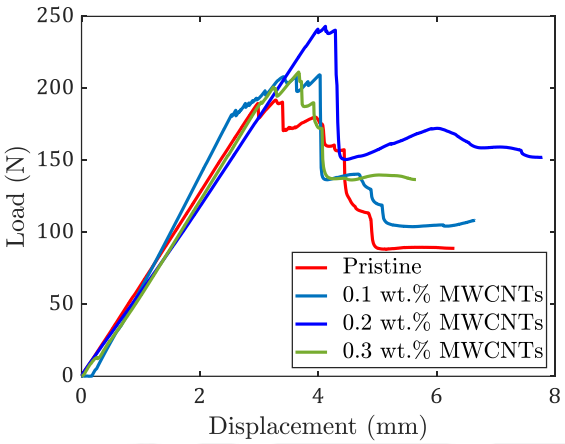

Fig. 6.12 Mixed-mode load-displacement response for lever length *c* =68 mm

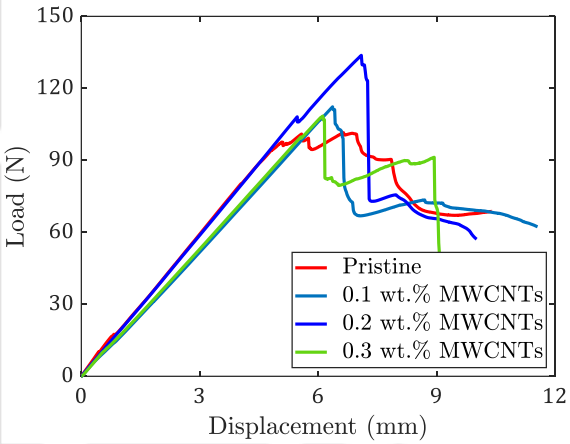

Fig. 6.13 Mixed-mode load-displacement response for lever length *c* =104 mm

The representative load-displacement responses from the MMB test are shown in **Fig. 6.11-Fig. 6.13**. The experiments are conducted for pristine and all MWCNTs variations, and their average responses are considered. Similar to the DCB and ENF test results, the 0.2 wt.% MWCNTs reinforced composites can sustain a more significant value of failure load under mixed-mode loading conditions irrespective of the mixed-mode ratios. The peak load reduces for 0.3 wt.% of MWCNTs reinforced composites, possibly due to the agglomeration of MWCNTs into the epoxy resin. Moreover, adding MWCNTs makes the interface brittle, as observed from the load-displacement response.

In addition to the dispersion of MWCNTs, the mixed-mode ratio also significantly influenced the interlaminar fracture toughness. The peak load corresponds to the lever length

of 52 mm, the highest compared to the other two lever lengths for pristine and all wt.% of MWCNTs reinforced composites. The decrease in lever length significantly increases the dominance of mode II loading, resulting in an increase in the peak load under load-displacement response.

6.4 Study of Surface Morphology

The fractured surfaces of the specimen are investigated to understand the influence of MWCNTs on the toughening mechanism. After conducting the mode II fracture tests, the specimens are cut into a dimension of 5 mm × 5 mm and placed under ZEISS, Gemini 300 FE-SEM. The detailed surface morphology under different loading modes is described in the subsequent subsection.

6.4.1 Study of mode I fracture surface

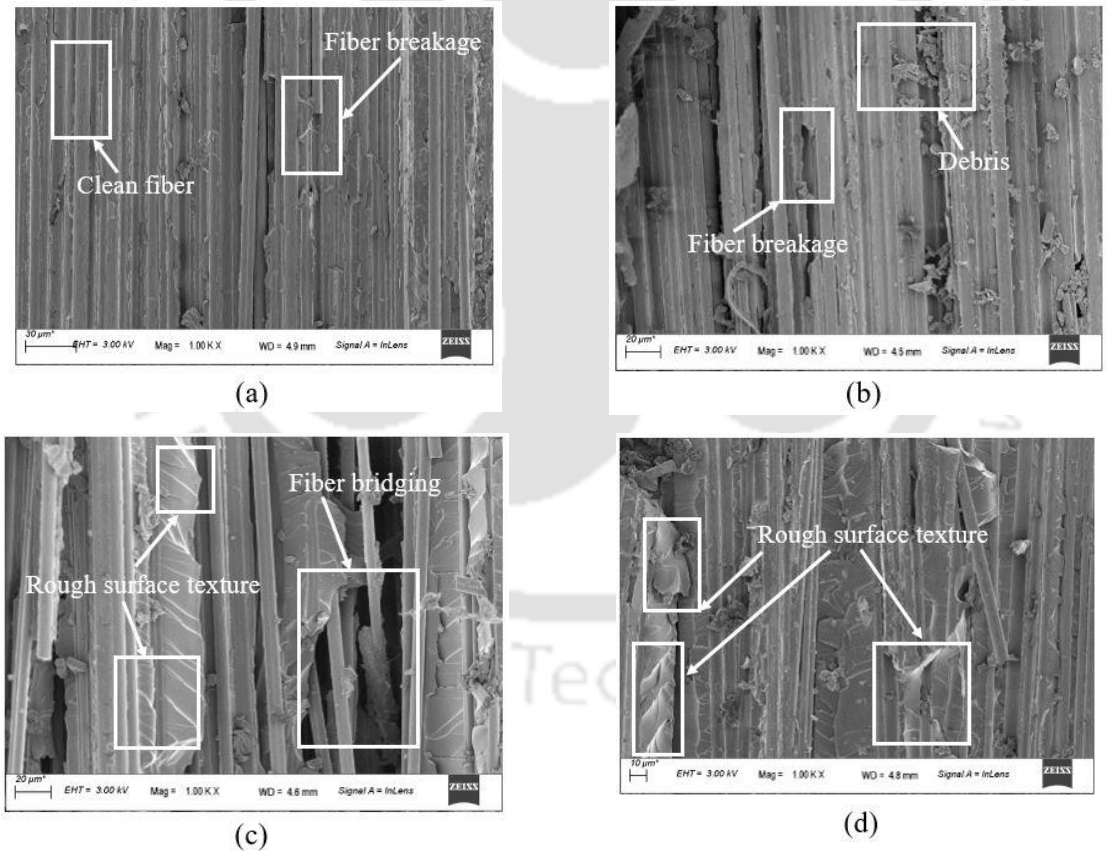

Fig. 6.14 Mode I fracture surfaces of (a) Pristine, (b) 0.1 wt.%, (c) 0.2 wt.%, and (c) 0.3 wt.% of MWCNTs-reinforced composites

The crack growth under pure mode I loading is prominently continuous along the fiber matrix interfaces. Clean fibers are observed in pristine fiber composites due to weak fiber-matrix adhesion, as shown in **Fig. 6.14 (a)**. Matrix debris is significant for composite specimens reinforced with 0.1 wt.% of MWCNTs, as shown in **Fig. 6.14 (b)**. Moreover, fiber bridging phenomena are observed in CFRP-reinforced with 0.2 wt.% of MWCNTs, as shown in **Fig. 6.14 (c)**. The fiber-bridging phenomenon usually occurs in the initial crack propagation stage, increasing mode I fracture toughness.

Rough surface texture is observed for MWCNTs reinforced composite specimens (specifically for 0.2 wt.% and 0.3 wt.%). Adding MWCNTs into the epoxy resin toughens the matrix and improves fiber-matrix adhesion. The stiffer epoxy will contribute to better resistance to crack propagation, leading to increased fracture toughness and rougher surface texture.

6.4.2 Study of mode II fracture surface

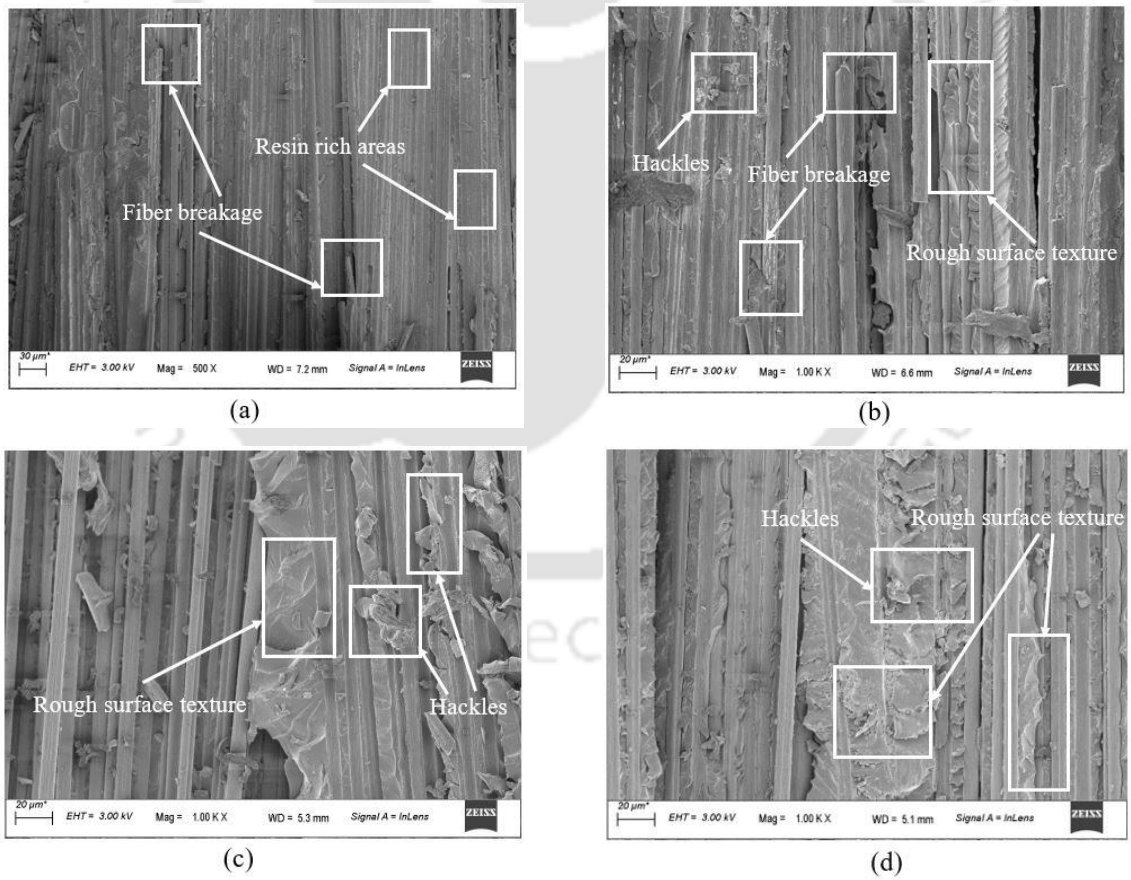

Fig. 6.15 Mode II fracture surfaces of (a) Pristine, (b) 0.1 wt.%, (c) 0.2 wt.%, and (c) 0.3 wt.% of MWCNTs-reinforced composites

The mode II fractured surfaces of the pristine specimens are relatively smooth and clean compared to the other MWCNTs-reinforced specimens, as shown in **Fig. 6.15 (a)**. In addition, several resin-rich areas and broken fibers are observed in the fracture surface of the pristine specimen observed under the microscope. On the other hand, the surface texture of the MWCNTs reinforced specimens is relatively rougher. The crack-deflecting mechanism in the presence of MWCNTs is mainly responsible for uneven surface morphology. A specific surface texture of the shear lip and saw-tooth hackles is observed in the fractured surface of the MWCNTs reinforced specimens. The hackles and the shear lip are prominent on the fractured surface with increasing contents on MWCNTs (prominently for 0.2 wt.% of MWCNTs content observed from **Fig. 6.15 (c)**). Furthermore, nanofillers in the epoxy resin repelled the matrix cracking by bridging mechanism, which requires a more considerable amount of energy for crack propagation. The MWCNTs reinforced specimens, therefore, exhibit a larger fracture toughness compared to pristine composite specimens.

The highly dense MWCNTs may result in agglomeration of MWCNTs in the reinforced composite specimens. Agglomeration reduces fiber/matrix adhesion and stress transfer between MWCNTs and matrix. This may be why the fracture toughness of 0.3 wt.% of MWCNTs specimens declined compared to the other MWCNTs reinforced specimens.

6.4.3 Study of mixed-mode (I/II) fracture surface

In mixed-mode loading, the presence of mode II contributes to the formation of hackles, as shown in **Fig. 6.16**. The crack growth pattern is primarily discontinuous, creating a rough surface texture. Clean fiber (for pristine composite specimens) represents a weak fiber matrix bonding that implies adhesive failure at the fiber-matrix interface. With the increasing content of MWCNTs (0.3 wt.%), the formation of hackles is less significant. Additionally, more matrix debris is observed for pristine and 0.1 wt.% MWCNTs reinforced tested coupons.

6.5 Closure

Specific fracture characterization tests are used to estimate the cohesive strength and interlaminar fracture toughness of MWCNTs reinforced CFRP. The mode I and mode II cohesive strength of the composite is evaluated using cross-tension and SBS test, respectively, for pristine and all wt.% variations of MWCNTs. The interlaminar fracture toughness of the composites is obtained by conducting the DCB and ENF test procedures. The mixed-mode (I/II)

fracture test of the CFRP is also carried out for three different mixed-mode ratios with a customized MMB setup.

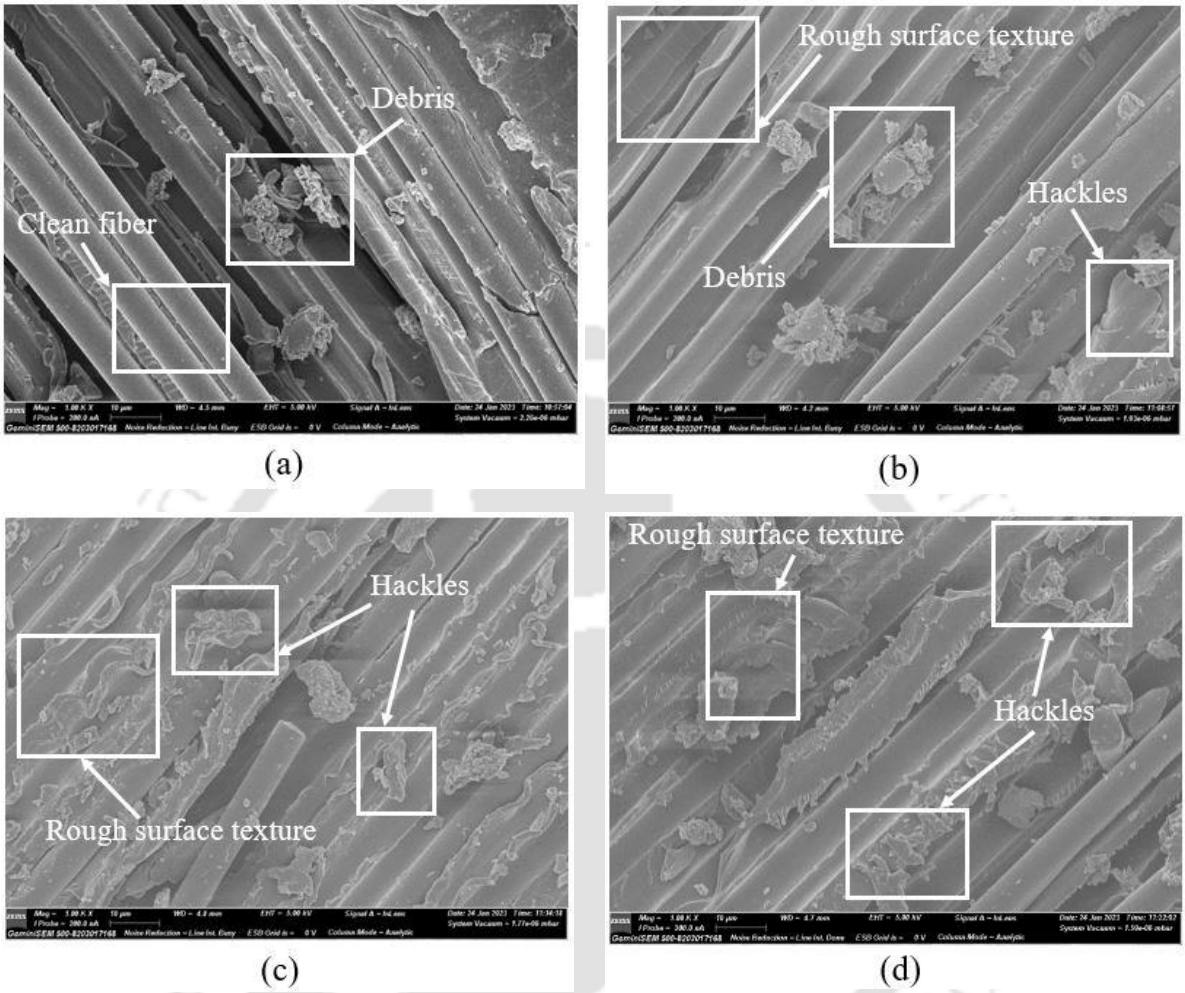

Fig. 6.16 Mixed-mode (I/II) fracture surfaces of (a) Pristine, (b) 0.1 wt.%, (c) 0.2 wt.%, and (c) 0.3 wt.% of MWCNTs-reinforced composites

The addition of MWCNTs up to 0.2 wt.% proportionally increases the strength and toughness properties. The interface strength and fracture toughness are decayed for CFRP reinforced with 0.3 wt.% of MWCNTs, possibly due to the agglomeration of the nanofillers into the epoxy resin. Moreover, the MWCNTs made the interface brittle, as observed from the load-displacement behaviour of the specimens observed under the DCB and the MMB tests. The FESEM analysis of the fracture surfaces confirmed the presence of hackles in MWCNTs reinforced composites, which may be a driving factor for enhancing fracture toughness.

Chapter 7 Numerical validation: Composite delamination

Triangular CZM is the commonly used T-S-L for predicting the delamination responses in composites, as it predicts reasonably well the experimental failure load and progressive delamination response [136]. This chapter presents a detailed formulation of the triangular CZM, specifically in the context of mixed-mode failure behaviour. The experimentally obtained cohesive strength and fracture energy in the preceding chapter is directly imputed into the triangular CZM to predict the interface failure behaviour of the laminated composites. A few parametric studies are also conducted to investigate the influence of the CZM parameters on the delamination response under pure mode I and mode II loading conditions.

It is essential to understand the delamination behaviour of the composites under mixed-mode loadings, which is more important in real-world scenarios. Numerous damage initiation such as — maximum stress, maximum strain, quadratic stress, quadratic strain, and damage evolution criteria — power law and B-K criteria are developed to study the composite delamination within the context of the CZM. In the present work, quadratic stress and power law criteria are used to combine the strength and energy parameters obtained experimentally under mode I and mode II loading conditions.

7.1 Triangular CZM

The triangular CZM is commonly employed to simulate delamination, the most prevalent failure mode in laminated composites. **Fig. 7.1 (a)** and **Fig. 7.1 (b)** illustrate the development of the cohesive zone with respect to the crack opening displacement or separation for the DCB and ENF test configurations, respectively. As the separation increases, the stress in the cohesive element approaches the cohesive strength and moves into the softening region of the T-S-L. The instantaneous traction-separation response for five different cohesive elements along the length of the cohesive zone for a triangular cohesive law is shown in **Fig. 7.1 (a)** and **Fig. 7.1 (b)** for mode I and mode II loading, respectively.

The constitutive response of the cohesive element on the onset of damage initiation can be given as

$$\sigma_i = K_i \delta_i \tag{7.1}$$

where $i = n$ or s are used to represent the cohesive stress, stiffness, and separation of the cohesive zone under mode I and mode II loading conditions, respectively. Once the damage gets initiated, the stiffness of the interface decreases from K_i to $(1-d)K_i$. The damage variable d of the cohesive element is assumed to be zero till the onset of damage initiation corresponding to the cohesive layer separation δ_n^c (or δ_s^c) and it approaches a value of one as it reaches the critical final separation δ_n^f (or δ_s^f). Here δ_n^c or δ_s^c represents the mode I and mode II cohesive separation, respectively, corresponding to the peak cohesive traction. Accordingly, the cohesive traction approaches zero once the cohesive separation becomes δ_n^f or δ_s^f under mode I and mode II loading, respectively. The instantaneous cohesive stress during damage evolution can be represented as

$$\sigma_i = (1-d)K_i\delta_i$$
$$d = \frac{\delta_i^f(\delta_i - \delta_i^c)}{\delta_i(\delta_i^f - \delta_i^c)}, \qquad d \in [0,1] \tag{7.2}$$

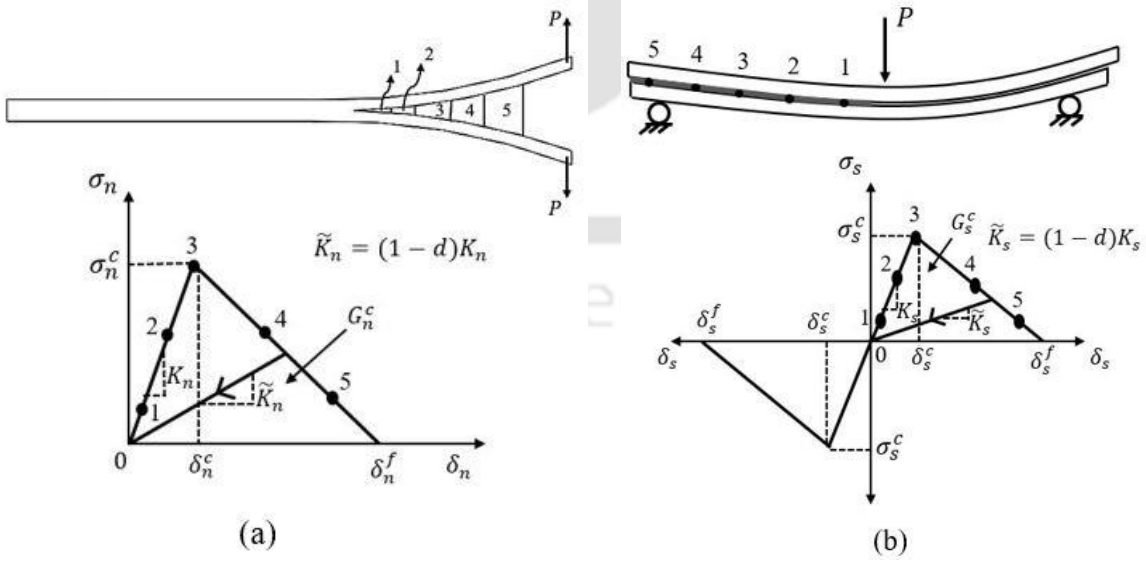

Fig. 7.1 Triangular CZM for (a) Mode I, and (b) Mode II loading.

7.1.1 Overview of mixed-mode triangular CZM

To describe combined mode I and mode II failure behaviour, a three-dimensional representation, employing the $0-\sigma-\delta_{normal}$ (normal) and $0-\sigma-\delta_{shear}$ (shear) planes is shown in **Fig. 7.2**. The triangles $0-\sigma_n^c-\delta_n^f$ and $0-\sigma_s^c-\delta_s^f$ are used to represent mode I and mode II triangular cohesive responses, respectively. Any point on the $0-\delta_n^f-\delta_s^f$ represents the mixed-mode relative displacement.

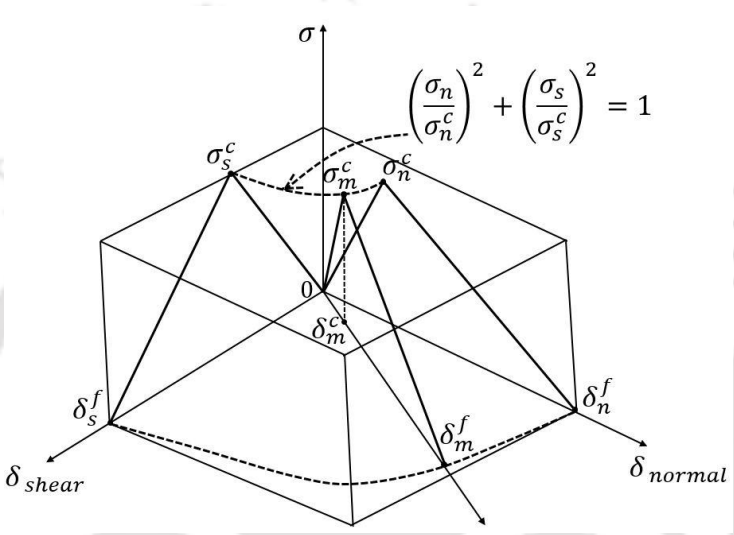

Fig. 7.2 Mixed-mode (I/II) triangular CZM

Here δ_n and δ_s are the instantaneous separation under mode I and mode II loading conditions. The instantaneous mixed-mode relative displacement is defined as

$$\delta_m=\sqrt{\delta_n^2+\delta_s^2} \tag{7.3}$$

The quadratic stress criteria used for damage initiation is defined as

$$\left(\frac{\sigma_n}{\sigma_n^c}\right)^2+\left(\frac{\sigma_s}{\sigma_s^c}\right)^2=1 \tag{7.4}$$

where σ_n and σ_s represents the instantaneous normal and shear stresses in the first shear direction, respectively. σ_n^c and σ_s^c are the normal and shear strengths in the respective directions. In the present work, a power law [145] is used for damage evolution under mixed-mode loading conditions, which is given as

$$\left(\frac{G_n}{G_n^c}\right)^{\alpha}+\left(\frac{G_s}{G_s^c}\right)^{\gamma}=1 \tag{7.5}$$

where G_n and G_s are the instantaneous fracture energy under mode I and mode II loading, respectively. G_n^c and G_s^c are the critical fracture energy in the respective loading conditions. α and γ are the exponents used to define the damage evolution.

The experimentally obtained cohesive strength and fracture energy are imputed into the triangular T-S-L to predict the failure response of the CFRP reinforced with the MWCNTs under different loading conditions. Several parametric studies are also carried out to investigate the influence of the CZM parameters on the global load-displacement response. The composite laminate is modelled as an orthotropic material with nine independent elastic constants. All the material properties are evaluated using the rule of mixture and the EasyPBC plugin [146] in ABAQUS®.

7.2 Evaluation of the effective properties of the nanocomposites

Computational modelling is an efficient tool to estimate the effective properties of the MWCNTs reinforced composite laminate with intricate morphologies. Various methods, including the rule of mixture [147] and the strength of materials [148] concept, can be employed to predict the overall properties of the composite laminate. Another effective approach is the homogenization technique [149], which utilizes the FE tool to convert heterogeneous media into an equivalent continuous homogeneous medium.

In the present work, a two-step methodology is adopted to evaluate the effective properties of the composite. Initially, the rule of mixtures is used to compute the equivalent properties of epoxy nanocomposites. If ρ_r denotes the density ratio between the hydroxyl functionalized MWCNTs and epoxy, the volume fraction of CNTs corresponding to a particular weight percentage can be derived as follows [150]

$$v_{cnt} = \left(\frac{\rho_r}{w_{cnt}} - \rho_r + 1\right)^{-1} \tag{7.6}$$

where w_{cnt} is the weight fraction of CNTs. The effective modulus of epoxy-based nanocomposite is calculated using the rule of mixtures using the formula

$$E_{nc} = E_m v_m + E_{cnt} v_{cnt} \tag{7.7}$$

where E_m, $v_{m,}$ and E_{cnt}, v_{cnt} represent the Young's modulus and the volume fraction of resin and the MWCNTs, respectively.

Next, a representative volume element (RVE) is considered, and the homogenization technique is used to compute the effective properties of the nanocomposites with reinforced fibers. Because of the recurring patterns within the composites, the RVE shown in **Fig. 7.3** is appropriate. The homogenization technique is employed through periodic boundary conditions (PBCs).

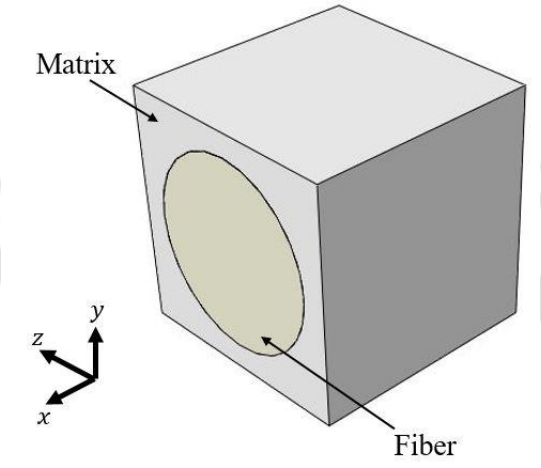

Fig. 7.3 Representative volume element (RVE)

As the RVEs can be assembled to form the complete lamina, the displacement should be continuous at the boundary of the neighboring RVE. So, the traction distribution at the opposite parallel faces of RVE should be equal and opposite. The displacement field of the pair of opposing parallel faces can be represented by the following set of equations [151].

$$u_i^{j+} = \epsilon_{ik} x_k^{j+} + u_i^*$$
$$u_i^{j-} = \epsilon_{ik} x_k^{j-} + u_i^* \tag{7.8}$$

where ϵ_{ik} is the global strain tensor of the periodic structure, and u^* is the periodic function from one RVE to another. k^+ and k^- represents k^{th} pair opposite parallel boundary surfaces of the RVE. The periodic component of the displacement field, u^* is the same for the opposite faces of RVE, which leads to

$$u_i^{j+} - u_i^{j-} = \epsilon_{ik}\left(x_k^{j+} - x_k^{j-}\right) = \epsilon_{ik}\Delta x_k^j \tag{7.9}$$

Eq. (7.9) is known as the displacement difference periodic boundary conditions (PBCs), which can be applied as displacement constraints on the boundary nodes of the surface. These boundary conditions satisfy both displacement and traction continuity conditions. To determine the average stress ($\bar{\bar{\sigma}}_{ij}$) and strain ($\bar{\bar{\epsilon}}_{ij}$) in the RVE, we use

$$\bar{\bar{\sigma}}_{ij} = \frac{1}{V_{RVE}} \int_{V_{RVE}} \sigma_{ij}(x,y,z)\mathrm{d}v$$
$$\bar{\bar{\epsilon}}_{ij} = \frac{1}{V_{RVE}} \int_{V_{RVE}} \epsilon_{ij}(x,y,z)\mathrm{d}v \quad (7.10)$$

Here V_{RVE} represents the volume of the RVE. The above two equations ensured the equivalency of strain energy between the original and the equivalent RVEs. Therefore, the strain energy of the original heterogeneous RVE (U^*) and the strain energy in the homogenous RVE (U) can be given as

$$U^* = \frac{1}{2} \int_{V_{RVE}} \sigma_{ij}\epsilon_{ij}\mathrm{d}v$$
$$U = \frac{1}{2} \bar{\bar{\sigma}}_{ij}\bar{\bar{\epsilon}}_{ij}V_{RVE} \quad (7.11)$$

Finally, the specific stiffness modulus $\bar{\bar{\bar{\bar{C}}}}_{ijkl}$ is obtained from the calculated average stress and strain from Eq. (7.10). The specific stiffness modulus can be given as

$$\bar{\bar{\sigma}}_{ij} = \bar{\bar{\bar{\bar{C}}}}_{ijkl}\bar{\bar{\epsilon}}_{lk} \quad (7.12)$$

In numerical analysis, the stresses and strains are initially evaluated for each element, and the weighted average is taken over all elements. The acquired values are divided by the volume of the RVE to obtain the average stresses and strains.

Table 7.1 Material properties for multiscale composites with all variations of MWCNTs

wt. % MWCNTs	E_{xx} (GPa)	$E_{yy} = E_{zz}$(GPa)	$\nu_{xy} = \nu_{xz}$	ν_{yz}	$G_{xy} = G_{xz}$ (GPa)	G_{yz}(GPa)
Neat	116.423	11.243	0.2414	0.2597	3.883	2.810
0.1%	116.537	11.947	0.2414	0.2598	4.130	2.992
0.2%	116.652	12.652	0.2414	0.2598	4.377	3.175
0.3%	116.766	13.348	0.2414	0.2599	4.622	3.357

A cylindrical fiber with a fiber-to-matrix volume fraction V_f = 50% is considered inside a cubical RVE. The required volume faction is decided by dividing the required weight proportion of fiber and matrix by their respective densities. An ABAQUS® plugin named

EasyPBC [146] is used to evaluate the effective orthotropic properties for the given V_f of the samples. The equivalent effective composite properties are mentioned in **Table 7.1**.

7.3 Numerical Modelling: Mode I delamination

The specimen geometry is modelled numerically in the FE software ABAQUS®. To simulate the load application, a vertical displacement u_y is applied at the end node situated at the upper half of the cantilever beam. Another equivalent node on the bottom part of the cantilever beam is provided with hinged support, as shown in **Fig. 7.4**. The hinged boundary condition allows the free rotation of the beam, preventing the mode II delamination and interlaminar shear stress at the interface. Both the top and the bottom edge node is tied to the top and bottom surface of the cantilever up to a distance of 20 mm from the left edge of the beam using a beam-type MPC constraint.

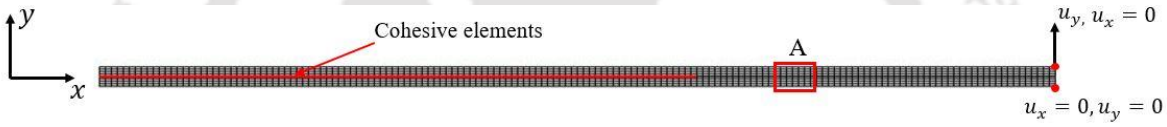

Fig. 7.4 Model geometry and boundary conditions of DCB

7.3.1 Mess-convergence study

In order to simulate the delamination phenomena accurately, the mesh should be sufficiently fine in the cohesive zone ahead of the crack tip. However, an extremely fine mesh may be computationally intensive for large structures. Therefore, a mesh sensitivity analysis is required to obtain the minimum number of elements required for a reliable result.

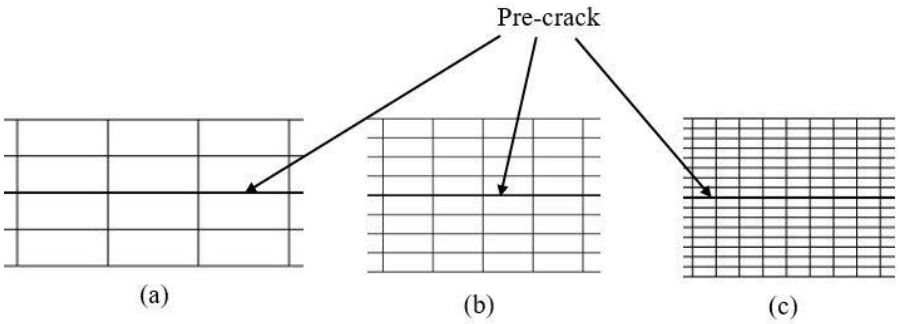

Fig. 7.5 Mesh configurations used for the DCB analysis

Each part of the cantilever beam is modelled with 4-noded bilinear plane stress quadrilateral elements (CPS4). Two-dimensional 4-noded cohesive elements (COH2D4) are positioned along the interface of the cantilever beam, as shown in **Fig. 7.4**. Three different mesh geometries

with 420, 1380, and 5220 total elements are considered for the mesh-sensitivity analysis. As shown in **Fig. 7.5**, the mesh configuration is the magnified meshed geometry of the region 'A' shown in the DCB geometry in **Fig. 7.4**. The load-displacement response obtained for the pristine composite for all three mesh configurations is shown in **Fig. 7.6**. Based on the mesh convergence analysis, 1340 total elements are considered for mode I crack propagation analysis.

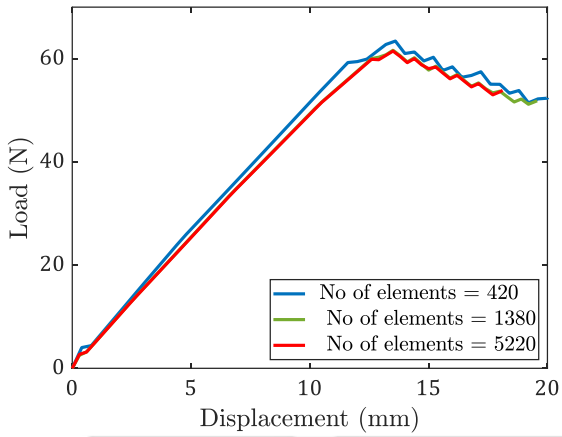

Fig. 7.6 DCB mesh convergence study

7.3.2 Parametric analysis

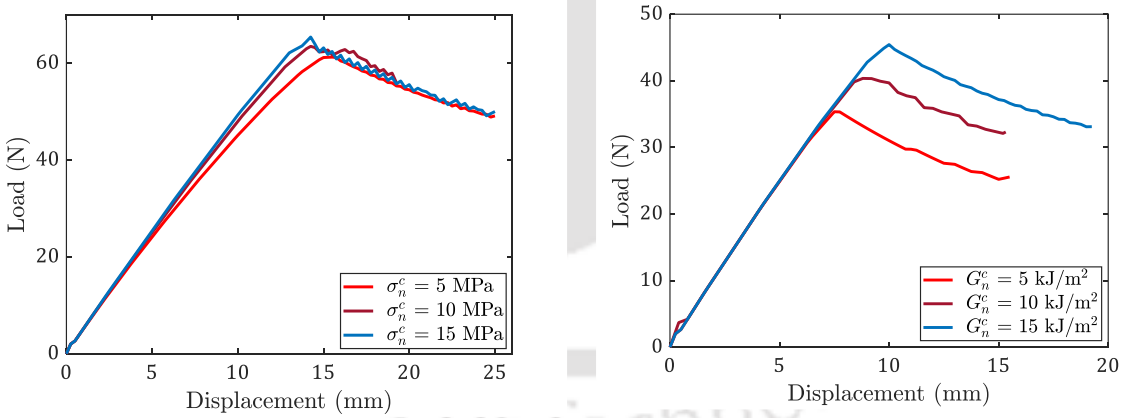

(a) (b)

Fig. 7.7 Influence of (a) Cohesive strength, and (b) fracture energy on the load-displacement response of DCB

The load-displacement response is significantly affected by the variations in the CZM parameters. The parametric analysis involves three distinct sets of cohesive strength and fracture energy variations to investigate the delamination behaviour of the composite materials.

The cohesive strength plays a significant role in accessing the delamination behaviour of composites. The cohesive strength defines the damage initiation stress at which the delamination initiates within the composite material. A higher cohesive strength necessitates a more significant amount of energy for damage initiation, which, in turn, enhances the load-bearing capacity of the structures. **Fig. 7.7 (a)** shows the influence of cohesive strength on the global load-displacement behaviour with a constant cohesive fracture energy $G_n^c = 0.5$ kJ/m^2. The cohesive strength also subsequently influences the propagation of the delamination front. A higher value of the cohesive strength means the delamination will progress slowly, as it requires greater stress to propagate through the material.

The cohesive fracture energy is another important parameter representing the energy required to initiate delamination within the composites. A relatively more significant value of the fracture energy indicates more resistance to fracture and vice versa. Moreover, a larger fracture energy value represents that the crack will propagate more slowly, resulting in greater resistance to crack propagation. Three different fracture energy variations are considered for a constant value of cohesive strength $\sigma_n^c = 5$ MPa and their load-displacement responses are plotted, as shown in **Fig. 7.7 (b)**.

7.3.3 Numerical validation

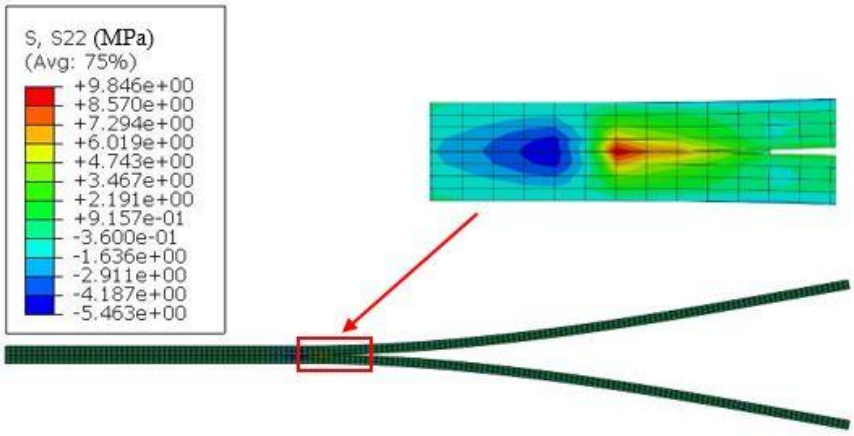

Fig. 7.8 Deformed geometry (DCB)

The numerical simulations are carried out for the pristine and all other variations of the MWCNTs. The experimentally obtained CZM parameters for each variation of the MWCNTs are used in the numerical model. The deformed FE model for the pristine composite laminate is shown in **Fig. 7.8.** The numerical results are in close agreement with the

experimental observations of pristine and all wt.% of MWCNTs, as shown in **Fig. 7.9 (a)-Fig. 7.9 (d)**. The % error between the experimental and the numerical peak load is mentioned in **Table 7.2**.

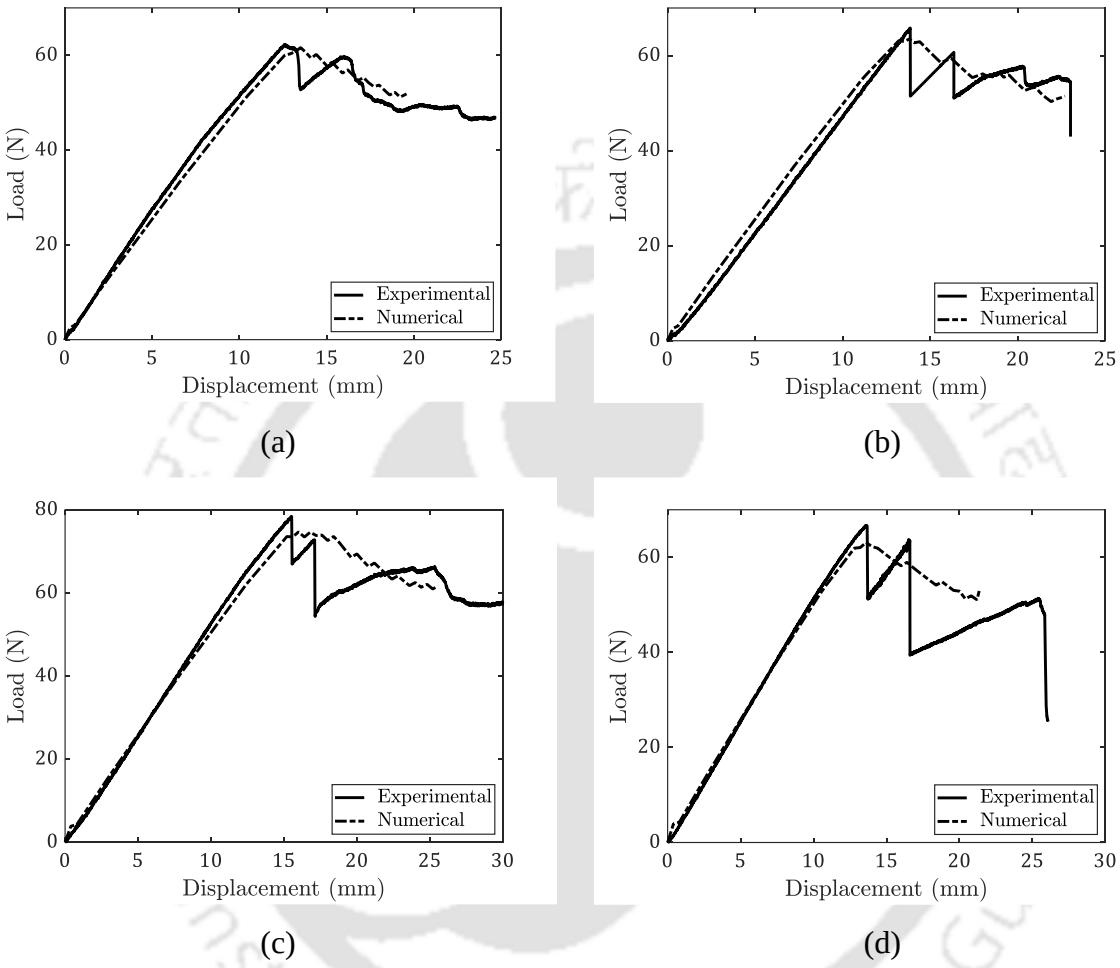

Fig. 7.9 Numerical validation (a) Pristine, (b) 0.1 wt.%, (c) 0.2 wt.%, and (d) 0.3 wt.% of MWCNTs

Table 7.2 Difference between the experimental and numerical peak load (DCB)

wt. % of MWCNTs	Experimental peak load (N) (P_{exp})	Numerical peak load (N) (P_{num})	% Error $\left\|\frac{P_{exp} - P_{num}}{P_{exp}}\right\|$
Pristine	62.33	61.67	1.05%
0.1%	65.80	63.19	3.96%
0.2%	78.38	75.95	3.10%
0.3%	66.74	63.43	4.96%

7.4 Numerical Modelling: Mode II delamination

A 2-D deformable solid part is created for each half of the ENF specimens. For generating a pre-crack to initiate the delamination, no contact interaction is provided for the initial length of 50 mm along the bonded surface of the laminate. The 4-nodded 2D cohesive elements are inserted ahead of the pre-crack region in the mid-surface of the composite laminate, as shown in **Fig. 7.10**. The specimen geometry is positioned with a span length of 100 mm between two fixed roller supports, while the top roller is subjected to a downward displacement of 7 mm.

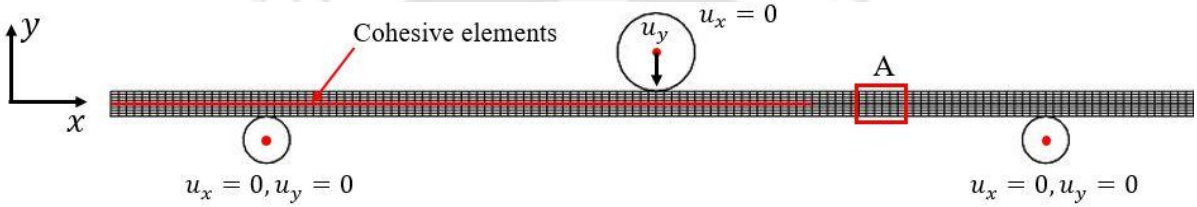

Fig. 7.10 Model geometry and the boundary conditions of ENF

A mesh-convergence analysis is performed for three different mesh. The mesh configurations are shown in **Fig. 7.11**, and their load-displacement response is recorded. This configuration is the magnified meshed geometry of the region 'A' shown in the ENF geometry (**Fig. 7.10**). From the load-displacement response, as shown in **Fig. 7.12**, the optimum number of elements considered for the present study is 1658, which includes 1120 linear plane stress quadrilateral elements (CPS4) for each half of the laminated beam, 90 2-D cohesive elements (COH2D4), and 66 linear line elements for the three rigid roller support.

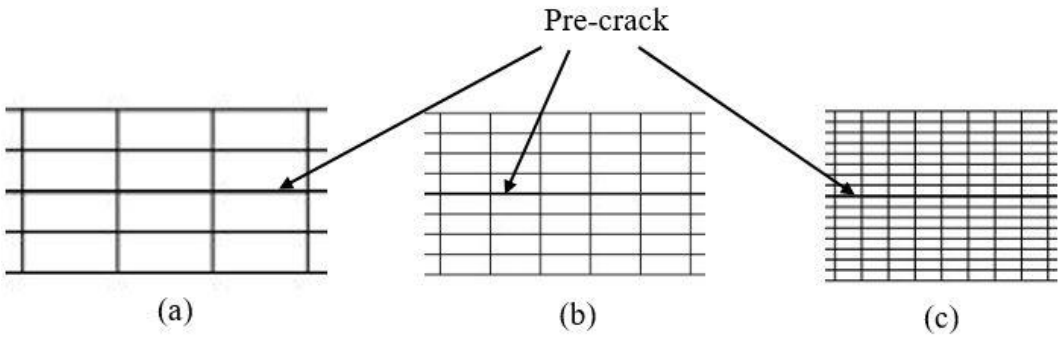

Fig. 7.11 Mesh configurations used for the ENF analysis

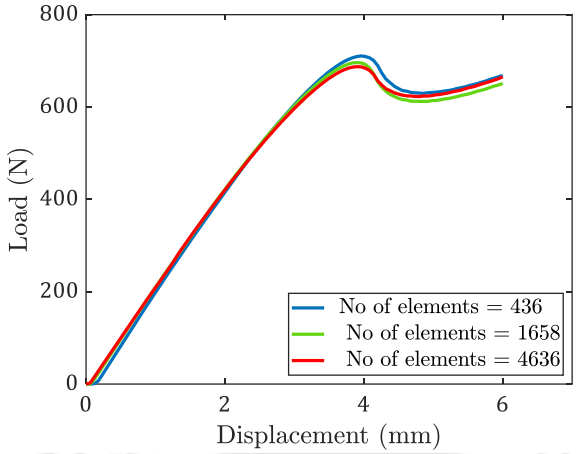

Fig. 7.12 ENF mesh convergence study

7.4.1 Parametric analysis

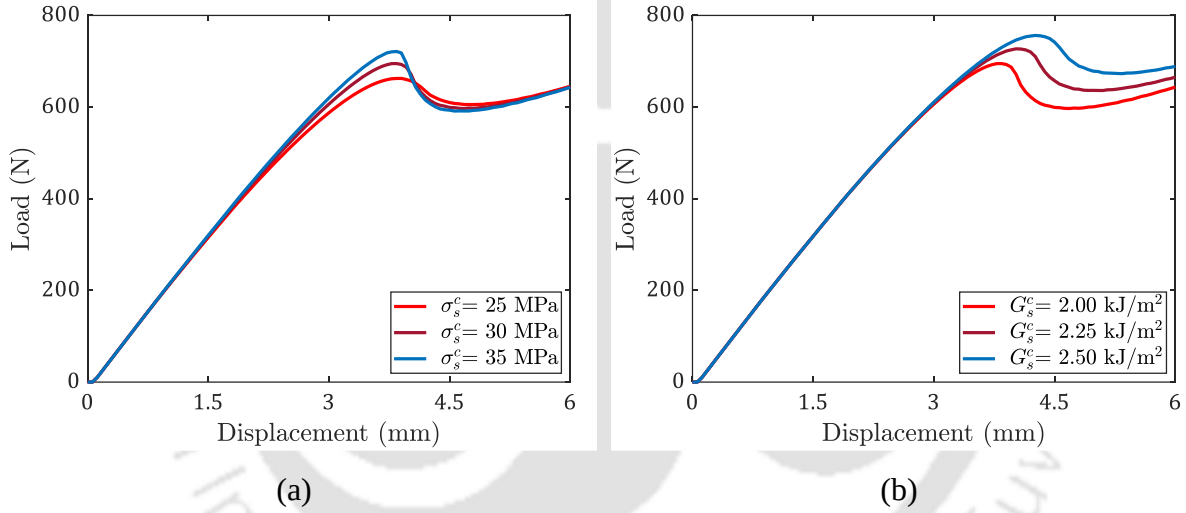

Fig. 7.13 Influence of (a) Cohesive strength and (b) fracture energy on the load-displacement response of ENF

The parametric analysis is performed with different cohesive strengths and fracture energies. For the pristine composites, the influence of the cohesive strength on the delamination response is investigated for a constant value of the cohesive fracture energy with $G_s^c = 2$ kJ/m^2. It is observed from **Fig. 7.13 (a)** that an increase in cohesive strength for a fixed fracture energy increases the peak load under the load-displacement response. Additionally, the increased value of the cohesive strength enhances the brittleness of the interface.

The failure behaviour is further investigated under three different variations of fracture energy for a constant value of the cohesive strength with $\sigma_s^c = 30$ MPa. The increase in the

fracture energy proportionally increases the load-bearing ability and the ductility of the interfaces, as shown in **Fig. 7.13 (b)**.

7.4.2 Numerical validation

The FE simulations are carried out for the pristine and all the wt.% of MWCNTs. The deformed FE model for the ENF specimens is shown in **Fig. 7.14**. It is observed that the load-displacement response of the numerical model for the pristine and all other variations of the MWCNTs are in close agreement with the experimental results. The combined numerical and the experimental load-displacement response of the pristine and all the other MWCNTs variations are shown in **Fig. 7.15**. The % error between the experimental and the numerical peak load is mentioned in

Table 7.3.

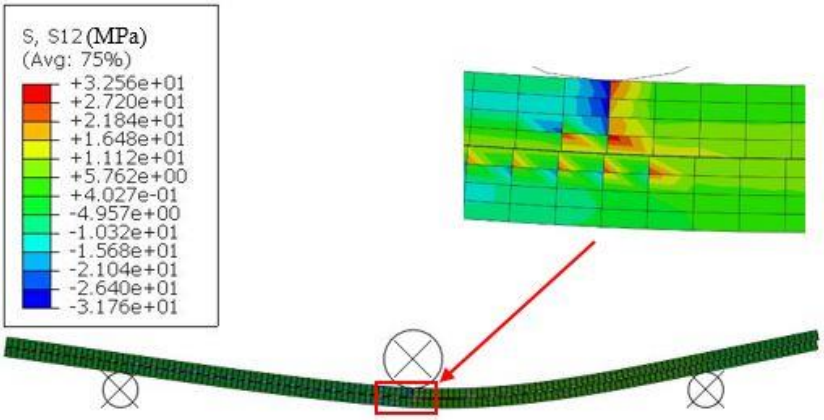

Fig. 7.14 Deformed geometry (ENF)

Table 7.3 Difference between the experimental and numerical peak load (ENF)

wt. % of MWCNTs	Experimental peak load (N) (P_{exp})	Numerical peak load (N) (P_{num})	% Error $\left\|\frac{P_{exp} - P_{num}}{P_{exp}}\right\|$
Pristine	701.10	717.04	3.01%
0.1%	748.04	767.35	2.58%
0.2%	756.46	771.17	1.98%
0.3%	708.32	726.47	2.57%

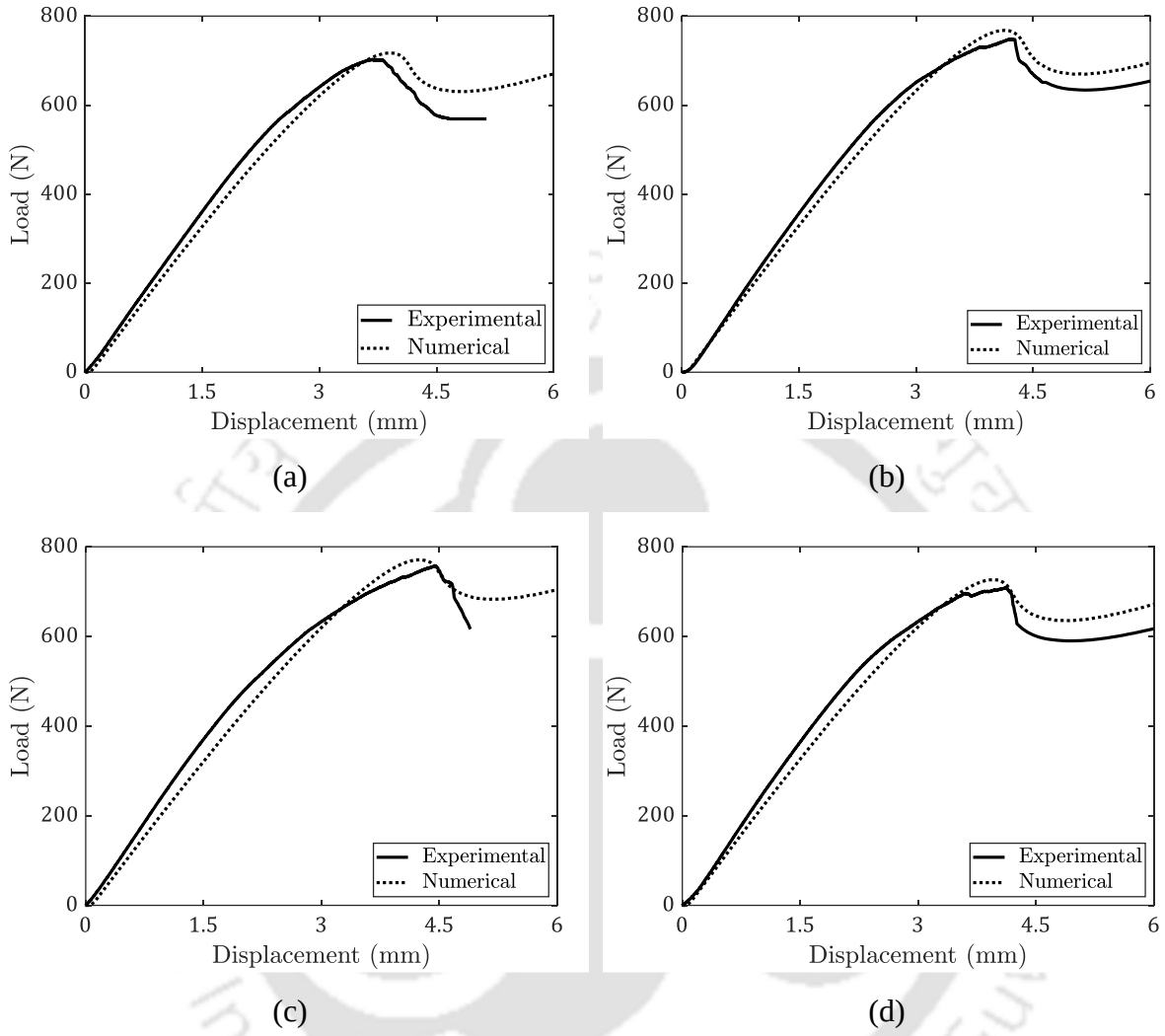

Fig. 7.15 Numerical validation (a) Pristine, (b) 0.1 wt.%, (c) 0.2 wt.%, and (d) 0.3 wt.% of MWCNTs

7.5 Numerical Modelling: Mixed-mode (I/II) delamination

The MMB setup consists of four parts: the composite laminate, cohesive, the support roller, and the lever for applying the load. Each half of the composite beam is modelled with 2-D plane stress quadrilateral elements and 2-D cohesive elements along the interface. Moreover, the lever and the roller are modelled as 2-D discrete rigid parts without deformation during loading.

A downward displacement u_y is applied to the reference point of the lever, as shown in **Fig. 7.16**. The reference point of the roller is fixed to eliminate all degrees of translation and rotational motion. The reference point, situated at the right corner of the bottom laminate, is

provided with hinged boundary conditions. Additionally, the top and the bottom edge node, situated at the right end of each half of the cantilever, is tied to the composite surface up to a distance of 25 mm from the using a beam-type MPC constraint. A pair of contact interactions is provided between the top surface of the laminate with the lever and the bottom surface of the laminate with the roller to avoid interpenetration.

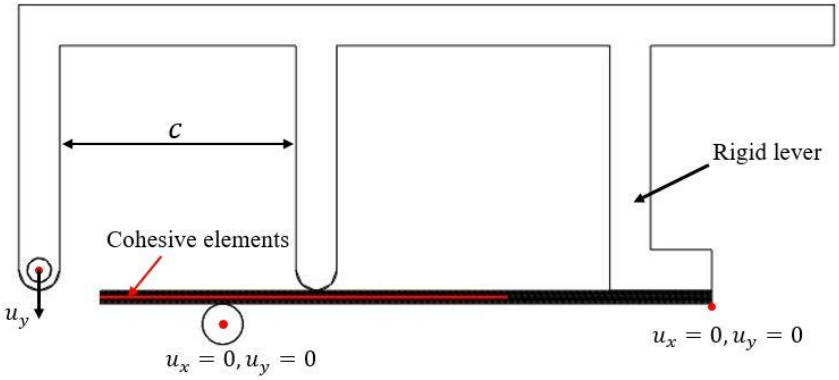

Fig. 7.16 Model geometry and the boundary conditions of ENF

The total number of elements in MMB meshed geometry is 4455, which consists of 1500 CPS4 elements on each half of the composite beam with 250 2-D interface cohesive elements. The optimum number of elements required to perform the simulation is based on the convergence analysis.

7.5.1 Numerical validation

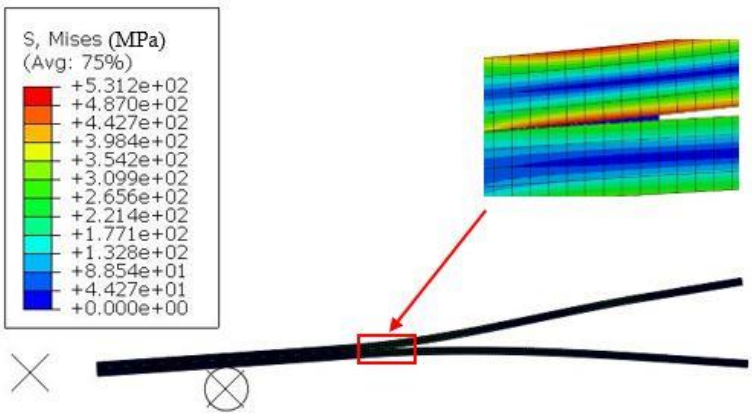

Fig. 7.17 Deformed geometry (MMB)

The FE simulations are carried out for the pristine and all the wt. % of MWCNTs. For lever length $c = 68$ mm, the deformed FE model of the MMB specimen is shown in **Error! Reference source not found.** As Eq. (7.4) mentioned, the quadratic stress criteria is used to

predict damage initiation under mixed-mode. Moreover, the damage evolution is governed by the power law with exponent $\alpha = \gamma = 1$, which is popular choice for many researchers [152–154].

Table 7.4 Difference between the experimental and numerical peak load (MMB)

wt. % of MWCNTs	Lever length (c) in mm	Mixed-mode ratio G_s/G	Experimental peak load (N) (P_{exp})	Numerical peak load (N) (P_{num})	% Error $\left\|\frac{P_{exp} - P_{num}}{P_{exp}}\right\|$
Pristine	52	0.4	271.64	267.25	1.61%
	68	0.3	191.90	197.50	2.92%
	104	0.2	101.52	102.14	0.61%
0.1%	52	0.4	289.17	280.36	3.04%
	68	0.3	209.26	206.40	1.36%
	104	0.2	112.31	107.14	4.60%
0.2%	52	0.4	337.06	326.88	3.02%
	68	0.3	243.06	242.38	0.28%
	104	0.2	133.76	126.08	5.74%
0.3%	52	0.4	283.89	269.81	4.96%
	68	0.3	211.35	204.90	3.05%
	104	0.2	108.44	105.38	2.82%

It is observed that the load-displacement response of the numerical model for the pristine and all the other variations of MWCNTs are in close agreement with the experimental results, as shown in **Fig. 7.18**-**Fig. 7.20**. The % error between the experimental and the numerical peak load for all three lever length is mentioned in **Table 7.4**.

7.6 Discussions

The FE modelling provides a detailed understanding of the influence of the MWCNTs on the interlaminar fracture toughness. The experimentally obtained strength and energy parameters are used in all three numerical models (i.e., DCB, ENF, and MMB) to validate their delamination responses. The main advantage of this method is that the damage experienced by

each variation of the MWCNTs can be evaluated and displayed separately, allowing the distinction between different failure scenarios.

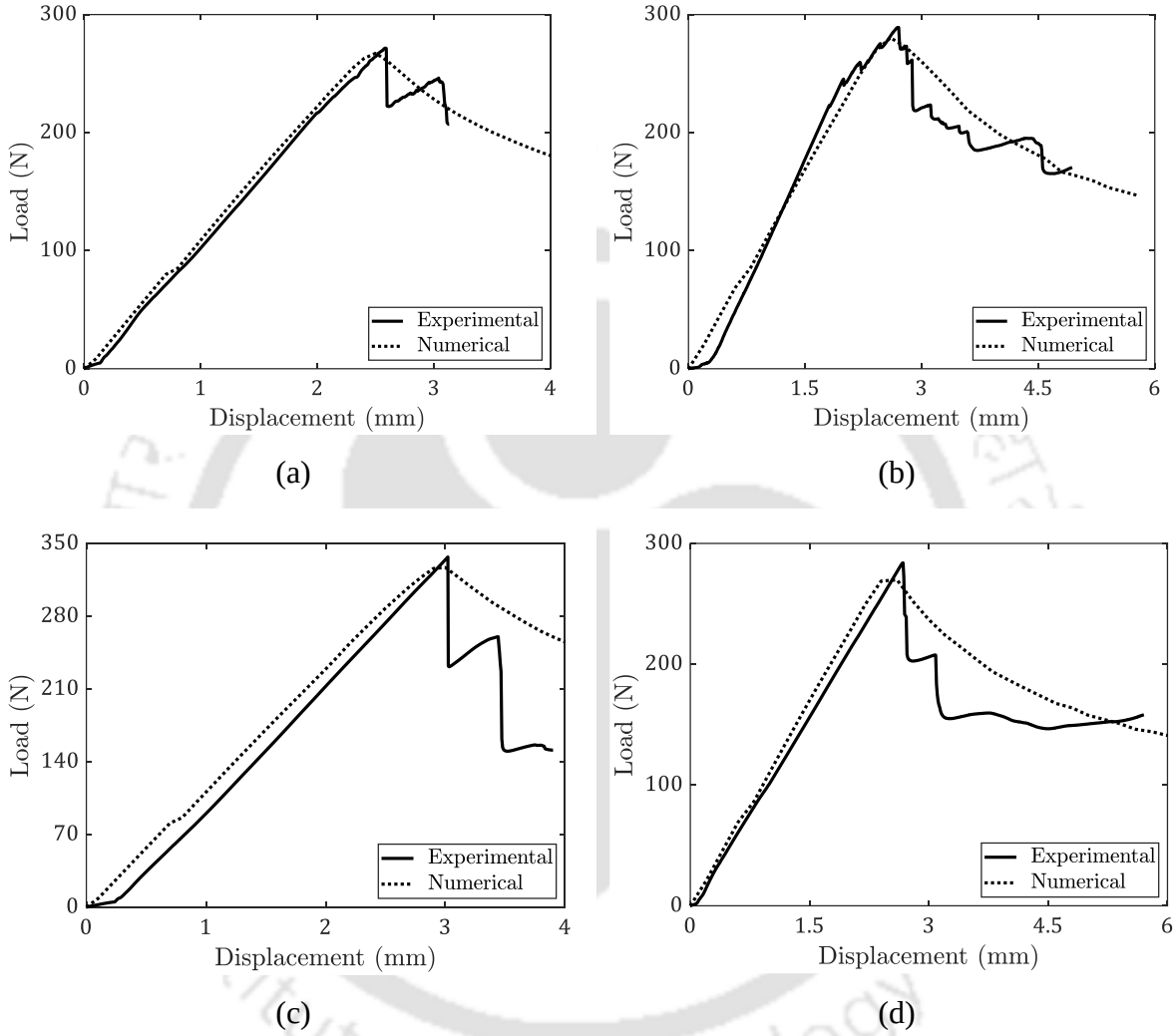

Fig. 7.18 Numerical validation with lever length c =52 mm for (a) Pristine, (b) 0.1 wt.%, (c) 0.2 wt.%, and (d) 0.3 wt.% of MWCNTs

The numerical validation shows that although the FE results generally align well with the experimental load-displacement responses, some disparities arise, particularly during the crack growth phase. One possible explanation for these differences is using a constant critical energy release rate in the numerical simulation despite the fracture energy changes as delamination advances. The modified beam theory employed to estimate mode I fracture energy assumes a linear relationship between the cube root of compliance and crack length. This holds true only

when a constant fracture energy value is assumed during crack propagation. In fiber bridging cases, the experimental data points form a curved trajectory, rendering a linear fitting method inadequate for determining corrected fracture energy values. However, the FE modelling offers valuable insights for visualizing the influence of the MWCNTs on the interlaminar fracture toughness. The standard ASTM standard testing procedures are used to estimate the fracture parameters, which adhere to the traditional LEFM theories. Alternatively, other fracture mechanics theories, such as EPFM, might be suitable for effectively validating the nonlinear failure behaviour of the laminated composites reinforced with the MWCNTs.

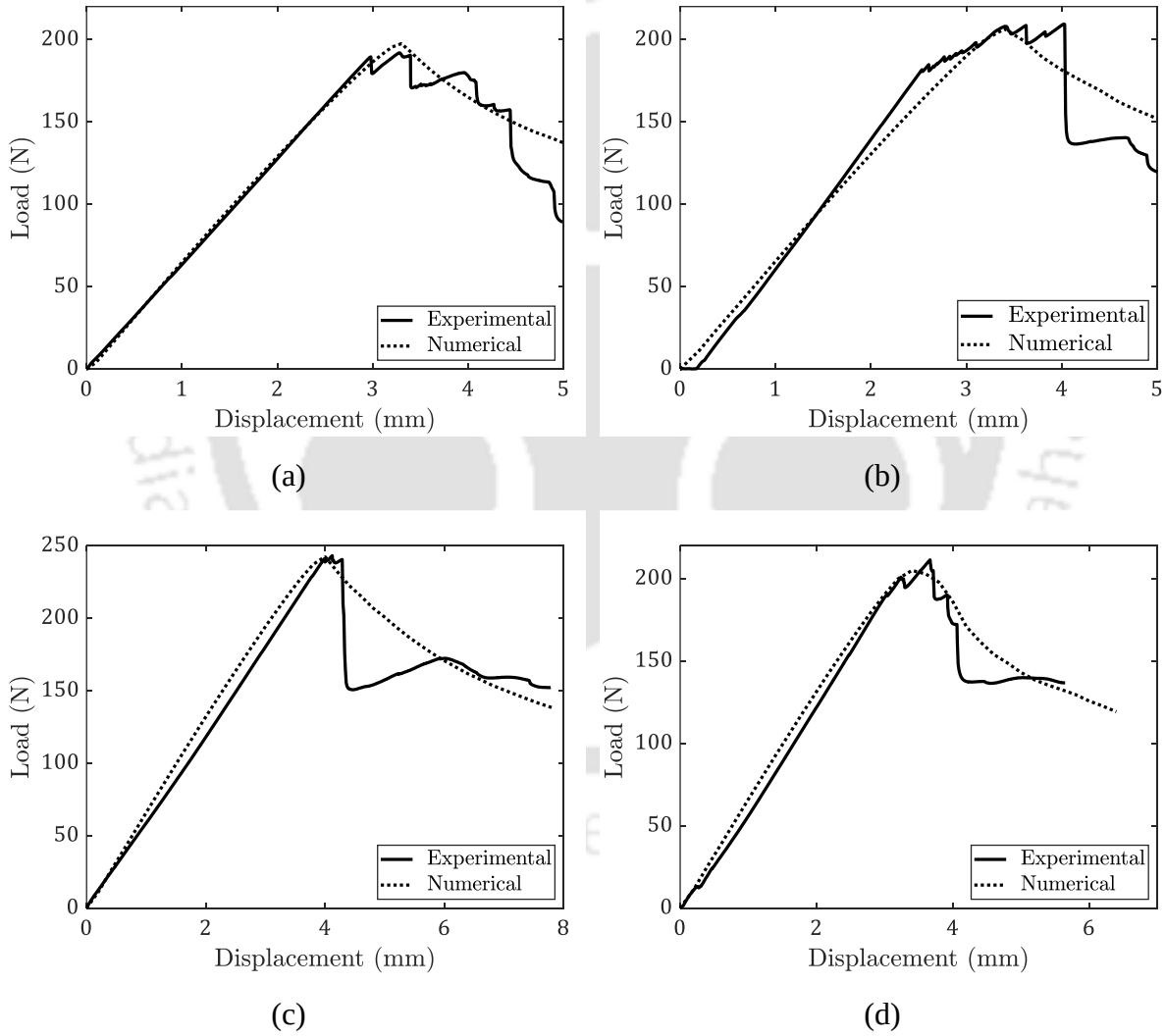

Fig. 7.19 Numerical validation with lever length c =68 mm for (a) Pristine, (b) 0.1 wt.%, (c) 0.2 wt.%, and (d) 0.3 wt.% of MWCNTs

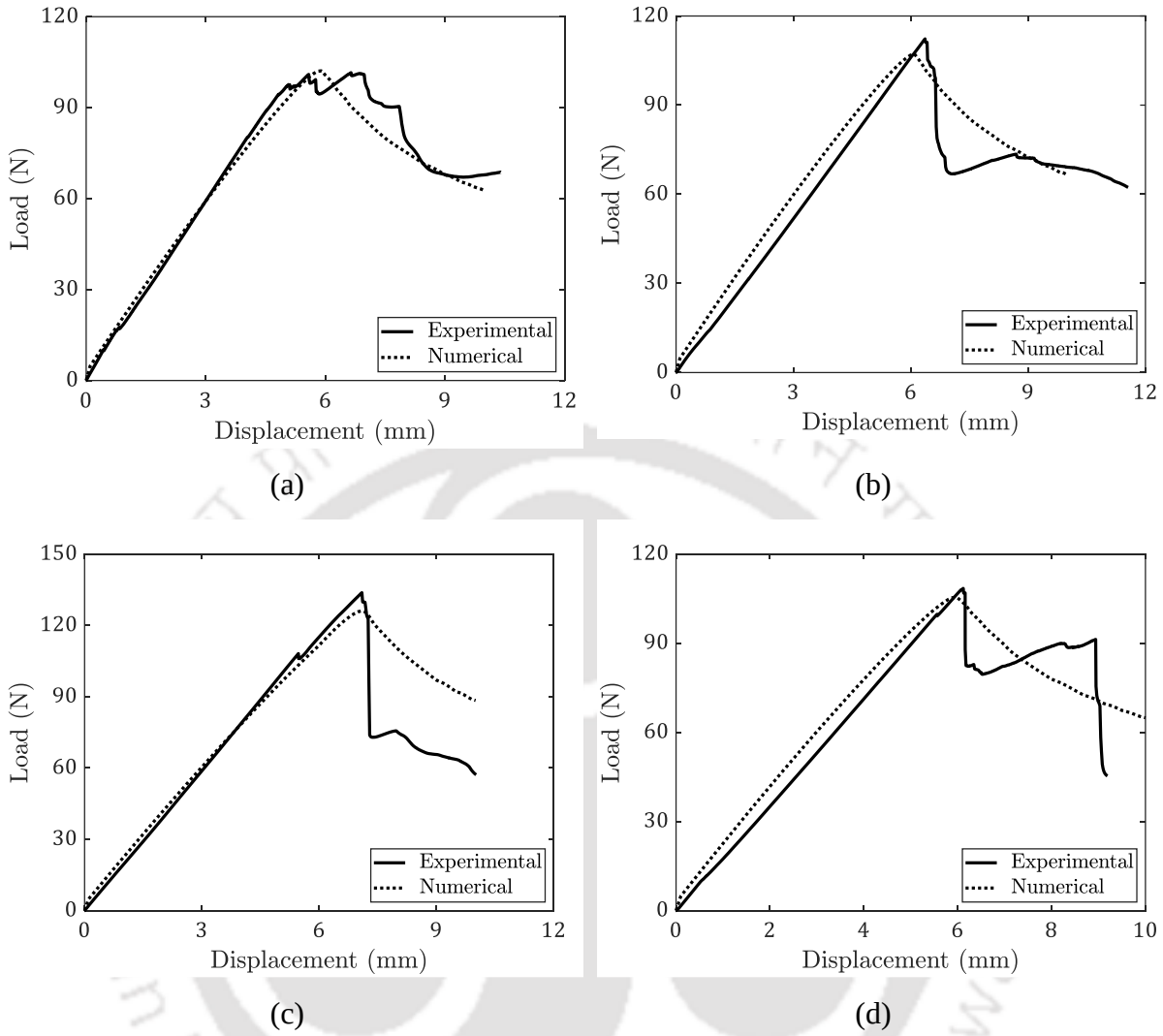

Fig. 7.20 Numerical validation with lever length c =104 mm for (a) Pristine, (b) 0.1 wt.%, (c) 0.2 wt.%, and (d) 0.3 wt.% of MWCNTs

7.7 Closure

This chapter uses an intrinsic triangular CZM to validate the mode I and mode II delamination response of the CFRP composite laminate. The CZM parameters obtained from the specific fracture characterization tests are directly provided into the numerical model, eliminating the need for resource-intensive trial-and-error computations. The influence of the CZM parameters on the delamination behaviour of composites is investigated through some parametric analysis.

The mode-independent CZM parameters are combined with appropriate damage criteria to validate the mixed-mode delamination response. The computational outcomes exhibit a

reasonable agreement with the experimental findings, thus affirming the reliability of the experimental methods employed. This validation of the delamination response covers three specific mixed-mode ratios with less than 5% error in the peak load. This approach can be extended to evaluate delamination behaviour under various mixed-mode conditions.

Chapter 8 Conclusions and Future Scope

This final chapter provides an overview of the current study, followed by key findings and the scope for future research. The last section of this chapter outlines the contributions made by this thesis.

8.1 Observations and discussions

The primary objective of the present work is to extend the applicability of the CZM for predicting the interface fracture of adhesively bonded joints and laminated composites. A semi-analytical asymptotic stress and displacement field solution is obtained for mode I and mode II interface fracture analysis in a cohesive zone for any generalized extrinsic cohesive law that nullifies the crack tip singularity, assuming no friction between the crack surfaces. The solution coefficients depended on the type of cohesive law, material geometry, and the boundary conditions of the problem. However, there is no need to evaluate the coefficients for a given cohesive zone length ρ of constant cohesive T-S-L. The obtained SIFs using the domain-independent interaction integral ascertain the reduction in the strength of the singularity. The computed results agree well with the analytical formulation for determining the SIF. The presented procedure could be easily extended to higher-order extrinsic T-S-Ls with finite traction at zero separation.

The interaction integral method, which is not specific to any particular domain, is used to estimate the SIF, considering the traction along the crack faces. The SIF is computed for three types of extrinsic cohesive laws: constant traction, linear, and parabolic softening. The strength of stress singularity is determined across a range of cohesive zone lengths, with the cohesive strength being kept constant for all three types of cohesive laws. It is observed that the decrease in the SIF is more pronounced when using the constant traction cohesive law as compared to the linear and parabolic softening models. This is primarily because, in the case of a constant traction cohesive law, the stress intensity caused by the presence of the cohesive zone increases rapidly, leading to a rapid reduction in the overall SIF.

The brittleness number related to cohesive law parameters and material geometry specifications affects the load-displacement curve, thus demonstrating the ability of ductile to

brittle crack propagation phenomenon along the interface. For the same value of the brittleness number, different load-displacement responses are obtained for various extrinsic CZMs. The load-displacement responses are also presented for linear softening cohesive law for different brittleness number values under pure mode I and mode II loading conditions.

The failure in the bonded interface is simulated using the SIF nullification criteria within the framework of the extrinsic CZM. A pre-cracked adhesively bonded PMMA disc-shaped CT specimen is fabricated and subjected to mode I loading conditions in the UTM to investigate the interface crack propagation; this corresponds to brittle failure. Additionally, the influence of MWCNTs on the mode II failure behaviour is investigated by conducting interface fracture studies on adhesively bonded aluminum joints. In the FE analysis considering a linear softening cohesive law, the load required for incremental crack growth is determined by nullifying the SIF at the mathematical crack tip. The FE results agreed with the experimental data, demonstrating the effectiveness of extrinsic CZM in the interface crack propagation problems. The intrinsic CZM parameters are also estimated for mode II crack propagation studies and compared with the extrinsic CZM counterpart.

Experimentally estimating the CZM parameters — cohesive strength and fracture energy, is another significant finding of the present thesis work. Most researchers evaluate the CZM parameters using direct and indirect procedures involving dedicated experimental setup or numerically intensive computational resources. The present work evaluates the CZM parameters for pristine and MWCNTs-reinforced CFRP laminate with routine experimental facilities (UTM) under mode I and mode II loading conditions. The cohesive strength is evaluated using the cross-tension and SBS tests under mode I and mode II loadings, respectively. Moreover, the fracture energy is estimated using the standard DCB and ENF test procedures provided in the ASTM standard.

The influence of hydroxyl functionalized MWCNTs on the interlaminar strength and fracture toughness of the CFRP is also investigated in the present work. It is observed that the mode I interface strength and interlaminar shear strength for 0.2 wt.% MWCNTs reinforced composite increases by 24.37% and 14.03% compared to the pristine composites. Additionally, adding MWCNTs up to 0.2 wt.% increases the mode I and mode II fracture toughness by

47.72% and 14.63% compared to the pristine composites. The higher MWCNTs contents, i.e., 0.3 wt.% of MWCNTs, however, reduce the effective stress transfer and the fracture toughness of the composites.

The mixed-mode (I/II) fracture toughness of the composites reinforced with MWCNTs is evaluated under three distinct mixed-mode ratios. Increasing the mixed-mode ratios is achieved by reducing the lever length, which improves the mixed-mode interlaminar fracture toughness. The improvement in mixed-mode fracture toughness exhibits a similar pattern observed under mode I and mode II loading. Specifically, the mixed-mode fracture toughness increases up to 0.2 wt.% of MWCNTs but declines beyond this point. The FESEM analysis of the fractured surfaces also confirms the enhancement in the fracture toughness. The improvement of mode I fracture toughness is prominently due to the fiber bridging and rough surface textures. Similarly, the interlaminar fracture surface with 0.2 wt.% of MWCNTs shows a higher density of hackles, indicating the resistance to crack propagation by the nano-reinforced matrix.

The obtained material properties and cohesive parameters are directly imputed into the FE model with a triangular T-S-L to validate the load-displacement response for pristine and all proportions of MWCNTs under mode I, mode II, and mixed-mode (I/II) loading conditions. The effective orthotropic properties of the nanofiller-reinforced CFRP are computed using the rule of mixtures and the homogenization technique using periodic boundary conditions. The accuracy between the experimental and the numerically simulated load vs. displacement responses confirms the sufficiency and reliability of the experimental test procedures. The maximum error in the peak load between the numerical and experimental results is less than 5%.

8.2 Thesis contributions

The contributions of the thesis can be summarized as

i. A semi-analytical procedure is used to estimate the SIF in the presence of the CZM for any generalized extrinsic cohesive law.
ii. The failure response of an adhesively bonded interface is investigated using different extrinsic CZMs that possess identical brittleness number values.

iii. The influence of MWCNTs on the mode II interface fracture of adhesively bonded joints is investigated.

iv. A suitable extrinsic CZM methodology based on SIF nullification criteria is proposed to validate the brittle fracture of adhesively bonded joints under mode I and mode II loading conditions.

v. A simplified experimental methodology is developed to evaluate the CZM parameters for lesser utilized hydroxyl functionalized MWCNTs reinforced CFRP under mode I and mode II loading scenarios.

vi. The mixed-mode (I/II) delamination response is evaluated for MWCNTs reinforced composites by varying the lever length of the MMB apparatus.

vii. FE modelling is performed to investigate the authenticity of the experimental obtained CZM parameters.

viii. FESEM analysis of delaminated CFRP is carried out to understand the fracture mechanism under mode I, mode II, and mixed-mode loading conditions.

8.3 Conclusions

The main conclusions of the present thesis are summarized as follows:

i. The SIFs obtained using the domain-independent interaction integral closely match the analytical and semi-analytical results of constant traction and linear softening cohesive law. This method can readily be expanded to accommodate higher-order extrinsic T-S-Ls.

ii. The SIF decreases rapidly for constant T-S-L with cohesive zone length, followed by linear and parabolic T-S-L. Therefore, not only the magnitude of the cohesive stress but also its variations is another critical factor influencing the crack tip SIF.

iii. Lower order T-S-L is recommended to nullify the SIF for a small cohesive zone length.

iv. The load-displacement response does not solely depend on the values of the brittleness number but is also influenced by the order of the extrinsic cohesive laws used.

v. The load required for an incremental crack growth is determined by nullifying the SIF at the mathematical crack tip with linear softening cohesive law. The FE results agreed with the experimental data (with an error of less than 5%), demonstrating the effectiveness of extrinsic CZM to model interface crack propagation problems.

vi. The strength of the adhesively bonded aluminum joints is maximum for 0.2 wt.% of MWCNTs. Any further increase in MWCNT concentration leads to deteriorated strength, possibly due to the agglomeration of MWCNTs in the epoxy.

vii. The experimental peak load is the only factor influencing the intrinsic CZM strength. However, the failure displacement of the load-displacement response determines the extrinsic cohesive strength.

viii. The cohesive strength and fracture energy of the MWCNTs reinforced composite laminate are estimated from the cross-tension and DCB test for pure mode I loading conditions. The SBS and ENF tests are used to evaluate the cohesive strength and fracture energy under mode II loadings, respectively.

ix. It is noticed that the addition of MWCNTs up to 0.2 wt.% increases the interface strength and fracture energy proportionally. The mode I interface strength and fracture energy increase is 24.37% and 47.72% for 0.2 wt.% of MWCNTs compared to pristine composites. The specific surface textures (fiber bridging and the presence of hackles) also confirm the improvement of interlaminar fracture toughness with the addition of MWCNTs.

x. The mode II interlaminar shear strength and fracture energy for 0.2 wt.% reinforced composites are increased by 14.03% and 14.63%, respectively, compared to pristine composite.

8.4 Future scope

i. The extrinsic CZM methodology based on the SIF nullification procedure can be used to validate the mixed-mode fracture of adhesively bonded joints.

ii. The adhesively bonded structure does not solely depend on the values of the brittleness number but is also influenced by the order of the cohesive laws used. A parameter that considers cohesive strength, cohesive energy, and order of the cohesive

law could be used as a better measure for predicting the same load vs. displacement response.

iii. Estimating cohesive stiffness from experimental studies or other direct approaches will reduce the computational effort on interface failure.

List of Publications

International Journals

[1] Saikia P.J, Muthu N. Extrinsic cohesive zone modelling for interface crack growth: Numerical and experimental studies. Eng Fract Mech 2022;266:108353. https://doi.org/10.1016/j.engfracmech.2022.108353.

[2] Saikia P.J, Muthu N. Extrinsic/intrinsic cohesive zone modelling and experiments on interface failure of multi-walled carbon nanotube reinforced adhesively bonded joints under mode II loading. Theor Appl Fract Mech 2023;126:103967. https://doi.org/10.1016/j.tafmec.2023.103967.

[3] Saikia P.J, Kumar M, Kumar A, Muthu N. Experimental estimation and numerical validation of cohesive zone parameters in hydroxyl functionalized MWCNTs-reinforced CFRP under pure mode II loading. Polym Compos.2024;1-15. doi:10.1002/pc.28337

[4] Saikia, P.J., Kumar A., Kumar M. and Muthu, N. Cohesive zone parameters to predict mixed-mode delamination in CFRP reinforced with hydroxyl functionalized MWCNTs: Experimental and Numerical investigations (Under review in Engineering Fracture Mechanics)

Conferences

[1] Saikia, P.J., Muthu, N. Identification of Cohesive Zone Parameters for a bi-material Interface Crack, 1st Online International Conference on Recent Advances in Computational and Experimental Mechanics, IIT Kharagpur, September 4-6, 2020.

[2] Saikia, P.J., Muthu, N. Equivalency between Cohesive zone model and linear elastic fracture mechanics for an Isotropic Crack, 65^{th} congress of the Indian Society of Theoretical and Applied Mechanics, IIT Kharagpur, December 9-11, 2020.

[3] Saikia, P.J, Kumar M., Muthu, N. Enhancing the mode I interlaminar fracture toughness of carbon fiber-reinforced composite with hydroxyl functionalized MWCNTs; Numerical and Experimental study, The 8th Asian Conference on Mechanics of Functional Materials and Structures, IIT Guwahati, December 11-14, 2022.

[4] Saikia, P.J, Kumar M., Muthu, N. The effect of hydroxyl functionalized MWCNTs on the interlaminar fracture toughness of Basalt fiber-reinforced epoxy composite, Structural Integrity Conference and Exhibition, December 14-16, 2022.

References

[1] da Silva LFM, Campilho RDSG. Advances in Numerical Modelling of Adhesive Joints. Berlin, Heidelberg: Springer Berlin Heidelberg; 2012. https://doi.org/10.1007/978-3-642-23608-2.

[2] CE I. Stresses in a plate due to the presence of cracks and sharp corners. Trans Inst Nav Arch 1913;55:219–41.

[3] Griffith AA. VI. The phenomena of rupture and flow in solids. Philos Trans R Soc London Ser A, Contain Pap a Math or Phys Character 1921;221:163–98.

[4] Yarema SY. On the contribution of G. R. Irwin to fracture mechanics. Mater Sci 1996;31:617–23. https://doi.org/10.1007/BF00558797.

[5] Westergaard HM. Bearing Pressures and Cracks: Bearing Pressures Through a Slightly Waved Surface or Through a Nearly Flat Part of a Cylinder, and Related Problems of Cracks. J Appl Mech 1939;6:A49–53. https://doi.org/10.1115/1.4008919.

[6] Williams ML. The Bending Stress Distribution at the Base of a Stationary Crack. J Appl Mech 1961;28:78–82. https://doi.org/10.1115/1.3640470.

[7] Griffits AA. VI. The phenomena of rupture and flow in solids. Philos Trans R Soc London Ser A, Contain Pap a Math or Phys Character 1921;221:163–98. https://doi.org/10.1098/rsta.1921.0006.

[8] Irwin GR. Analysis of Stresses and Strains Near the End of a Crack Traversing a Plate. J Appl Mech 1957;24:361–4. https://doi.org/10.1115/1.4011547.

[9] Fan C, Jar P-Y Ben, Cheng JJR. Cohesive zone with continuum damage properties for simulation of delamination development in fiber composites and failure of adhesive joints. Eng Fract Mech 2008;75:3866–80. https://doi.org/10.1016/j.engfracmech.2008.02.010.

[10] Shahin K, Taheri F. The strain energy release rates in adhesively bonded balanced and unbalanced specimens and lap joints. Int J Solids Struct 2008;45:6284–300. https://doi.org/10.1016/j.ijsolstr.2008.07.030.

[11] Reeder J, Crews, Jr. J. The mixed-mode bending method for delamination testing. 30th Struct. Struct. Dyn. Mater. Conf., vol. 28, Reston, Virigina: American Institute of Aeronautics and Astronautics; 1989, p. 1270–6. https://doi.org/10.2514/6.1989-1347.

[12] Noorman DC. Cohesive Zone Modelling in Adhesively Bonded Joints. Thesis 2014:172.

[13] Krueger R. Virtual crack closure technique: History, approach, and applications. Appl Mech Rev 2004;57:109–43. https://doi.org/10.1115/1.1595677.

[14] Turon Travesa A. Simulation of delamination in composites under quasi-static and fatigue loading using cohesive zone models. Universitat de Girona; 2006.

[15] Chow WT, Atluri SN. Finite element calculation of stress intensity factors for interfacial crack using virtual crack closure integral. Comput Mech 1995;16:417–25. https://doi.org/10.1007/BF00370563.

[16] Belytschko T, Black T. Elastic crack growth in finite elements with minimal remeshing. Int J Numer Methods Eng 1999;45:601–20. https://doi.org/10.1002/(SICI)1097-0207(19990620)45:5<601::AID-NME598>3.0.CO;2-S.

[17] Daux C, Moës N, Dolbow J, Sukumar N, Belytschko T. Arbitrary branched and intersecting cracks with the extended finite element method. Int J Numer Methods Eng 2000;48:1741–60. https://doi.org/10.1002/1097-0207(20000830)48:12<1741::AID-NME956>3.0.CO;2-L.

[18] Fagerström M, Larsson R. Theory and numerics for finite deformation fracture modelling using strong discontinuities. Int J Numer Methods Eng 2006;66:911–48. https://doi.org/10.1002/nme.1573.

[19] Xu Y, Yuan H. Computational analysis of mixed-mode fatigue crack growth in quasi-brittle materials using extended finite element methods. Eng Fract Mech 2009;76:165–81. https://doi.org/10.1016/j.engfracmech.2008.08.011.

[20] Muthu N, Maiti SK, Falzon BG, Yan W. Crack propagation in non-homogenous materials: Evaluation of mixed-mode SIFs, T-stress and kinking angle using a variant of EFG Method. Eng Anal Bound Elem 2016;72:11–26. https://doi.org/10.1016/j.enganabound.2016.07.017.

[21] Rice JR, Rosengren GF. Plane strain deformation near a crack tip in a power-law hardening material. J Mech Phys Solids 1968;16:1–12. https://doi.org/10.1016/0022-5096(68)90013-6.

[22] Desmorat JLR, Lemaitre J. „Engineering Damage Mechanics" 2005.

[23] Talreja R. Damage and failure of composite materials. Adv. Theor. Deform. Damage Fail. Mater., Springer; 2022, p. 235–80.

[24] Liljedahl CDM, Crocombe AD, Wahab MA, Ashcroft IA. Damage modelling of adhesively bonded joints. Int J Fract 2006;141:147–61. https://doi.org/10.1007/s10704-006-0072-9.

[25] Yang QD, Thouless MD. Mixed-mode fracture analyses of plastically-deforming adhesive joints. Int J Fract 2001;110:175–87. https://doi.org/10.1023/A:1010869706996.

[26] Turon A, Costa J, Camanho PP, Dávila CG. Simulation of delamination in composites under high-cycle fatigue. Compos Part A Appl Sci Manuf 2007;38:2270–82. https://doi.org/10.1016/j.compositesa.2006.11.009.

[27] Song SH, Paulino GH, Buttlar WG. A bilinear cohesive zone model tailored for fracture of asphalt concrete considering viscoelastic bulk material. Eng Fract Mech 2006;73:2829–48. https://doi.org/10.1016/j.engfracmech.2006.04.030.

[28] Kafkalidis MS, Thouless MD. The effects of geometry and material properties on the fracture of single lap-shear joints. Int J Solids Struct 2002;39:4367–83. https://doi.org/10.1016/S0020-7683(02)00344-X.

[29] Elliott HA. An analysis of the conditions for rupture due to griffith cracks. Proc Phys Soc 1947;59:208–23. https://doi.org/10.1088/0959-5309/59/2/305.

[30] Barenblatt GI. The Mathematical Thsory of Equilibrium Cracks in Brittle Fracture (Initial Experiment for Hydogel as a Medium for...). Adv Appl Mech 1962;7:55–129.

[31] Dugdale DS. Yielding of steel sheets containing slits. J Mech Phys Solids 1960;8:100–

4. https://doi.org/10.1016/0022-5096(60)90013-2.

[32] Camacho GT, Ortiz M. Computational modelling of impact damage in brittle materials. Int J Solids Struct 1996;33:2899–938. https://doi.org/10.1016/0020-7683(95)00255-3.

[33] Needleman A. A Continuum Model for Void Nucleation by Inclusion Debonding. J Appl Mech 1987;54:525–31. https://doi.org/10.1115/1.3173064.

[34] Xu X-P, Needleman A. Void nucleation by inclusion debonding in a crystal matrix. Model Simul Mater Sci Eng 1993;1:111–32. https://doi.org/10.1088/0965-0393/1/2/001.

[35] Tvergaard V, Hutchinson JW. The relation between crack growth resistance and fracture process parameters in elastic-plastic solids. J Mech Phys Solids 1992;40:1377–97. https://doi.org/10.1016/0022-5096(92)90020-3.

[36] Park K, Paulino GH, Roesler JR. A unified potential-based cohesive model of mixed-mode fracture. J Mech Phys Solids 2009;57:891–908. https://doi.org/10.1016/j.jmps.2008.10.003.

[37] Park K, Paulino GH. Cohesive Zone Models: A Critical Review of Traction-Separation Relationships Across Fracture Surfaces. Appl Mech Rev 2011;64. https://doi.org/10.1115/1.4023110.

[38] Needleman A. Micromechanical modelling of interfacial decohesion. Ultramicroscopy 1992;40:203–14. https://doi.org/10.1016/0304-3991(92)90117-3.

[39] Feraren P, Jensen HM. Cohesive zone modelling of interface fracture near flaws in adhesive joints. Eng Fract Mech 2004;71:2125–42. https://doi.org/10.1016/j.engfracmech.2003.12.003.

[40] Campilho RDSG, Moura MFSF de, Ramantani DA, Morais JJL, Barreto AMJP, Domingues JJMS. Adhesively Bonded Repair Proposal for Wood Members Damaged by Horizontal Shear Using Carbon-Epoxy Patches. J Adhes 2010;86:649–70. https://doi.org/10.1080/00218464.2010.484318.

[41] Campilho RDSG, Banea MD, Pinto AMG, Da Silva LFM, De Jesus AMP. Strength prediction of single- and double-lap joints by standard and extended finite element

modelling. Int J Adhes Adhes 2011;31:363–72. https://doi.org/10.1016/j.ijadhadh.2010.09.008.

[42] Xie D, Waas AM. Discrete cohesive zone model for mixed-mode fracture using finite element analysis. Eng Fract Mech 2006;73:1783–96. https://doi.org/10.1016/j.engfracmech.2006.03.006.

[43] Harper PW, Hallett SR. Cohesive zone length in numerical simulations of composite delamination. Eng Fract Mech 2008;75:4774–92. https://doi.org/10.1016/j.engfracmech.2008.06.004.

[44] Elices M, Guinea GV, Gómez J, Planas J. The cohesive zone model: advantages, limitations and challenges. Eng Fract Mech 2002;69:137–63. https://doi.org/10.1016/S0013-7944(01)00083-2.

[45] Wells A. Unstable crack propagation in metals: cleavage and fast fracture. Proc. crack Propag. Symp., vol. 1, 1961, p. 26028.

[46] Maiti SK. Fracture mechanics: fundamentals and applications. Cambridge University Press; 2015.

[47] Sun C-T, Jin Z. Fracture mechanics. Academic press; 2011.

[48] Rice JR. A Path Independent Integral and the Approximate Analysis of Strain Concentration by Notches and Cracks. J Appl Mech 1968;35:379–86. https://doi.org/10.1115/1.3601206.

[49] Rice JR, others. Mathematical analysis in the mechanics of fracture. Fract an Adv Treatise 1968;2:191–311.

[50] Stern M, Becker EB, Dunham RS. A contour integral computation of mixed-mode stress intensity factors. Int J Fract 1976;12:359–68. https://doi.org/10.1007/BF00032831.

[51] Ramesh K, Lewis G. Digital photoelasticity: advanced techniques and applications. Appl Mech Rev 2002;55:B69--B71.

[52] de Moura MFSF, Gonçalves JPM, Magalhães AG. A straightforward method to obtain

the cohesive laws of bonded joints under mode I loading. Int J Adhes Adhes 2012;39:54–9. https://doi.org/10.1016/j.ijadhadh.2012.07.008.

[53] Choupani N. Mixed-mode cohesive fracture of adhesive joints: Experimental and numerical studies. Eng Fract Mech 2008;75:4363–82. https://doi.org/10.1016/j.engfracmech.2008.04.023.

[54] Hafiz TA, Abdel Wahab MM, Crocombe AD, Smith PA. Mixed-mode fracture of adhesively bonded metallic joints under quasi-static loading. Eng Fract Mech 2010;77:3434–45. https://doi.org/10.1016/j.engfracmech.2010.09.015.

[55] Banea MD, da Silva LFM, Campilho RDSG. Mode I fracture toughness of adhesively bonded joints as a function of temperature: Experimental and numerical study. Int J Adhes Adhes 2011;31:273–9. https://doi.org/10.1016/j.ijadhadh.2010.09.005.

[56] Gleich DM, Van Tooren MJL, Beukers A. Analysis and evaluation of bondline thickness effects on failure load in adhesively bonded structures. J Adhes Sci Technol 2001;15:1091–101. https://doi.org/10.1163/156856101317035503.

[57] Han X, Jin Y, da Silva LFM, Costa M, Wu C. On the effect of adhesive thickness on mode I fracture energy - an experimental and modelling study using a trapezoidal cohesive zone model. J Adhes 2020;96:490–514. https://doi.org/10.1080/00218464.2019.1601087.

[58] Rahmani A, Choupani N. Experimental and numerical analysis of fracture parameters of adhesively bonded joints at low temperatures. Eng Fract Mech 2019;207:222–36. https://doi.org/10.1016/j.engfracmech.2018.12.031.

[59] Andersson T, Biel A. On the effective constitutive properties of a thin adhesive layer loaded in peel. Int J Fract 2006;141:227–46. https://doi.org/10.1007/s10704-006-0075-6.

[60] Marzi S, Biel A, Stigh U. On experimental methods to investigate the effect of layer thickness on the fracture behaviour of adhesively bonded joints. Int J Adhes Adhes 2011;31:840–50. https://doi.org/10.1016/j.ijadhadh.2011.08.004.

[61] Chaves FJP, da Silva LFM, de Moura MFSF, Dillard DA, Esteves VHC. Fracture

Mechanics Tests in Adhesively Bonded Joints: A Literature Review. J Adhes 2014;90:955–92. https://doi.org/10.1080/00218464.2013.859075.

[62] Choupani N. Interfacial mixed-mode fracture characterization of adhesively bonded joints. Int J Adhes Adhes 2008;28:267–82. https://doi.org/10.1016/j.ijadhadh.2007.08.002.

[63] Pang HLJ, Seetoh CW. A Compact Mixed Mode (CMM) fracture specimen for adhesive bonded joints. Eng Fract Mech 1997;57:57–65. https://doi.org/10.1016/S0013-7944(97)00014-3.

[64] Jokinen J, Wallin M, Saarela O. Applicability of VCCT in mode I loading of yielding adhesively bonded joints—a case study. Int J Adhes Adhes 2015;62:85–91. https://doi.org/10.1016/j.ijadhadh.2015.07.004.

[65] Azimi M, Mirjavadi SS, Asli SA, Hamouda AMS. Fracture Analysis of a Special Cracked Lap Shear (CLS) Specimen with Utilization of Virtual Crack Closure Technique (VCCT) by Finite Element Methods. J Fail Anal Prev 2017;17:304–14. https://doi.org/10.1007/s11668-017-0243-1.

[66] Demoura M, Campilho R, Goncalves J. Crack equivalent concept applied to the fracture characterization of bonded joints under pure mode I loading. Compos Sci Technol 2008;68:2224–30. https://doi.org/10.1016/j.compscitech.2008.04.003.

[67] Campilho RDSG, Banea MD, Neto JABP, da Silva LFM. Modelling adhesive joints with cohesive zone models: effect of the cohesive law shape of the adhesive layer. Int J Adhes Adhes 2013;44:48–56. https://doi.org/10.1016/j.ijadhadh.2013.02.006.

[68] Sadeghi MZ, Gabener A, Zimmermann J, Saravana K, Weiland J, Reisgen U, et al. Failure load prediction of adhesively bonded single lap joints by using various FEM techniques. Int J Adhes Adhes 2020;97:102493. https://doi.org/10.1016/j.ijadhadh.2019.102493.

[69] Gong Y, Zhang B, Hallett SR. Delamination migration in multidirectional composite laminates under mode I quasi-static and fatigue loading. Compos Struct 2018;189:160–

76. https://doi.org/10.1016/j.compstruct.2018.01.074.

[70] Tan W, Naya F, Yang L, Chang T, Falzon BG, Zhan L, et al. The role of interfacial properties on the intralaminar and interlaminar damage behaviour of unidirectional composite laminates: Experimental characterization and multiscale modelling. Compos Part B Eng 2018;138:206–21. https://doi.org/10.1016/j.compositesb.2017.11.043.

[71] Andersons J, König M. Dependence of fracture toughness of composite laminates on interface ply orientations and delamination growth direction. Compos Sci Technol 2004;64:2139–52. https://doi.org/10.1016/j.compscitech.2004.03.007.

[72] Pereira AB, de Morais AB. Mode I interlaminar fracture of carbon/epoxy multidirectional laminates. Compos Sci Technol 2004;64:2261–70. https://doi.org/10.1016/j.compscitech.2004.03.001.

[73] Pereira AB, de Morais AB, Marques AT, de Castro PT. Mode II interlaminar fracture of carbon/epoxy multidirectional laminates. Compos Sci Technol 2004;64:1653–9. https://doi.org/10.1016/j.compscitech.2003.12.001.

[74] Asp LE. The effects of moisture and temperature on the interlaminar delamination toughness of a carbon/epoxy composite. Compos Sci Technol 1998;58:967–77. https://doi.org/10.1016/S0266-3538(97)00222-4.

[75] Lucas JP. Delamination fracture: Effect of fiber orientation on fracture of a continuous fiber composite laminate. Eng Fract Mech 1992;42:543–61. https://doi.org/10.1016/0013-7944(92)90173-C.

[76] de Morais A. Mode-I interlaminar fracture of carbon/epoxy cross-ply composites. Compos Sci Technol 2002;62:679–86. https://doi.org/10.1016/S0266-3538(01)00223-8.

[77] Zhao L, Wang Y, Zhang J, Gong Y, Hu N, Li N. XFEM-based model for simulating zigzag delamination growth in laminated composites under mode I loading. Compos Struct 2017;160:1155–62. https://doi.org/10.1016/j.compstruct.2016.11.006.

[78] Turon A, Camanho PP, Costa J, Renart J. Accurate simulation of delamination growth under mixed-mode loading using cohesive elements: Definition of interlaminar strengths and elastic stiffness. Compos Struct 2010;92:1857–64.

https://doi.org/10.1016/j.compstruct.2010.01.012.

[79] Lu X, Ridha M, Chen BY, Tan VBC, Tay TE. On cohesive element parameters and delamination modelling. Eng Fract Mech 2019;206:278–96. https://doi.org/10.1016/j.engfracmech.2018.12.009.

[80] Zhao L, Gong Y, Zhang J, Chen Y, Fei B. Simulation of delamination growth in multidirectional laminates under mode I and mixed mode I/II loadings using cohesive elements. Compos Struct 2014;116:509–22. https://doi.org/10.1016/j.compstruct.2014.05.042.

[81] Ejaz H, Mubashar A, Uddin E, Ali Z, Arif N. Influence of MWCNTs on strength properties of high viscous epoxy adhesive and fracture behaviour of adhesively bonded joints. Theor Appl Fract Mech 2022;120:103412. https://doi.org/10.1016/j.tafmec.2022.103412.

[82] Esmaeili A, Sbarufatti C, Casati R, Jiménez-Suárez A, Ureña A, Hamouda AMS. Effective addition of nanoclay in enhancement of mechanical and electromechanical properties of SWCNT reinforced epoxy: Strain sensing and crack-induced piezoresistivity. Theor Appl Fract Mech 2020;110:102831. https://doi.org/10.1016/j.tafmec.2020.102831.

[83] Zhang D, Huang Y. The bonding performances of carbon nanotube (CNT)-reinforced epoxy adhesively bonded joints on steel substrates. Prog Org Coatings 2021;159:106407. https://doi.org/10.1016/j.porgcoat.2021.106407.

[84] Khoramishad H, Ashofteh RS, Mobasheri M, Berto F. Temperature dependence of the shear strength in adhesively bonded joints reinforced with multi-walled carbon nanotubes. Eng Fract Mech 2018;199:179–87. https://doi.org/10.1016/j.engfracmech.2018.05.032.

[85] Khoramishad H, Ashofteh RS, Pourang H, Berto F. Experimental investigation of the influence of temperature on the reinforcing effect of graphene oxide nano-platelet on nanocomposite adhesively bonded joints. Theor Appl Fract Mech 2018;94:95–100.

https://doi.org/10.1016/j.tafmec.2018.01.010.

[86] Kim WJ, Kang SO, Ah CS, Lee YW, Ha DH, Choi IS, et al. Functionalization of Shortened SWCNTs Using Esterification. Bull Korean Chem Soc 2004;25:1301–2. https://doi.org/10.5012/bkcs.2004.25.9.1301.

[87] Hsiao K-T, Alms J, Advani SG. Use of epoxy/multiwalled carbon nanotubes as adhesives to join graphite fiber reinforced polymer composites. Nanotechnology 2003;14:791–3. https://doi.org/10.1088/0957-4484/14/7/316.

[88] Tarfaoui M, Lafdi K, El Moumen A. Mechanical properties of carbon nanotubes based polymer composites. Compos Part B Eng 2016;103:113–21. https://doi.org/10.1016/j.compositesb.2016.08.016.

[89] Gude MR, Prolongo SG, Gómez-del Río T, Ureña A. Mode-I adhesive fracture energy of carbon fiber composite joints with nanoreinforced epoxy adhesives. Int J Adhes Adhes 2011;31:695–703. https://doi.org/10.1016/j.ijadhadh.2011.06.016.

[90] Mujika F, Vargas G, Ibarretxe J, De Gracia J, Arrese A. Influence of the modification with MWCNT on the interlaminar fracture properties of long carbon fiber composites. Compos Part B Eng 2012;43:1336–40. https://doi.org/10.1016/j.compositesb.2011.11.020.

[91] Carpinteri A. Size effect in fracture toughness testing: a dimensional analysis approach. Anal Exp Fract Mech 1980:785–97.

[92] Carpinteri A. Notch sensitivity in fracture testing of aggregative materials. Eng Fract Mech 1982;16:467–81. https://doi.org/10.1016/0013-7944(82)90127-8.

[93] Carpinteri A, Colombo G. Numerical analysis of catastrophic softening behaviour (snap-back instability). Comput Struct 1989;31:607–36. https://doi.org/10.1016/0045-7949(89)90337-4.

[94] Moës N, Belytschko T. Extended finite element method for cohesive crack growth. Eng Fract Mech 2002;69:813–33. https://doi.org/10.1016/S0013-7944(01)00128-X.

[95] Li X, Lu S, Lubineau G. Snap-back instability of double cantilever beam with bridging.

Int J Solids Struct 2021;233:111150. https://doi.org/10.1016/j.ijsolstr.2021.111150.

[96] Lacidogna G, Accornero F, Carpinteri A. Influence of snap-back instabilities on Acoustic Emission damage monitoring. Eng Fract Mech 2019;210:3–12. https://doi.org/10.1016/j.engfracmech.2018.06.042.

[97] Jin Z-H, Paulino GH, Dodds RH. Cohesive fracture modelling of elastic–plastic crack growth in functionally graded materials. Eng Fract Mech 2003;70:1885–912. https://doi.org/10.1016/S0013-7944(03)00130-9.

[98] Zhang Z (Jenny), Paulino GH. Cohesive zone modelling of dynamic failure in homogeneous and functionally graded materials. Int J Plast 2005;21:1195–254. https://doi.org/10.1016/j.ijplas.2004.06.009.

[99] Ortiz M, Pandolfi A. Finite-deformation irreversible cohesive elements for three-dimensional crack-propagation analysis. Int J Numer Methods Eng 1999;44:1267–82. https://doi.org/10.1002/(SICI)1097-0207(19990330)44:9<1267::AID-NME486>3.0.CO;2-7.

[100] Jin Z-H, Sun CT. Cohesive zone modelling of interface fracture in elastic bi-materials. Eng Fract Mech 2005;72:1805–17. https://doi.org/10.1016/j.engfracmech.2004.09.011.

[101] Xiao Q, Karihaloo BL. Asymptotic fields at frictionless and frictional cohesive crack tips in quasibrittle materials. J Mech Mater Struct 2006;1:881–910. https://doi.org/10.2140/jomms.2006.1.881.

[102] Muskhelishvili, Nikolaĭ Ivanovich. Some basic problems of the mathematical theory of elasticity. Vol. 15. Groningen: Noordhoff, 1953.

[103] Karihaloo BL, Xiao QZ. Asymptotic fields at the tip of a cohesive crack. Int J Fract 2008;150:55–74. https://doi.org/10.1007/s10704-008-9218-2.

[104] Carlberger T, Stigh U. Influence of Layer Thickness on Cohesive Properties of an Epoxy-Based Adhesive—An Experimental Study. J Adhes 2010;86:816–35. https://doi.org/10.1080/00218464.2010.498718.

[105] Zhu Y, Liechti KM, Ravi-Chandar K. Direct extraction of rate-dependent traction–separation laws for polyurea/steel interfaces. Int J Solids Struct 2009;46:31–51. https://doi.org/10.1016/j.ijsolstr.2008.08.019.

[106] Pinto AMG, Magalhães AG, Campilho RDSG, de Moura MFSF, Baptista APM. Single-Lap Joints of Similar and Dissimilar Adherends Bonded with an Acrylic Adhesive. J Adhes 2009;85:351–76. https://doi.org/10.1080/00218460902880313.

[107] Jang J, Sung M, Han S, Yu W-R. Prediction of delamination of steel-polymer composites using cohesive zone model and peeling tests. Compos Struct 2017;160:118–27. https://doi.org/10.1016/j.compstruct.2016.10.025.

[108] Campilho RDSG, de Moura MFSF, Domingues JJMS. Using a cohesive damage model to predict the tensile behaviour of CFRP single-strap repairs. Int J Solids Struct 2008;45:1497–512. https://doi.org/10.1016/j.ijsolstr.2007.10.003.

[109] Carlberger T, Stigh U. An explicit FE-model of impact fracture in an adhesive joint. Eng Fract Mech 2007;74:2247–62. https://doi.org/10.1016/j.engfracmech.2006.10.016.

[110] Ibrahim AH, Watson B, Jahed H, Rezaee S, Royer C, Cronin DS. Prediction of bonded asymmetric metallic cross-tension and single lap shear joints using finite element model with material-level adhesive properties and cohesive zone method. Int J Adhes Adhes 2023;120:103298. https://doi.org/10.1016/j.ijadhadh.2022.103298.

[111] Sørensen BF. Cohesive law and notch sensitivity of adhesive joints. Acta Mater 2002;50:1053–61. https://doi.org/10.1016/S1359-6454(01)00404-9.

[112] Andersson T, Stigh U. The stress–elongation relation for an adhesive layer loaded in peel using equilibrium of energetic forces. Int J Solids Struct 2004;41:413–34. https://doi.org/10.1016/j.ijsolstr.2003.09.039.

[113] Högberg JL, Stigh U. Specimen proposals for mixed mode testing of adhesive layer. Eng Fract Mech 2006;73:2541–56. https://doi.org/10.1016/j.engfracmech.2006.04.017.

[114] Ji G, Ouyang Z, Li G, Ibekwe S, Pang S-S. Effects of adhesive thickness on global and local Mode-I interfacial fracture of bonded joints. Int J Solids Struct 2010;47:2445–58. https://doi.org/10.1016/j.ijsolstr.2010.05.006.

[115] Campilho RDSG, de Moura MFSF, Domingues JJMS. Numerical prediction on the tensile residual strength of repaired CFRP under different geometric changes. Int J Adhes Adhes 2009;29:195–205. https://doi.org/10.1016/j.ijadhadh.2008.03.005.

[116] Campilho RDSG, de Moura MFSF, Ramantani DA, Morais JJL, Domingues JJMS. Tensile behaviour of three-dimensional carbon-epoxy adhesively bonded single- and double-strap repairs. Int J Adhes Adhes 2009;29:678–86. https://doi.org/10.1016/j.ijadhadh.2009.02.004.

[117] Jung Lee M, Min Cho T, Seock Kim W, Chai Lee B, Ju Lee J. Determination of cohesive parameters for a mixed-mode cohesive zone model. Int J Adhes Adhes 2010;30:322–8. https://doi.org/10.1016/j.ijadhadh.2009.10.005.

[118] Jin ZH, Sun CT. Cohesive Fracture Model Based on Necking. Int J Fract 2005;134:91–108. https://doi.org/10.1007/s10704-005-7864-1.

[119] Liebowitz H, Sih GC. Mathematical theories of brittle fracture. 1968.

[120] Xiao Q, Karihaloo BL. Asymptotic fields at frictionless and frictional cohesive crack tips in quasibrittle materials. J Mech Mater Struct 2006;1:881–910. https://doi.org/10.2140/jomms.2006.1.881.

[121] Rice JR, Sih GC. Plane Problems of Cracks in Dissimilar Media. J Appl Mech 1965;32:418–23. https://doi.org/10.1115/1.3625816.

[122] Cavezza F, Boehm M, Terryn H, Hauffman T. A Review on Adhesively Bonded Aluminium Joints in the Automotive Industry. Metals (Basel) 2020;10:730. https://doi.org/10.3390/met10060730.

[123] Linke M, Lammering R. On the calibration of the cohesive strength for cohesive zone models in finite element analyses. Theor Appl Fract Mech 2023;124:103733. https://doi.org/10.1016/j.tafmec.2022.103733.

[124] Objois A, Assih J, Troalen JP. Theoretical Method to Predict the First Microcracks in a Scarf Joint. J Adhes 2005;81:893–909. https://doi.org/10.1080/00218460500222819.

[125] Alam M, Parmigiani JP, Kruzic JJ. An experimental assessment of methods to predict crack deflection at an interface. Eng Fract Mech 2017;181:116–29. https://doi.org/10.1016/j.engfracmech.2017.05.013.

[126] Materials P, Materials EI, Matrix P, Materials C, Specimens P. Standard Test Method for Tensile Properties of Plastics 1 2006:1–15. https://doi.org/10.1520/D0638-14.1.

[127] Miyagawa H, Mohanty AK, Drzal LT, Misra M. Nanocomposites from biobased epoxy and single-wall carbon nanotubes: synthesis, and mechanical and thermophysical properties evaluation. Nanotechnology 2005;16:118–24. https://doi.org/10.1088/0957-4484/16/1/024.

[128] Yu N, Zhang ZH, He SY. Fracture toughness and fatigue life of MWCNT/epoxy composites. Mater Sci Eng A 2008;494:380–4. https://doi.org/10.1016/j.msea.2008.04.051.

[129] Alloys A, Treatment CA. Standard Guide for Preparation of Metal Surfaces for Adhesive Bonding 1. Society 2000;90:1–6. https://doi.org/10.1520/D2651-01R16.2.

[130] SANDER M, RICHARD H. Experimental and numerical investigations on the influence of the loading direction on the fatigue crack growth. Int J Fatigue 2006;28:583–91. https://doi.org/10.1016/j.ijfatigue.2005.05.012.

[131] Machado JJM, Marques EAS, Campilho RDSG, da Silva LFM. Mode II fracture toughness of CFRP as a function of temperature and strain rate. Compos Part B Eng 2017;114:311–8. https://doi.org/10.1016/j.compositesb.2017.02.013.

[132] Gojny F, Wichmann M, Fiedler B, Schulte K. Influence of different carbon nanotubes on the mechanical properties of epoxy matrix composites – A comparative study. Compos Sci Technol 2005;65:2300–13. https://doi.org/10.1016/j.compscitech.2005.04.021.

[133] Alian AR, El-Borgi S, Meguid SA. Multiscale modelling of the effect of waviness and agglomeration of CNTs on the elastic properties of nanocomposites. Comput Mater Sci 2016;117:195–204. https://doi.org/10.1016/j.commatsci.2016.01.029.

[134] Cui H. Numerical simulation of crack propagation in solid propellant with extrinsic

cohesive zone model. Meccanica 2022;57:1617–30. https://doi.org/10.1007/s11012-022-01516-6.

[135] Zhang Z, Paulino GH, Celes W. Extrinsic cohesive modelling of dynamic fracture and microbranching instability in brittle materials. Int J Numer Methods Eng 2007;72:893–923. https://doi.org/0.1002/nme.2030.

[136] Katsivalis I, Thomsen OT, Feih S, Achintha M. Development of cohesive zone models for the prediction of damage and failure of glass/steel adhesive joints. Int J Adhes Adhes 2020;97:102479. https://doi.org/10.1016/j.ijadhadh.2019.102479.

[137] Precision WS. Standard Test Method for Short-Beam Strength of Polymer Matrix Composite Materials. Annu B ASTM Stand 2011;00:1–8. https://doi.org/10.1520/D2344.

[138] ASTM D5528-01. Standard test method for mode I interlaminar fracture toughness of unidirectional fiber-reinforced polymer matrix composites. Am Stand Test Methods 2014;03:1–12. https://doi.org/10.1520/D5528-13.2.

[139] ASTM D7905. Standard test method for determination of the mode II interlaminar fracture toughness of unidirectional fiber-reinforced polymer matrix composites. Astm 2014:1–18. https://doi.org/10.1520/D7905.

[140] D6671M A. Standard Test Method for Mixed Mode I-Mode II Interlaminar Fracture Toughness of Unidirectional Fiber Reinforced Polymer Matrix Composites. ASTM Int 2006;i:15. https://doi.org/10.1520/D6671.

[141] Rodríguez-González JA, Avilés F. A modified short beam shear specimen for characterization of interfacial strength in nanocomposites. Polym Test 2012;31:792–9. https://doi.org/10.1016/j.polymertesting.2012.04.011.

[142] Fan Z, Santare MH, Advani SG. Interlaminar shear strength of glass fiber reinforced epoxy composites enhanced with multi-walled carbon nanotubes. Compos Part A Appl Sci Manuf 2008;39:540–54. https://doi.org/10.1016/j.compositesa.2007.11.013.

[143] Rahman MM, Zainuddin S, Hosur MV, Robertson CJ, Kumar A, Trovillion J, et al. Effect of NH2-MWCNTs on crosslink density of epoxy matrix and ILSS properties of e-glass/epoxy composites. Compos Struct 2013;95:213–21. https://doi.org/10.1016/j.compstruct.2012.07.019.

[144] Borowski E, Soliman E, Kandil U, Taha M. Interlaminar Fracture Toughness of CFRP Laminates Incorporating Multi-Walled Carbon Nanotubes. Polymers (Basel) 2015;7:1020–45. https://doi.org/10.3390/polym7061020.

[145] Greenhalgh E, Singh S. The Effect of Moisture, Matrix and Ply Orientation on Delamination Resistance, Failure Criteria and Fracture Morphology in CFRP. Compos. Mater. Testing, Des. Accept. Criteria, 100 Barr Harbor Drive, PO Box C700, West Conshohocken, PA 19428-2959: ASTM International; 2002, p. 221-221–14. https://doi.org/10.1520/STP10642S.

[146] Omairey SL, Dunning PD, Sriramula S. Development of an ABAQUS plugin tool for periodic RVE homogenisation. Eng Comput 2019;35:567–77. https://doi.org/10.1007/s00366-018-0616-4.

[147] Tam DKY, Ruan S, Gao P, Yu T. High-performance ballistic protection using polymer nanocomposites. Adv. Mil. Text. Pers. Equip., Elsevier; 2012, p. 213–37. https://doi.org/10.1533/9780857095572.2.213.

[148] Vasiliev V V, Morozov E V. Mechanics and analysis of composite materials. Elsevier; 2001.

[149] Cheng G-D, Cai Y-W, Xu L. Novel implementation of homogenization method to predict effective properties of periodic materials. Acta Mech Sin 2013;29:550–6. https://doi.org/10.1007/s10409-013-0043-0.

[150] Tjong SC. Carbon Nanotube Reinforced Composites. vol. 3. Wiley; 2009. https://doi.org/10.1002/9783527626991.

[151] Rakesh P, More A, Kumar M, Muthu N. Probabilistic failure prediction in a double composite cantilever beam with single and double source uncertainty. Compos Struct 2022;279:114870. https://doi.org/10.1016/j.compstruct.2021.114870.

[152] de Morais AB, Pereira AB, de Moura MFSF, Silva FGA, Dourado N. Bilinear approximations to the mixed-mode I–II delamination cohesive law using an inverse method. Compos Struct 2015;122:361–6. https://doi.org/10.1016/j.compstruct.2014.11.058.

[153] Harper PW, Sun L, Hallett SR. A study on the influence of cohesive zone interface element strength parameters on mixed mode behaviour. Compos Part A Appl Sci Manuf 2012;43:722–34. https://doi.org/10.1016/j.compositesa.2011.12.016.

[154] Gong Y, Zhao L, Zhang J, Hu N. An improved power law criterion for the delamination propagation with the effect of large-scale fiber bridging in composite multidirectional laminates. Compos Struct 2018;184:961–8. https://doi.org/10.1016/j.compstruct.2017.10.076.